Molecular Mechanisms of MYC as Stress Resilience Factor

Molekulare Mechanismen von MYC als Stressresistenzfaktor

Doctoral thesis for a doctoral degree
at the Graduate School of Life Sciences,
Julius-Maximilians-Universität Würzburg,
Section Biomedicine

submitted by

Daniel Alexander Solvie

from

Karlsruhe

Würzburg 2022

Submitted on: 28.10.2022

Members of the Thesis Committee

Chairperson: Prof. Dr. Alexander Buchberger

Primary Supervisor: Prof. Dr. Martin Eilers
Second Supervisor: Prof. Dr. Petra Beli
Third Supervisor: Prof. Dr. Nikita Popov

Date of Public Defense: 10.03.2023

Date of Receipt of Certificates:

Table of contents

1 Summary

Cancer is one of the leading causes of death worldwide. The underlying tumorigenesis is driven by the accumulation of alterations in the genome, eventually disabling tumor suppressors and activating proto-oncogenes.

The MYC family of proto-oncogenes shows a strong deregulation in the majority of tumor entities. However, the exact mechanisms that contribute to MYC-driven oncogenesis remain largely unknown. Over the past decades, the influence of the MYC protein on transcription became increasingly apparent and was thoroughly investigated. Additionally, in recent years several publications provided evidence for so far unreported functions of MYC that are independent of a mere regulation of target genes. These findings suggest an additional role of MYC in the maintenance of genomic stability and this role is strengthened by key findings presented in this thesis.

In the first part, I present data revealing a pathway that allows MYC to couple transcription elongation and DNA double-strand break repair, preventing genomic instability of MYC-driven tumor cells. This pathway is driven by a rapid transfer of the PAF1 complex from MYC onto RNAPII, a process that is mediated by HUWE1. The transfer controls MYC-dependent transcription elongation and, simultaneously, the remodeling of chromatin structure by ubiquitylation of histone H2B. These regions of open chromatin favor not only elongation but also DNA double-strand break repair.

In the second part, I analyze the ability of MYC proteins to form multimeric structures in response to perturbation of transcription and replication. The process of multimerization is also referred to as phase transition. The observed multimeric structures are located proximal to stalled replication forks and recruit factors of the DNA-damage response and transcription termination machinery. Further, I identified the HUWE1-dependent ubiquitylation of MYC as an essential step in this phase transition. Cells lacking the ability to form multimers display genomic instability and ultimately undergo apoptosis in response to replication stress.

Both mechanisms present MYC as a stress resilience factor under conditions that are characterized by a high level of transcriptional and replicational stress. This increased resilience ensures oncogenic proliferation.

Therefore, targeting MYC’s ability to limit genomic instability by uncoupling transcription elongation and DNA repair or disrupting its ability to multimerize presents a therapeutic window in MYC-dependent tumors.

2 Zusammenfassung

Tumorerkrankungen sind eine der häufigsten Todesursachen weltweit. Für die Entstehung und Entwicklung eines Tumors sind Veränderungen im Genom verantwortlich, wobei Proto-Onkogene aktiviert und Tumorsuppressorgene inaktiviert werden.
Die MYC-Familie der Proto-Onkogene ist in der Mehrzahl der menschlichen Tumorerkrankungen stark dereguliert. Der genaue Mechanismus, der in MYC-getriebenen Tumoren eine Rolle spielt, ist aber weiterhin ungeklärt. In den letzten Jahrzehnten wurde die Funktion von MYC als Transkriptionsfaktor in den Vordergrund gestellt. Veröffentlichungen der letzten Jahre deuten zusätzlich auf mehrere, bisher unbekannte Funktionen hin, die unabhängig von einer bloßen Regulation von Zielgenen sind und auf eine zusätzliche Rolle bei der Erhaltung der genomischen Stabilität hinweisen. Diese Rolle wird durch wesentliche Ergebnisse dieser Doktorarbeit gestärkt.

In dem ersten Teil der Doktorarbeit präsentiere ich einen Pathway, der es MYC ermöglicht, transkriptionelle Elongation und Doppelstrangbruch-Reparatur zu koppeln, wodurch genomische Instabilität in MYC-gesteuerten Tumorzellen limitiert wird. Dieser Pathway wird durch einen schnellen Transfer des PAF1-Komplexes von MYC auf die RNAPII angetrieben, bei dem HUWE1 eine essenzielle Rolle einnimmt. Der Transfer steuert die MYC-abhängige transkriptionelle Elongation und gleichzeitig die Öffnung der Chromatinstruktur. Dies geschieht durch Ubiquitylierung des Histons H2B zugunsten von sowohl transkriptioneller Elongation als auch der DNA-Doppelstrangbruchreparatur.

In dem zweiten Teil der Doktorarbeit analysiere ich die Fähigkeit von MYC-Proteinen, als Reaktion auf eine Störung der Transkription und/oder Replikation multimere Strukturen bilden zu können. Diese Fähigkeit wird auch als Phasentrennung bezeichnet. Die multimere Strukturen befinden sich in der Nähe von blockierten Replikationsgabeln und rekrutieren Faktoren der DNA-Schadensreaktion und der Transkriptionsterminationsmaschinerie. Die HUWE1-abhängige Ubiquitylierung von MYC habe ich als wesentlichen Schritt der Phasentrennung identifiziert. Zellen ohne die Fähigkeit zur Bildung von Multimeren zeigen als Reaktion auf Replikationsstress exzessive genomische Instabilität und letztendlich Apoptose auf.

Beide Mechanismen machen MYC zu einem Faktor, der genomische Instabilität als Resultat von unphysiologischem Transkriptions- und Replikationsstress limitiert und damit die onkogene Zellteilung gewährleistet. Eine gezielte Beeinflussung der aufgeführten Mechanismen, durch welche MYC die genomische Instabilität limitiert, kann bei MYC-abhängigen Tumoren von großem therapeutischem Nutzen sein.

3 Introduction

3.1 Oncogenesis

Cancer is one of the leading causes of death worldwide with more than 19 million cases diagnosed in 2020 (Ferlay et al., 2021). Tumors are thought to originate from single cells by a gradual accumulation of multiple mutations or alterations of genes and their products that regulate cell differentiation, proliferation, and cell death (Hanahan and Weinberg, 2000; 2011). The genes that are positively regulating these key regulatory steps in cellular biology are termed proto-oncogenes. Direct mechanisms that convert proto-oncogenes into active oncogenes are either structural changes of the respective protein itself (e.g. the constitutive activation of KRAS), or alterations in gene expression. These expression changes are often the result of an amplification of the gene locus or a genetic translocation that places the proto-oncogene under the control of a highly active promoter/enhancer sequences (Kontomanolis et al., 2020). Oncogenes are opposed in their function by tumor suppressors that are defined as proteins restraining proliferation and inducing apoptosis in response to biological abnormalities. Hence, the inactivation of tumor suppressors and the respective repercussions are a common hallmark of cancer. Many tumor suppressors surveil the integrity of the genome. Consequently, the activation of oncogenes, as discussed above, and the inactivation of tumor suppressors are of utmost importance for the mutagenesis during tumor development. The inactivation of a tumor suppressor such as TP53, the “guardian of the genome”, accelerates the accumulation of mutations, ranging from a few functionally indispensable “driver” mutations to several hundred expendable “passenger” mutations. Principles that are analog to classical evolution shape the cancer genome in the above discussed manner through a process of clonal expansion over a timespan of several years up to decades (Greaves and Maley, 2012; Hanahan and Weinberg, 2011).

To date, more than 50 oncogenes have been identified (Kontomanolis et al., 2020). While the transforming principles of many oncogenes are apparent, the exact functional mechanisms of the family of MYC oncogenes are controversial and subject of this thesis.

3.2 The family of MYC oncogenes

With its discovery in the early 1970s, v-*myc* was one of the first oncogenes described and it was later shown to originate from the chicken c-*myc* gene (Vennstrom et al., 1982). c-*myc* and the corresponding human paralog *MYC* belong to the family of MYC oncogenes comprising *MYC*, *MYCN* and *MYCL*. Several signaling pathways that sense environmental stimuli, such as the MAK/ERK-pathway, converge on MYC. Consequently, it was suggested that its physiological role is the cellular reprogramming on the transcriptional level and includes maintenance of pluripotency as well as stem cell maturation in a tissue specific manner (Eilers and Eisenman, 2008; Gandarillas and Watt, 1997; Takahashi and Yamanaka, 2006).

The MYC family belongs to the oncogenes with the highest amplification rate among many human cancers (Dang, 2012). In addition to amplification of the gene locus, several mechanisms have been observed that enable either an increased MYC protein expression, including gene translocation, placing MYC at the highly transcribed immunoglobulin locus in multiple myeloma (Shou et al., 2000) or an enhanced transcription of the *MYC* gene by inactivation of the tumor suppressor APC (He et al., 1998). Additionally, the protein half-life can be increased by activation of the RAS/RAF/ERK pathway (Sears et al., 2000). All of these mechanisms are downstream of oncogenic events and in line with the observation that MYC amplification alone is not sufficient as a transformation stimulus and requires additional events such as the activation of KRAS (Dang, 2012).

3.3 The structure of MYC proteins

The ability of MYC to control cell growth and proliferation is based on its ability to bind DNA as a heterodimer together with its partner protein MAX. This binding is mediated by the basic helix-loop-helix leucin zipper (bHLH-LZ) motif that is located in the conserved C-terminal domain of MYC. The bHLH-LZ motif increases the affinity of the heterodimer towards DNA sequences enriched for E-boxes with the consensus CAC(G/A)TG sequence (Blackwood and Eisenman, 1991). However, many binding sites lack this specific sequence and several publications suggest that interaction partners are required to enhance MYC's chromatin affinity, as for instance shown for the interaction of MYC with WDR5 (Guo et al., 2014; Thomas et al., 2015).

Apart from the C-terminal domain, six more highly conserved regions, termed MYC-boxes (MBs), are present among the MYC family members. Each of these six MBs mediates the binding to a specific subset of MYC interactors. Deletions and point mutations were used to characterize the MBs, and the results of these experiments are depicted for exemplary interactors in Figure 3.3.1.

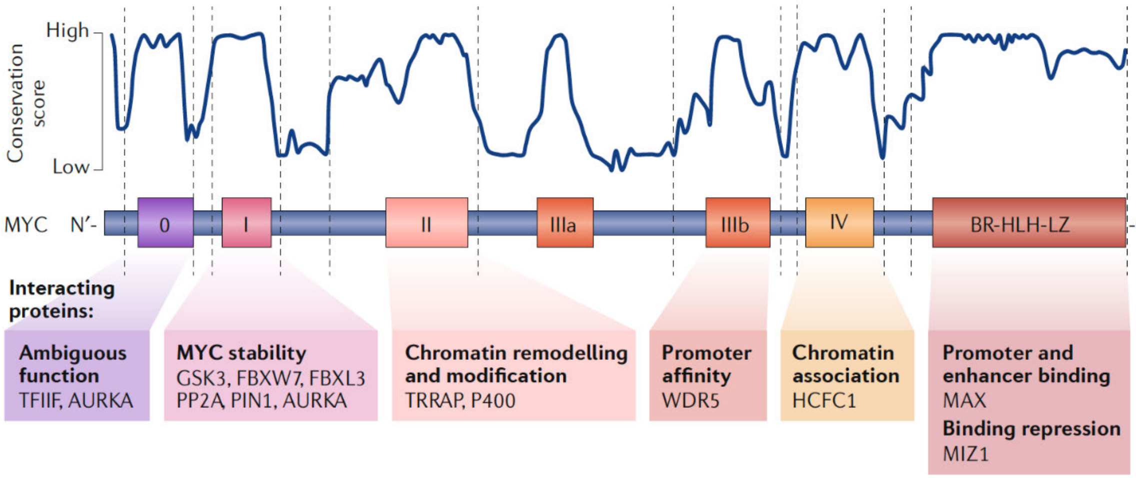

Figure 3.3.1: Conserved regions of MYC proteins.

Conservation score for the full-length structure of MYC depicting regions with high sequence identity among the three MYC family members. Exemplary interactors of the respective MBs and subsequent function are indicated below. This figure was published in a similar form in Baluapuri et al. (2020).

Structurally, MYC resembles classical transcription factors that contain the transcriptional associated domain (TAD) and a structured DNA binding domain (DBD). The N-terminal unstructured domain of MYC, including MBI and II, has been associated with transcriptional activity (Kato et al., 1990; Nie et al., 2020). This is consistent with the finding, that MBI regulates MYC protein ubiquitylation and turnover which has been associated with the activating effect of MYC on transcriptional elongation (Farrell and Sears, 2014; Jaenicke et al., 2016). MBII additionally mediates the interaction with the coactivator and scaffold protein TRRAP that is involved in chromatin remodeling and histone acetylation (McMahon et al., 1998).

MBIIIb and MBIV are located outside of the TAD domain and can associate with WDR5 and HCFC1, proteins that were shown to enhance the chromatin association of MYC (Thomas et al., 2016; Thomas et al., 2015).

Heterodimerization with MAX via the bHLH-LZ domain mediates the DNA interaction of MYC as discussed above. However, at oncogenic MYC levels the zinc finger protein MIZ1 competes with MAX for binding resulting in a repression of genes that are transcriptionally regulated by MYC (Walz et al., 2014).

Available crystal structures of MYC encompass only the more structured C-terminal part of MYC which is only about 20% of the full-length protein (Figure 3.3.2a). Despite of recent progress in the field of artificial intelligence, predictions of MYC's complete 3D structure are still rather vague (Figure 3.3.2b).

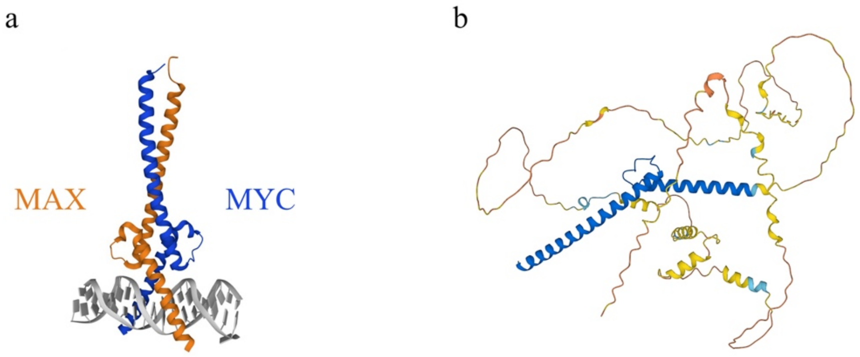

Figure 3.3.2: Available and predicted structure of the MYC protein.
(a) Recombinant MYC-MAX heterodimer recognizing DNA. MYC comprises the AA 353-439, MAX AA 23-102 (Nair and Burley, 2003). (b) Predicted full-length structure of MYC (P01106); color code represents model confidence (blue: very high; light blue: confident; yellow: low; orange: very low) (Jumper et al., 2021).

While the structured bHLH-LZ domain of MYC can be predicted with high confidence using AlphaFold (Jumper et al., 2021) and resembles the published structure very closely, the residual domains of MYC lack a confident prediction and barely display secondary or tertiary structures. Inspection of the amino acid composition of the N-terminus reveals a composition that is dominated by low-complexity stretches that exhibit a preference for conformational heterogeneity and are also referred to as intrinsically disordered regions (IDRs).

IDRs can be estimated using machine learning in form of neuronal networks based on amino acid composition, hydropathy, or sequence complexity in a sliding window approach. Theses algorithms are trained on ordered and disordered amino acid sequences with available experimental data. Corresponding predictions for MYC (Figure 3.3.3) with the VSL-2 algorithm (Peng et al., 2006) result in two major IDRs, one encompassing 50 AA around MBI and a second one from MBII to the bHLH-LZ domain consisting of 242 AA. The flDPnn algorithm (Hu et al., 2021) predicted several smaller IDRs over the complete protein sequence, sparing only MBII, IIIa, IV and the bHLH-LZ region. Both approaches produce comparable results, although the threshold of flDPnn to interpret amino acid stretches as contiguous IDRs is slightly more relaxed, with more than 80% of MYC considered as unstructured. Highly unstructured proteins typically share the ability to participate in multivalent and phase separated interactions. Consequently, these characteristics have been proposed for MYC (Baluapuri et al., 2020; Boija et al., 2018) and will be introduced in the chapter 3.6.

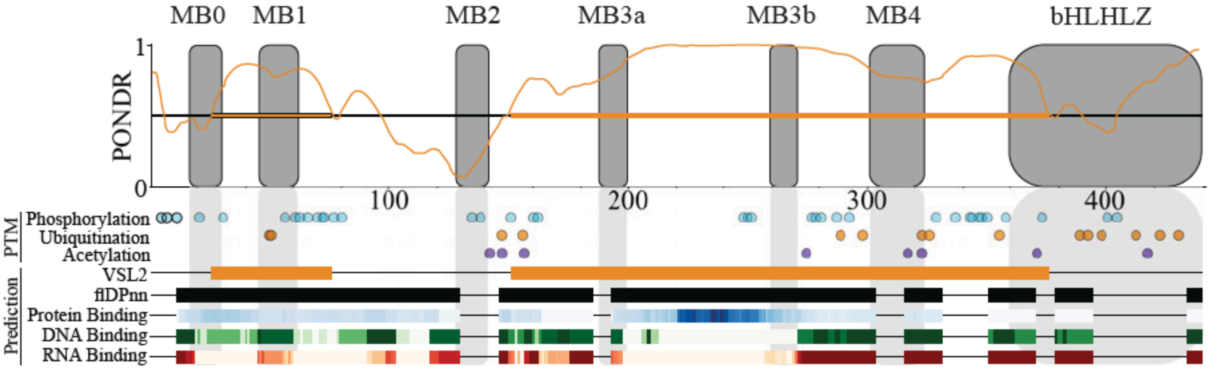

Figure 3.3.3: Intrinsic disorder and disorder function prediction of the MYC protein.

Diagram depicting disorder prediction of the MYC protein (P01106) using the PONDR score (VSL-2) (Peng et al., 2006) and the flDPnn tool (Hu et al., 2021). Prediction is overlayed with MBs and post translational modifications (PTMs) (Hornbeck et al., 2015) as well as prediction of disorder function in form of protein, DNA and RNA binding (Hu et al., 2021).

Due to the unstructured nature of the protein, approaches to target MYC in tumor therapy with small molecule inhibitors remain unsuccessful. In combination with the nuclear localization that excludes immunological approaches that rely on surface presentation, MYC has been considered “undruggable” (Llombart and Mansour, 2022).

3.4 Oncogenic models of MYC

Over the last decades several models were proposed to explain the transforming principle of MYC. All models agree on several characteristics of MYC that have been presented in the previous chapters. These characteristics are the heterodimerization of MYC with its partner protein MAX via the bHLH-LZ region, the presence of the heterodimer at all active promoter regions which is mediated by binding to E-Boxes and, with lower affinity, other DNA sequences. Furthermore, several structurally conserved MBs in the MYC protein, which mediate specific protein-protein contacts and thereby contribute to a diverse interactome of MYC, are part of the consensus.

The respective models are introduced in the following paragraphs.

3.4.1 The gene regulatory model

The transforming principle of MYC which relates changes in MYC protein abundance to subsequent changes on gene expression is discussed by three models in the literature.

The gene-selective activator model states that MYC drives the expression of a small number of genes which in turn regulate cellular processes (Sabo et al., 2014; Tesi et al., 2019; Walz et al., 2014). Considering that MYC is bound to all active promoters, this model implies that MYC binding has very little effect on the expression of the majority of genes.

The global-amplifier model, in contrast, states that the functionality of all active promoters is enhanced by MYC binding thereby increasing global mRNA levels (Lin et al., 2012; Nie et al., 2020; Nie et al., 2012). However, the actual change of gene expression in response to extensive manipulation of MYC protein abundance remains marginal (Baluapuri et al., 2020).

The gene-specific affinity model addressed the discrepancy between the comparably low affinity of the MYC-MAX heterodimer to E-boxes and the finding that the heterodimer is present at all active promoters. This model predicts that MYC binding and the respective effects on gene expression are dictated by the interactors of MYC that determine the promoter binding affinity (Lorenzin et al., 2016).

All models and the underlying studies depend profoundly on the choice of statistical parameters and computational algorithms and have led to a discussion about technical concerns. Regardless of which gene regulatory model ultimately prevails, the mild effects of global promoter binding on mRNA levels reason for additional, gene expression independent functions of MYC. These are subject of the following models.

3.4.2 The interactome as driver of MYC functions

Multiple interactomes of the MYC and MYCN proteins have been previously published (Baluapuri et al., 2019; Buchel et al., 2017; Heidelberger et al., 2018; Kalkat et al., 2018) and thorough investigation concluded on a shared interactome consisting of 80 proteins (Baluapuri et al., 2020).

The number and heterogenous composition of the interactome suggests MYC's participation in various complexes of diverse function. These include chromatin remodelling, including histone modification as exemplarily represented by members of the SWI/SNF, NuRD and NuA4 complex, and chromatin topology, for instance represented by the TFIIIC complex. Simultaneously, MYC interacts with parts of the ubiquitin-proteasome system e.g., PSMC3 and further subunits of the proteasome, as well as with several transcription regulators and polymerase associated factors, like WDR5 and the PAF1 complex (PAF1c). Further functional groups of interactors include splicing, the cell cycle, DNA damage and nucleolar factors (Baluapuri et al., 2020; Kalkat et al., 2018).

In line with the discrepancy between promoter binding and the subsequent effects on gene expression, the diverse functional groups of MYC interactors suggest a role of MYC that reaches beyond a mere effect on changes in mRNA levels.

3.4.3 The hand-over model

The hand-over model considers MYC as a recruitment platform for members of the diverse MYC interactome to the promotor region, which is followed by a transfer from MYC onto RNAPII (Baluapuri et al., 2020). This notion is supported by recent publications on the interplay of MYC and the elongation factors SPT5 and PAF1c (Baluapuri et al., 2019; Jaenicke et al., 2016).

It was shown that depletion of MYC reduced chromatin and RNAPII association of SPT5 and resulted in transcriptional defects that correlate with the effects exhibited by SPT5 depletion. Intriguingly, the results suggest a hook-like effect, where excessive abundance of the MYC protein can sequester interactors away from the transcription machinery into complexes that are not associated with the chromatin (Baluapuri et al., 2019).

PAF1c hand-over from MYC onto RNAPII is controlled by the ubiquitin system, and interference with the ubiquitin system impairs this hand-over step, resulting in the accumulation of repressive intermediates instead. These observations propose a regulatory function of the ubiquitylation of MYC in the hand-over model (Jaenicke et al., 2016).

The hand-over model combines the large interactome of MYC and the effects of MYC on transcription. To date, the examples include only transcriptional regulators, but the model is likely to extend to more functional groups of the MYC interactome.

3.4.4 Transcriptional stress resilience

In addition to roles in regulating and promoting transcription, several interactors of MYC have roles implicated in the response to transcription stress.

The topoisome for instance, which is assembled and stimulated by MYC, consists of Topoisomerase 1 and 2 and relieves DNA from excessive supercoiling and therewith from torsional stress that is caused by high transcriptional output. Consequently, MYC's functional relation to the topoisome prevents genomic instability (Das et al., 2022).

Transcription induced negative supercoiling promotes the formation of DNA-RNA hybrids, referred to as R-loops, which have been shown to disrupt transcription and cause double strand breaks (DSBs) (Aguilera and Garcia-Muse, 2012). PAF1c can clear co-transcriptional R-loops, most likely due to its role in H2B ubiquitylation together with the E3-ligase RNF20-RNF40 (Shivji et al., 2018; Van Oss et al., 2016). Similarly, MYCN has been shown to prevent promoter-proximal R-loops by recruitment of BRCA1 (Herold et al., 2019) and by chromatin remodeling that is induced by the formation of a complex with AURKA (Roeschert et al., 2021). Furthermore, the NuA4 complex is implicated in DSB repair in promoter regions by destabilizing histones and a subsequent remodelling of the chromatin in cooperation with the ATPase activity of p400, another MYC interactor (Jacquet et al., 2016; Xu et al., 2010b).

Taking into account that several MYC interactors have a role in the prevention or the resolution of transcription stress, the stress-resilience model offers an explanation for the discrepancy between MYC binding and effects on gene expression by maintaining genetic integrity of promoter and genic regions under conditions with high transcriptional activity (Baluapuri et al., 2020).

3.4.5 Coordination of transcription-replication conflicts

Tumors show high levels of replication stress, induced by several conditions that will be introduced in detail in chapter 3.5. This includes in particular conflicts between the transcription and the replication fork. Reasons for these conflicts are for example the stalling of the RNA polymerase and the formation of R-loops. These problems are enhanced by non-physiological transcription rates in the S-phase as well as by premature origin-firing during oncogenesis (Garcia-Muse and Aguilera, 2016; Macheret and Halazonetis, 2018).

Several findings suggest a role of MYC proteins in preventing these S-phase specific conflicts. MIZ1 limits the expression of canonical MYC target genes in the S-phase. Furthermore, the S- and G2-phase specific binding of AURKA to MYCN, outcompetes MYCN co-activators and hence represses effects on transcriptional elongation (Baluapuri et al., 2020).

As discussed in the previous chapter, MYC proteins reduce the abundance of a major risk-factor for transcription-replication conflicts, namely R-loops, and prevent DNA lesions that can also result in RNA polymerase stalling. Moreover, a recent publication demonstrates the ability of MYCN to recruit the RNA exosome to promoters and thereby facilitate termination of stalled RNA polymerases in favor of the replisome (Papadopoulos et al., 2021).

The model of transcription-replication coordination can be interpreted as an extension of the previously introduced stress-resilience model because the relieve of introduced stresses directly translates into the reduction of transcription-replication conflicts.

In summary, the gene-regulatory independent models emerged from the observation that the diverse interactome of MYC contains complexes with functions that extend far beyond the regulation of gene expression. These models for additional functions of MYC are particularly supported by the functional interaction of MYC with proteins that are involved in limiting transcription and replication stress.

At the same time, a mechanism that spatially and temporally controls the interactions between MYC and functionally distinct groups of partner proteins remains unclear.

3.5 Chromatin maintenance

As already indicate in chapter 3.1, the inability to effectively surveille genomic integrity is a hallmark of cancer and mutations or other defects in the DDR system even increase the genomic instability. This chapter will introduce the basic mechanisms in DDR, particularly in the context of transcription and replication stress.

Cells are continuously exposed to sources of DNA damage, originating either from within the cell or from environmental influences.

Endogenous causes for DNA damage include rare events like replication errors in form of insertions and deletions with 10^{-6} to 10^{-8} events per cell per division, as well as the chemical instability of the DNA itself. More common causes are torsional stress introduced by transcription and replication and reactive oxygen species (ROS) (Chatterjee and Walker, 2017). Exogenous sources include ionizing radiation (IR), ultraviolet radiation (UV), as well as chemicals inducing crosslinking and alkylation (Chatterjee and Walker, 2017).

The types of damage that result from these endogenous and exogenous sources range from a single base that is affected to lesions including aberrant DNA structures, as well as single strand breaks (SSBs) and double strand breaks (DSBs) of DNA.

A healthy cell has several pathways to alleviate these damages.

While mismatch repair (MMR) recognizes replication errors through the bulge in the DNA helix that is caused by mismatched base-pairs, base excision repair (BER) corrects lesions that are caused by events that do not alter the DNA helix like for instance base oxidation or hydrolysis. Furthermore, it is responsible for the repair of SSBs with the help of PARP1 (Chatterjee and Walker, 2017).

Nucleotide excision repair (NER) is specialized in removal of bulky lesions as induced by the formation of pyrimidine dimers through UV. NER requires TFIIH, a complex involved in transcription initiation but also in DDR through its ability to open DNA at promoter regions or at sites of lesions, respectively (Kokic et al., 2019). Bulky lesions present roadblocks for transcription and induce stalling of the RNAPII. To allow repair factors and TFIIH to access the lesion, RNAPII backtracks and can be either degraded by the ubiquitin system or resume transcription with the help of TFIIS (Noe Gonzalez et al., 2021).

The most toxic DNA lesions are DSBs where there is a risk of the loss of sequences and chromosomal aberrations. Homologous recombination (HR) and non-homologous end joining (NHEJ) are the two major pathways that evolved to repair DSBs.

NHEJ is initiated by binding of Ku70-Ku80 to the free DNA ends and the recruitment of DNA-PKcs. Together these factors bridge the gap between the two ends of a DSB followed by ligation (Scully et al., 2019). In contrast to HR, NHEJ does not require the presence of homologous DNA sequences or a sister chromatid and can therefore take place throughout the cell cycle.

Similar to NHEJ, the cascade of HR starts by Ku70-Ku80 binding to DNA ends. Subsequently, the DSB is resected in 3'-5' direction by the MRN complex resulting in single stranded DNA (ssDNA) that is initially covered by RPA. Subsequently, RPA is replaced by RAD51 which mediates homologous pairing. Several steps of this complex cascade are coordinated by BRCA1 (Scully et al., 2019).

The choice of a pathway is dictated by presence or absence of DNA end resection. The entry into S-phase provides activating signaling for enzymes that mediate DNA end resection and subsequently promote HR. On the other hand, BRCA1 can be antagonized by 53BP1, a mechanism that prevents end resection and therefore promotes NHEJ (Bunting et al., 2010).

Master regulators of the DSB response are three PI3-kinases DNA-PKcs, ATM and ATR. All three kinases are activated by different complexes or DNA structures and subsequently phosphorylate partially overlapping groups of substrates.

As described above, DNA-PKcs is activated by Ku70-Ku80, but can also be targeted by ATM and ATR and is the main kinase mediating phosphorylation of RPA32 at serine 4 and 8 (S4S8RPA). This phosphorylation is a sequential event that follows ATR mediated phosphorylation of RPA32 at serine 33 (S33RPA). Phosphorylation of S4S8RPA is required for full activation of ATR but also signals replication catastrophe (Marechal and Zou, 2015; Menolfi and Zha, 2020).

ATM is activated by the MRN complex and, besides many other substrates, phosphorylates H2AX, which in turn serves as a hub for signaling and recruitment of the DDR machinery and phosphorylation of CHK2 and p53 (Paull, 2015). Additionally, ATM stimulates ubiquitylation of H2B at lysine 120 (K120), a posttranslational modification required for recruitment of the DDR factors and for a rapid repair of DSBs (Moyal et al., 2011).

Activation of ATR requires RPA coated ssDNA that is generated by DSB resection, R-loops formation, and stalled replication forks. Furthermore, the RPA binder ATRIP is required for ATR activation, as well as the 9-1-1 complex, TopBP1 or ETAA. Active ATR phosphorylates CHK1 and thereby suppresses entry into mitosis and origin firing, and it stabilizes replication forks (Saldivar et al., 2017).

As indicated above, transcription and replication are dependent on the DDR machinery in several ways. DNA damage induced replication stress, a paused or slow moving RNAPII and torsional stress can stall the replication fork, exposing segments of ssDNA. These are subsequently bound and protected by RPA and stimulate the loading of the 9-1-1 complex. Together these factors activate ATR signaling. Simultaneously, activated DDR subsequently allows the continuation of replication (Cimprich and Cortez, 2008).

RNA polymerases respond to the same factors that induce stalling of the DNA polymerases with particular emphasis on DSB induced by torsional stress due to high levels of transcription (Singh et al., 2020). During replication the template strand is essential for the cell in order to prevent the loss of genetic information. Similarly important is the stabilization of the nascent replication product and the resumption of a stalled replication fork to ensure genomic integrity. In contrast, nascent RNA is non-essential for the cell and therefore the eviction of RNA polymerase from the chromatin is a common pathway to resolve stalled RNA polymerases and also transcription-replication conflicts (Edenberg et al., 2014). As mentioned above, stalling of the RNA polymerase can lead to a transcription-coupled repair (TCR) including the opening of chromatin for DDR factor recruitment and eviction or restart of RNAPII.

In accordance with the large number of factors that are involved in the various signaling cascades that are activated in response to DNA damage, DNA damage sites give rise to clusters of DDR factors. These clusters can display characteristics of phase separation (Banani et al., 2017; Levone et al., 2021), a concept that will be introduced in the next chapter.

3.6 Phase separation

IDRs, which were previously introduced in the context of MYC's structure, display an overrepresentation of amino acids with polar, charged and aromatic side chains, that can mediate multivalent contacts between several IDRs through electrostatic, hydrophobic, π-π and several other types of interaction (Boeynaems et al., 2018) thereby functioning as sticker regions that drive protein assemblies.

From a purely thermodynamic perspective, entropy favors a state of chaos which commonly results in a well-mixed system. In a system that contains only two types of molecules, "A" and "B", this means that interactions between A and B (A-B) are energetically favorable over A-A or B-B interactions (Figure 3.6.1a). However, in biological systems homotypic interactions (A-A or B-B) can sometimes be more favorable than heterotypic interactions. In this case the system will de-mix into two phases (Figure 3.6.1b). A frequently used example to visualize the separation into phases is the addition of hydrophobic oil to water.

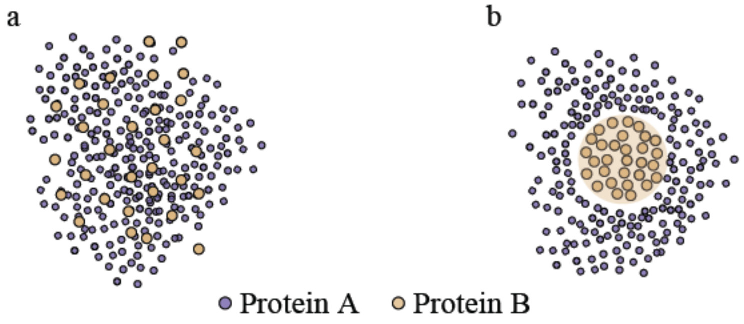

Figure 3.6.1: Phase separation in a two-component system.

(a) The heterotypic interaction of Protein A and B is favorable over homotypic interactions. (b) homotypic interactions of Protein B are favorable over heterotypic interactions.

Apart from this simplified example, phase separation is commonly observed in a cellular context when multivalent interactions energetically favor homotypic interactions of molecules. A prime example are P granules in *Caenorhabditis elegans* that form due to phase separation of the LAF-1 protein (Elbaum-Garfinkle et al., 2015).

In addition to homotypic interactions, phase separation in a biological system can be driven by multivalent interactions of IDRs from different proteins or even by interactions with RNA. Many phase separated proteins contain either RNA binding motives or are predicted to interact with RNA (Gomes and Shorter, 2019; Sharp et al., 2022). For instance, nucleoli contain hundreds of enriched proteins, several of whom bind to newly synthesized rRNA. In i*n vitro* experiments only a small fraction of these proteins are essential for phase transition, suggesting that the recruitment of the remaining proteins via multivalent interactions occurs at a later stage (Shin and Brangwynne, 2017). Regardless of the vast number of different proteins that are involved in this particular example, phase separation is a highly selective process that results in a distinct molecular composition, representing a form of compartmentalization.

Compartmentalization is a cellular principle that aims at optimizing biochemical conditions. It allows to control cellular materials and metabolic processes and contains signaling pathways, thereby, increasing complexity. Commonly, compartmentalization is achieved through organelles that are surrounded by membranes, for instance mitochondria. Phase separation allows the formation of additional membrane-less organelles, thereby extending cellular complexity even further. This is reflected by the variety of biomolecular condensates that can be found in cells, including P bodies, stress granules, cajal bodies or para speckles, to name only a few, and by their diverse biological functions of these structures (Gu et al., 2022).

Biomolecular condensates are characterized by rapid dynamics including formation and dissolution within seconds and selective exchange with the environment. The compatibility of different IDRs is thought to determine which proteins can participate in a particular condensation process and which are excluded. Similarly, the physical size restriction posed by the mesh-like structures that are formed upon multivalent interactions of proteins in a condensate determines the specificity of the condensate composition. Condensate dynamics are suggested to be tuned by PTMs, by the abundance of charges in the solvent, mainly in form of RNA, and by protein concentrations. Similar to the negative charges of RNA molecules, PTMs will also alter the local charge, the local structure and compactness around the modification and thereby affecting the forces that mediate sequence-specific phase separation (Boeynaems et al., 2018).

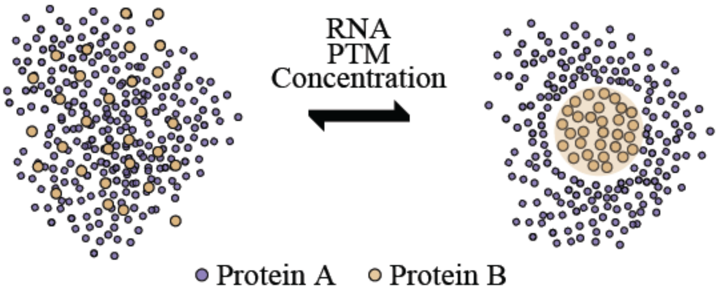

Figure 3.6.2: Regulators of phase separation.

The heterotypic interaction of Protein A and B is favorable over homotypic interactions until PTMs, RNA or protein concentration are altered to an extend that make homotypic interactions of protein B favorable over heterotypic interactions, or vice versa.

3.7 The ubiquitin system

PTMs are covalent modifications of proteins that occur during or after synthesis. By regulation of subject stability, activity, localization, or interaction, PTMs greatly increase the complexity and functionality of the cellular proteome (Chen and Kashina, 2021; Conibear, 2020).

Besides phosphorylation, methylation and acetylation, ubiquitylation is one of the most common modifications and was initially discovered in the context of protein degradation (Hershko et al., 1982). Ubiquitin molecules are small, 76 amino acid long peptides. Apart from its role in proteolysis, ubiquitylation controls various vital processes and pathways including autophagy, trafficking, DNA damage response, cell cycle control and apoptosis (Damgaard, 2021). The ubiquitylation of a target protein requires a reaction cascade that involves three classes of enzymes, the E1 (activation), E2 (conjugation) and E3 (ligation). The E3-ligases mediate substrate specificity of the ubiquitylation cascade and are divided into three types: RING-, HECT- and RBR-ligases. While the class of RING E3-ligases functions only as adapter between Substrate and E2 enzyme, HECT and RBR E3-ligases form a stable intermediate with the ubiquitin molecule before transferring it onto the substrate (Figure 3.7.1a).

The transfer can occur either to a lysine residue (K) on the substrate, resulting in mono-ubiquitylation, or to a lysine residue on a ubiquitin that is already attached to a substrate resulting in polyubiquitin-chains.

In the process of forming polyubiquitin-chains, the position of the lysine residue in the previous, already attached ubiquitin molecule that is used for a further ubiquitylation dictates the resulting chain-linkage type (K6, K11, K27, K29, K33, K48, K63). Additionally, several heterotypic and branched chain-linkages have been observed, as well as poly-ubiquitylation via methionine on ubiquitin itself (Figure 3.7.1b). All types of ubiquitylation are reversible and the deubiquitylation reaction is catalyzed by deubiquitylating enzymes (DUBs) with subsequent recycling of the cleaved ubiquitin molecules (Damgaard, 2021; Tracz and Bialek, 2021).

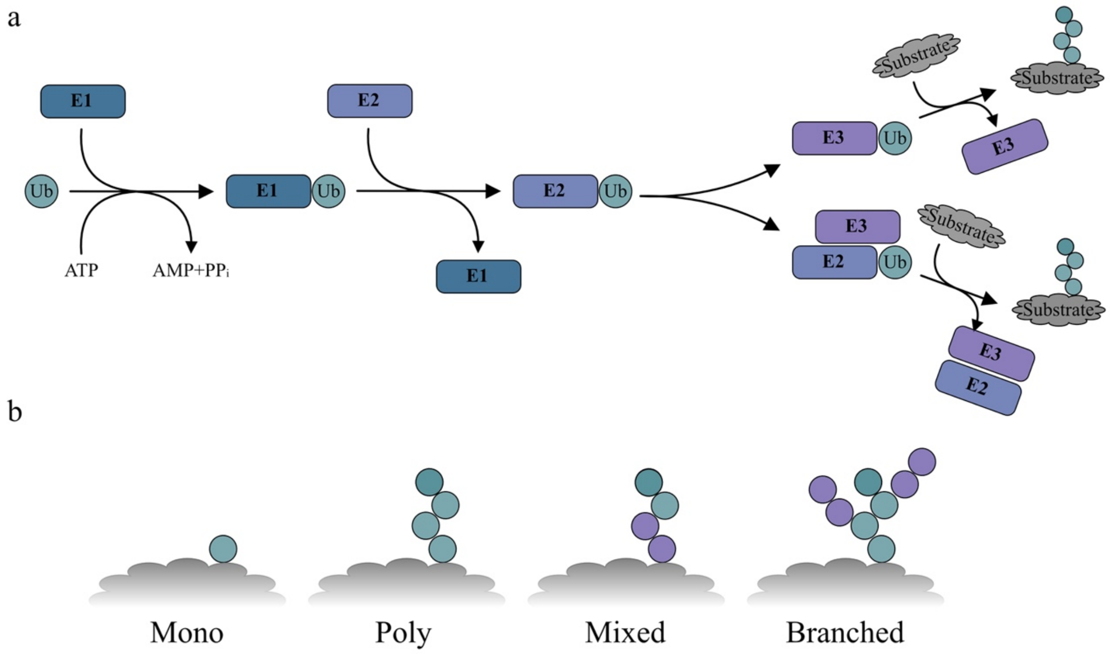

Figure 3.7.1: Sequential cascade of the ubiquitylation reaction and ubiquitylation types.
(a) Ubiquitin (Ub) is attached in an ATP-dependent reaction to the E1 enzyme and subsequently transferred to the E2 enzyme. Depending on the class of E3 enzyme, the Ub is first conjugated to the E3-ligase prior to transfer or directly transferred from the E2 enzyme to the substrate with the E3-ligase functioning only as mediator. (b) Exemplary ubiquitin chain types.

The variety of ubiquitin linkage types is referred to as "ubiquitin code" that propagates a specific set of cellular functions that will be briefly highlighted in the following paragraph.

K6-linked chains mediate mitophagy through the Parkin E3-ligase with USP8 and USP30 as respective DUBs (Cunningham et al., 2015; Durcan et al., 2014) and control DDR as shown for the BRCA1-BARD1 complex (Wu-Baer et al., 2003). Additionally, K6-linked chains can induce target degradation but also stabilization (Hong et al., 2018; Yuan et al., 2020) and prime substrates for structural remodeling by the ATPase VCP by HUWE1 (Heidelberger et al., 2018; Michel et al., 2017). More recently, a role of K6-linke ubiquitylation in enhancing chromatin affinity was reported (Zhang et al., 2020).

K11-linked chains are frequently found as branched chains with K48 and induce proteasomal degradation of its substrates; several cell cycle regulators are subjected to K11-linked ubiquitylation and thus show a direct role of K11-linked chains in cell cycle progression (Meyer and Rape, 2014).

K27-linked chains regulate NF-κB and IRF pathways and E3-enzymes that modify their substrates with K27-linked chains are the family of TRIM ligases, NEDD4 and RNF168, to name only a few.

K29-linked ubiquitylation has roles in neurodegenerative disorders, repression of Wnt/β-catenin signaling, proteasome regulation and epigenetics (Swatek and Komander, 2016; Tracz and Bialek, 2021).

AREL1 was the first E3-ligase published to generate polyubiquitylation in a K33-linked manner, which mediates intracellular trafficking (Swatek and Komander, 2016).

The most abundant polyubiquitin chain-type, K48-linked, marks its substrates for degradation by the proteasome. In contrast, K63-linked chains, the second most abundant form of polyubiquitin chains, have a role in kinase activation, cellular trafficking and DNA repair with the observation, that K63-linked chains can directly bind to DNA (Liu et al., 2018).

3.7.1 The E3-ligase HUWE1

The E3-ligase HUWE1 (HECT, UBA and WWE domain containing E3 ubiquitin protein ligase 1) belongs to the class of HECT ligases and comprises 4374 amino acids and a size of 482 kDa. Alternatively, HUWE1 is referred to as Mule, ARF-BP1, HECTH9, URE-B1 or LASU1 which in some cases reflects the initially discovered substrates of this E3-ligase. MYC was one of the first identified substrates, along with p53 and Mcl1. But since then many further target proteins have been identified with roles in cell cycle checkpoint decisions, protein quality control and DDR (Kao et al., 2018).

The HECT domain of HUWE1 is located near its C-terminus and consists of a N-lobe and a C-lobe. The N-lobe mediates interaction with the E2 enzyme, while the C-lobe contains the catalytic cysteine that forms a stable intermediate with the ubiquitin molecule prior to its transfer onto the substrate. The N-termini of HECT E3-ligases differ significantly and are thought to confer substrate and linkage specificity. Due to the size and high content of disordered regions of the N-terminus (54.87%, PONDR VSL-2), most studies investigating the function of HUWE1 made use of constructs that lack large parts of the protein. Only recently the structure of the full-length protein has been resolved (Hunkeler et al., 2021). This study identified further interaction domains in addition to the already known, conserved domains UBA, WWE and BH3. These additional domains may provide specificity for an even broader spectrum of substrates by mediating low-affinity interactions.

As discussed before, HUWE1 has been identified as a major cellular K6-ligase and targets MYC for non-proteolytic ubiquitylation (Adhikary et al., 2005; Heidelberger et al., 2018; Michel et al., 2017).

3.8 MYC and the ubiquitin system

The ubiquitin system is a key regulator of cellular processes. Therefore, it is not surprising that MYC, a protein with major regulatory functions in the cell, is highly targeted and controlled by the ubiquitin system.

The majority of the more than 18 known E3-ligases ubiquitylate their substrate to promote their subsequent degradation by the proteasome (Sun et al., 2021). The half-life of MYC, which is about 30 minutes, is also controlled by the ubiquitin system. However, the ubiquitin system not only controls protein stability but also the functional activity of MYC, both, in an activating or repressive manner (Figure 3.8.1). Several mechanisms have been published to explain how the ubiquitin system controls

MYC functions, including protein destabilization and functional repression, protein destabilization and functional activation, protein stabilization and activation as well as protein stabilization and repression (Chen et al., 2019). Representative examples are introduced in the following paragraph.

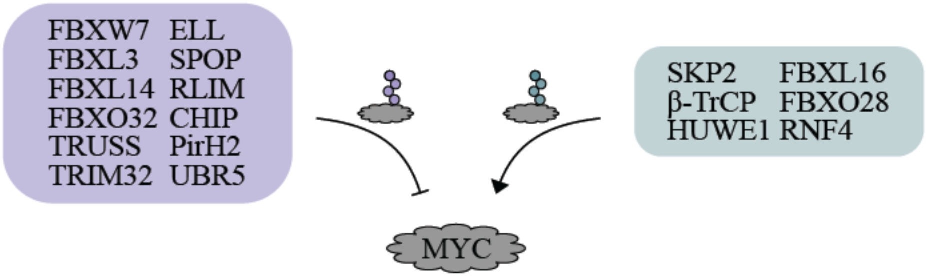

Figure 3.8.1: MYC and the Ubiquitin System.
List of E3-ligases that repress MYC-function by ubiquitylation, visualized by the bar, and E3-ligases stimulating MYC activity by ubiquitylation, visualized by the arrow. Substrate receptors shown for SCF (Skp1/Cul1/F-box protein) complexes. Data derived from Chen et al. (2019) and Sun et al. (2021).

FBWX7 is one of the best studied E3-ligases of MYC. It primes MYC for degradation by the proteasome in a K48-linkage specific manner. As the substrate receptor, FBXW7 is part of a SCF complex and mediates binding to substrates in a phosphorylation dependent manner. The FBWX7 degron of MYC is centered around T58 and has been recently extended to a second site around T244 and T248; phosphorylation of T58 is controlled by the GSK3 kinase and promoted by S62 phosphorylation, while the kinases for the second degron are still unknown (Welcker et al., 2004a; Welcker et al., 2004b; Welcker et al., 2022).

FBWX7 directed proteolysis of MYC is antagonized by the deubiquitylating enzymes USP28 and USP36 and also by the E3-ligase β-TrCP which recognizes a motif highly similar to the FBXW7 phosphodegron but instead assembles heterotypic K11-, K33-, K63- and K48 polyubiquitin chains that stabilize the MYC protein (Popov et al., 2010).

Like FBXW7, SKP2 is part of a SCL complex and primes MYC for proteasomal degradation. However, SKP2 mediated ubiquitylation simultaneously increases MYC activity inducing cell cycle progression and MYC associated transcription (Kim et al., 2003; von der Lehr et al., 2003). This phenomenon gave rise to the model of transcription-coupled proteasomal degradation. While the ubiquitylation of MYC is thought to be K48-linked, SKP2 has been shown to commonly mediate K63-linked ubiquitylation of substrates (Lee et al., 2015).

Similar to the effects of SKP2 HUWE1 is required for the activity of MYC but with only little influence on protein stability (Adhikary et al., 2005; Peter et al., 2014). Corresponding to this observation, the linkage-type of deposited ubiquitin chains on MYC by HUWE1 was shown to be non-proteolytic and a recent study provides evidence for K6-linked ubiquitylation of MYC by HUWE1 at K148 (Heidelberger et al., 2018). These findings are in line with evidence provided in this thesis.

3.9 Aim of this study

The aim of this study was to elucidate on the spatial and temporal control of the choice between the different functional groups of MYC interactors and the resulting consequences for cellular functions.

First, the role of the ubiquitin system in regulating interactions of MYC with partner proteins, particularly the PAF1 complex, was assessed. Therefore, an initial siRNA screen was conducted to identify E3-ligases that regulate the interactions between MYC and the PAF1 complex. Subsequently, downstream effects in presence or absence of the respective E3-ligase were investigated.

Second, there are several lines of evidence predicting that MYC has the ability to phase separate and, as a consequence of that, to mediate substantial parts of its interactome via multivalent interactions. To investigate this hypothesis, a compound screen was performed that aimed at finding stimuli capable of inducing a phase transition phenotype. The screen was followed by studies to determine the subsequent changes in the interactome and the resulting effects on MYC function.

Given the indications that ubiquitylation of MYC can regulate interactions with partner proteins, which is analyzed and described in the first part of this thesis, the influence of ubiquitylation on phase transition and downstream effects was an additional subject of this project.

4 Results

This thesis comprises two projects. The first project (chapter 4.1) follows the hand-over model of the PAF1c from MYC onto RNAPII (Jaenicke et al., 2016) and defines this ubiquitin driven step as essential in transcription-coupled double-strand break repair. Parts of the results of this project have been published in Endres et al. (2021). The second project (chapter 4.2) describes the ability of MYC proteins to multimerize in response to transcription and replication stress. Multimerization prevents accumulation of DSBs and enables proliferation in presence of these oncogenic stressors. The results of this project will be published in Solvie et al. (*in press*). The status of the manuscript was by the time of submission of this thesis *in press*.

4.1 Ubiquitylation of MYC couples transcription elongation with double-strand break repair at active promoters

4.1.1 HUWE1 drives the transfer of PAF1c from MYC onto RNAPII

Previous data indicated that ubiquitylation of MYC is a control mechanism regulating transcription. Specifically, the rapid handover of the PAF1 complex from MYC onto RNAPII depends on MYC ubiquitylation (Jaenicke et al., 2016).

4.1.1.1 Screen for E3-ligases controlling MYC-function at promoters

To further explore the role of the ubiquitin system in the transfer process, I investigated the accumulation of the intermediate MYC-PAF1, a structural and functional core subunit of the PAF1c, at promoters by an siRNA screen in U2OS$^{\text{MYC-tet-on}}$ cells targeting MYC-associated E3-ligases followed by proximity ligation assay (PLA) as readout. The Targets were selected based on published interactomes of MYC and MYCN (Baluapuri et al., 2019; Buchel et al., 2017). Out of 29 E3-ligases, the knock-down of 14 targets significantly enhanced the proximity between MYC and PAF1 (Figure 4.1.1a). To focus on E3-ligases influencing the proximity of MYC and PAF1 specifically at core promoters, the results were overlaid with a complementary screen between PAF1 and Ser5-phosphorylated RNAPII (pS5), which is mainly found on promoters. The knock-down of three E3-ligases resulted in significantly increased proximity between PAF1 and pS5. HUWE1 was the only E3-ligase that scored in both approaches (Figure 4.1.1a).

I confirmed the specificity of the PLA approach by controls that are visualized in Figure 4.1.1b; an siRNA targeting MYC, the absence of MYC induction (low MYC) and a single antibody control (1AB) depleted the PLA signal. In line with published results, inhibition of the proteasome using the inhibitor

MG-132 increased proximity between MYC and PAF1. Similarly, the depletion of the significant hit HUWE1 enhanced the assessed proximity, which was confirmed by visual inspection (Figure 4.1.1b,c).

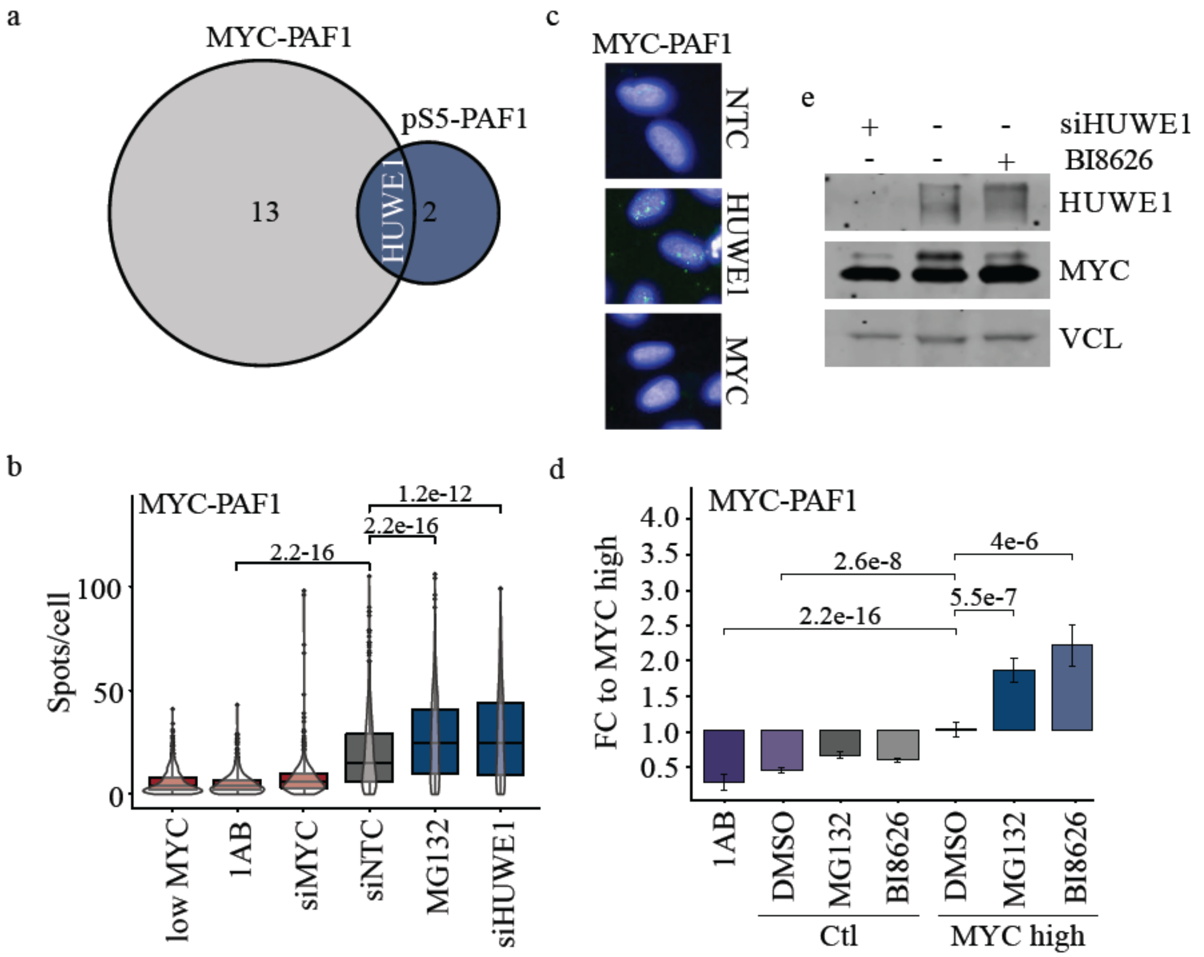

Figure 4.1.1: Screen for E3-ligases controlling MYC-function at promoters.

(a) Venn diagram summarizing the results of the PLA-siRNA screen investigating protein knock-down enhancing the proximity between the indicated proteins in U2OS cells in presence of oncogenic MYC levels (Dox: 1µg/ml, 24 hrs). Number of siRNAs significantly enriching proximity shown (n=10, FDR<0.05). (b) Box plot overlayed with violine plot to visualize distribution of PLA signals for indicated siRNAs of the screen in (a) (n=10). MG-132 (20 µM, 4 hrs) serves as positive control. Two sided Mann-Whitney U test relative to siNTC derived from data measured across 10 independent experiments. (c) Representative pictures of selected results from (a,b). (d) Box plot of PLA between MYC and PAF1 in U2OS cells expressing Dox inducible MYC (U2OS$^{MYC\text{-}tet\text{-}on}$). Where indicated ("MYC high") Dox was added for 24 hrs, MG-132 (20 µM), BI8626 (10 µM) and NVP2 (1 µM) was added for 4 hrs (n=3). 1AB refers to control samples containing solely the anti-PAF1 antibody. Two sided Mann-Whitney U test. (e) Immunoblot of the indicated proteins in RIPA extracts of U2OS cells, 40 hrs post transfection with siRNA targeting HUWE1 or 24 hrs incubation with BI8626 (10 µM) (n=4). Parts of this figure appear in a similar form in Endres et al. (2021).

To validate these results, I utilized a published HUWE1-inhibitor, BI8626, (Peter et al., 2014) which gave similar results to siRNA mediated depletion in PLA assays (Figure 4.1.1d). The signal specificity was ensured by previously described controls. All PLA assays were conducted in presence of oncogenic MYC-levels by induction of MYC with doxycycline.

Immunoblots ensured that neither depletion of HUWE1 by siRNA nor inhibition of HUWE1 function resulted in changes in steady state levels of MYC and thereby influenced the outcome of the assays that were discussed above (Figure 4.1.1e).

4.1.1.2 Characterization of the HUWE1-inhibitor BI8626

Previous characterization of BI8626 ensured its specificity for HUWE1 versus other HECT-E3 ligases *in vitro* and its function on transcription in colon carcinoma (Peter et al., 2014). To better characterize BI8626 *in cellulo* the effect on ubiquitylation of all cellular peptides was measured by SILAC-based ubiquitin remnant profiling (Kim et al., 2011; Xu et al., 2010a) and compared to depletion of HUWE1 by siRNA in U2OS cells. The cells were harvested for downstream processing 24 hrs after treatment with BI8626 and 48 hrs after transfection with siRNA targeting HUWE1. 1,825 ubiquitylated sites were identified across quadruplicates with a significant correlation between inhibition and depletion of HUWE1 which is shown in form of a scatter plot (Figure 4.1.2a). Notably, ubiquitylation sites on HUWE1 that are indicated in red were only downregulated upon depletion. Besides these differential effects on the HUWE1 protein, only very few sites differed significantly (FDR<0.005) between BI8626 and siHUWE1. The results are shown as a volcano-plot (Figure 4.1.2b).

Taken together, these experiments validate BI8626 as specific inhibitor for HUWE1 with similar effects to HUWE1 depletion by siRNA *in vivo*.

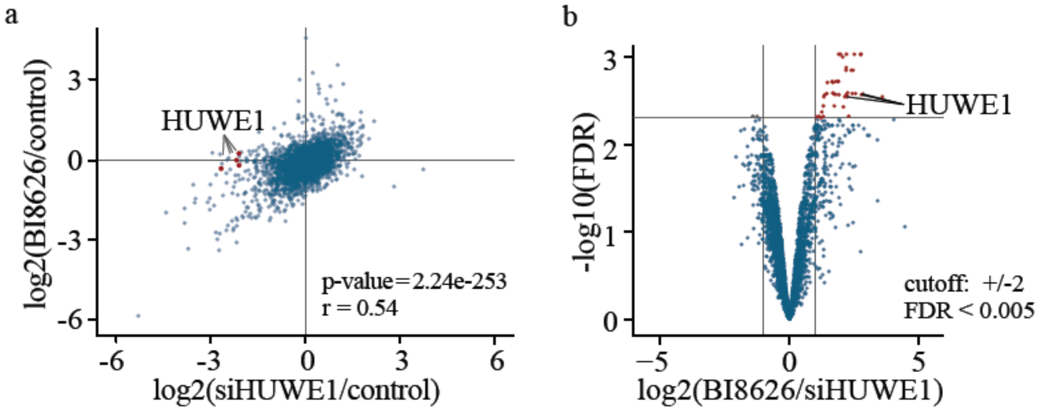

Figure 4.1.2: Characterization of BI8626 by ubiquitin profiling.

(a) SILAC Based Ubiquitin Remnant Profiling experiment quantifying ubiquitylation sites after siRNA targeting HUWE1 (48 hrs; x-axis) or HUWE1 inhibitor BI8626 treatment (10µM, 24 hrs; y-axis) compared to control condition. The plot shows a representative experiment as scatter plot. Highlighted sites represent ubiquitylation sites identified on HUWE1 and r represents Pearson correlation (n=4). (b) Volcano plot showing a direct comparison of BI8626 and siRNA targeting HUWE1 of normalized data across all replicates and corresponding significance. Data set corresponds to (a). Indicated sites represent ubiquitylation sites identified on HUWE1 (n=4). Parts of this figure appear in a similar form in Endres et al. (2021) and were produced in collaboration with Jan Heidelberger.

4.1.1.3 MYC accumulates on core promoters upon HUWE1 inhibition

MYC accumulates on promoter regions when ubiquitylation of MYC is inhibited (Jaenicke et al., 2016). I confirmed this notion with the results from the PLA-siRNA screen presented in chapter 4.1.1.1.. Consistently, chromatin immunoprecipitation (ChIP) indicated increased occupancy of MYC promoter sites, here shown for the *Nucleolin* gene upon HUWE1 inhibition (Figure 4.1.3a).

In line with the role of ATPase p97 in removal of MYC from chromatin in a HUWE1 dependent manner (Heidelberger et al., 2018), treatment with the p97-inhibitor NMS-873 increased MYC occupancy at promoters to a similar extend as HUWE1 inhibition (Figure 4.1.3a).

In order to assess MYC responses on a genome-wide level, I subjected U2OS$^{\text{MYC-tet-on}}$ cells to ChIP-Rx-sequencing. Inhibition of HUWE1 function for 4 hours increased MYC occupancy at the core promoters of all expressed genes in presence of oncogenic MYC levels (MYC high) as a metagene analysis revealed (Figure 4.1.3b). In presence of physiologic MYC levels the occupancy increased only moderately.

Taken together, the results suggest HUWE1 dependent ubiquitylation to prime MYC for dissociation from the chromatin. Evidence suggests a p97-dependent extraction.

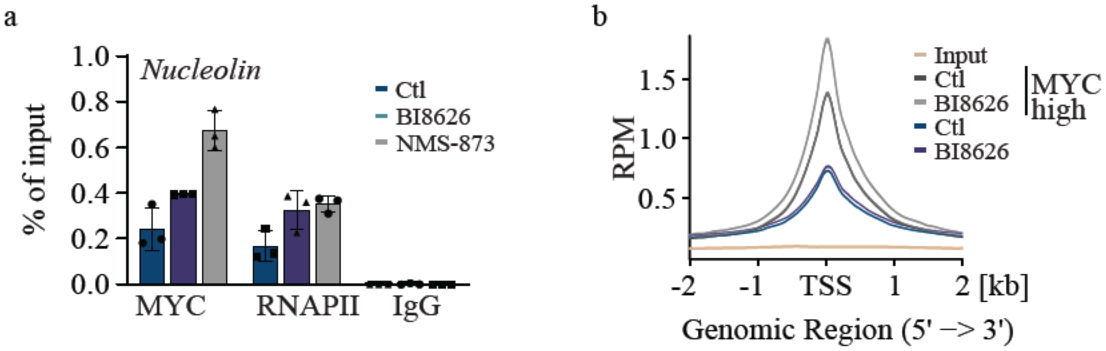

Figure 4.1.3: MYC accumulates on core promoters upon HUWE1 inhibition.

(a) Representative MYC and RNAPII ChIP-qPCR in U2OS cells upon treatment with BI8626 (10 µM, 4 hrs) and NMS-873 (10 µM, 4 hrs) of the Nucleolin promoter region. Data show mean +/- S.D. of technical triplicates (n=2). (b) Density plot of MYC in a ChIP-Rx experiment in U2OS$^{\text{MYC-tet-on}}$. The plots show density profiles centered on the TSS of all active promoters. Cells were treated with Dox for 24 hrs (MYC high) and BI8626 (10 µM, 4 hrs) as indicated (n=1). Parts of this figure appear in a similar form in Endres et al. (2021).

4.1.1.4 HUWE1 inhibition diminishes MYC effect on PAF1c and elongating RNAPII

The data presented in the previous chapters suggest HUWE1 as major driver of the PAF1c hand-over model and therefore on subsequent effects in transcriptional regulation of MYC (Jaenicke et al., 2016). Hence, I explored possible effects of HUWE1 inhibition on PAF1 and RNAPII chromatin distribution using ChIP-Rx-sequencing.

My investigation of genome wide responses of RNAPII to MYC induction revealed no changes at the promoter regions of all expressed genes in metagene analysis of ChIP-Rx-sequencing experiments in

U2OS$^{MYC\text{-}tet\text{-}on}$ cells (Figure 4.1.4a, RNAPII Ctl). In presence of HUWE1 inhibition, RNAPII accumulated at promoters in response to MYC induction (Figure 4.1.4a, RNAPII BI8626).

The elongating form of RNAPII (pS2) showed increased occupancy throughout all expressed genes upon induction of MYC (Figure 4.1.4b, pS2 Ctl). Inhibition of HUWE1 function abolished this increase (Figure 4.1.4b, pS2 BI8626).

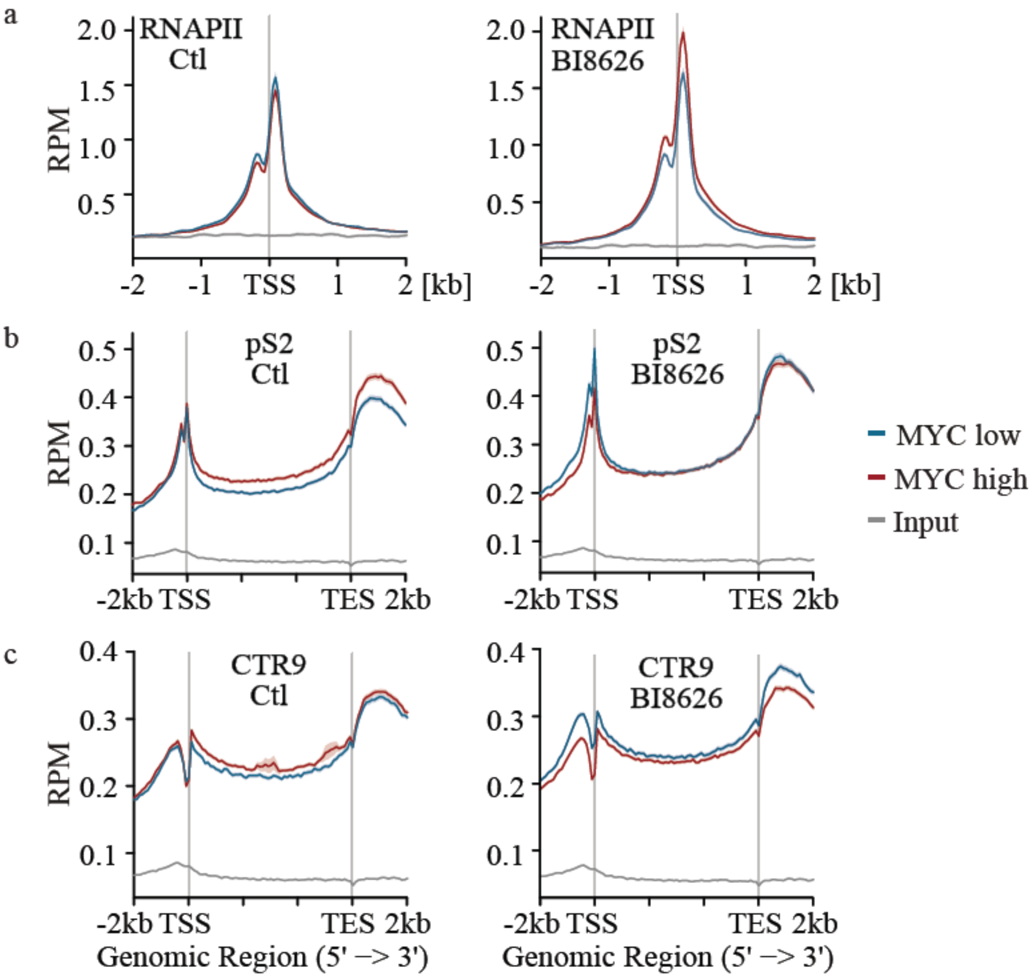

Figure 4.1.4: HUWE1 inhibition diminishes MYC effect on PAF1c and elongating RNAPII.

(a) Metagene plot of total RNAPII in a ChIP-Rx experiment in U2OS$^{MYC\text{-}tet\text{-}on}$. The plots show metagene profiles of all active promoters (n=17,674) with (MYC high) or without (MYC low) addition of Dox (24 hrs) in control (DMSO-treated) cells or cells exposed to BI8626 (10 µM, 4 hrs) (n=2). (b) Metagene plot of pS2 RNAPII in a ChIP-Rx experiment. Plots and conditions are as in (a) (n=2). (c)Metagene plot of CTR9 in a ChIP-Rx experiment. Plots and conditions are as in (a) (n=2). Parts of this figure appear in a similar form in Endres et al. (2021).

In parallel to the behavior of pS2, I observed an increased association of CTR9, a core subunit of the PAF1c, with chromatin throughout all expressed genes in presence of oncogenic MYC levels (Figure 4.1.4c, CTR9 Ctl). The inhibition of HUWE1 led to a decreased chromatin association of CTR9 upon MYC induction below the abundance of CTR9 in presence of physiological MYC levels (Figure 4.1.4c, CTR9 BI8626).

I conducted the ChIP-Rx-sequencing experiments in presence of oncogenic MYC levels and, where indicated, 4 hours of HUWE1 inhibition in order to assess imminent effects of HUWE1 function on the distribution of respective proteins on chromatin.
These results indicate that HUWE1-mediated ubiquitylation of MYC acts as a control mechanism which impacts transcription via the transfer of the PAF1c from MYC onto RNAPII.

4.1.2 MYC and HUWE1 promote global histone H2B ubiquitylation

As introduced in chapter 3.4.4, the PAF1 complex interacts with the E3-ligase RNF20-RNF40 and ubiquitylates histone H2B at K120 (Van Oss et al., 2016). Due to the effect of MYC and HUWE1 on PAF1c transfer, I explored the ubiquitylation state of histone H2B in response to changes in MYC and HUWE1 abundance or function.

4.1.2.1 Assessment of H2B ubiquitylation by immunoblotting

In order to investigate changes on the ubiquitylation of histone H2B I made use of two approaches. First, I inspected cellular H2B ubiquitylation levels by immunoprecipitation of all ubiquitylated peptides and subsequent immunoblotting for histone H2B in U2OS$^{MYC\text{-}tet\text{-}on}$ cells. In presence of physiological MYC levels, H2B was barely detectable in lysates after ubiquitin-immunoprecipitation. This is in contrast to a strong increase in abundance of H2B after ubiquitin-immunoprecipitation upon MYC induction (Figure 4.1.5a). The incubation of cells with BI8626 abolished the presence of H2B in lysates after ubiquitin-immunoprecipitation in presence of oncogenic MYC levels.

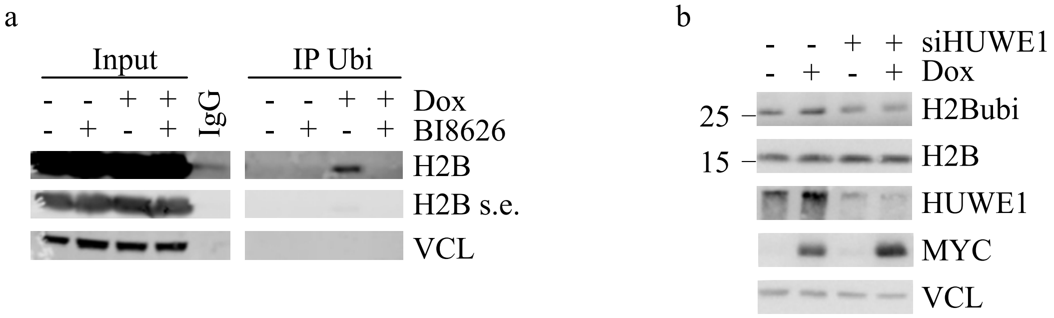

Figure 4.1.5: Assessment of H2B ubiquitylation by immunoblotting.
(a) Immunoprecipitation using an anti-ubiquitin antibody (FK2) from U2OS$^{MYC\text{-}tet\text{-}on}$ cells. Input shows 1% of the material used in the immunoprecipitation (n=2). A shorter exposure (s.e.) was chosen to visualize total H2B levels. Treatment with Dox (24 hrs) and BI8626 (10 µM, 4 hrs) as indicated. (b) Immunoblot documenting ubiquitylation of H2B in U2OS$^{MYC\text{-}tet\text{-}on}$ cells 40 hrs post transfection with control siRNA or siRNA targeting HUWE1. Dox was added as indicated. Parts of this figure appear in a similar form in Endres et al. (2021).

Second, I utilized a ubiquitylation sensitive antibody for H2B (K120 specific) to assess cell lysates without affinity purification. I confirmed a MYC-driven increase in H2B ubiquitylation at K120 in a HUWE1 dependent manner, as shown by immunoblot (Figure 4.1.5b). H2B total levels remained constant while the immunoblot for HUWE1 confirmed depletion by siRNA and the immunoblot for MYC validated the induction of MYC.

4.1.2.2 ChIP-Rx-sequencing of ubiquitylated H2B

To confirm the ubiquitylation changes of H2B on a genome wide level, I conducted ChIP-Rx-sequencing and investigated the chromatin distribution of H2B and of the ubiquitylated H2B (K120, H2Bubi). U2OS$^{\text{MYC-tet-on}}$ cells were treated with Dox to induce MYC in presence as well as in absence of HUWE1 function.

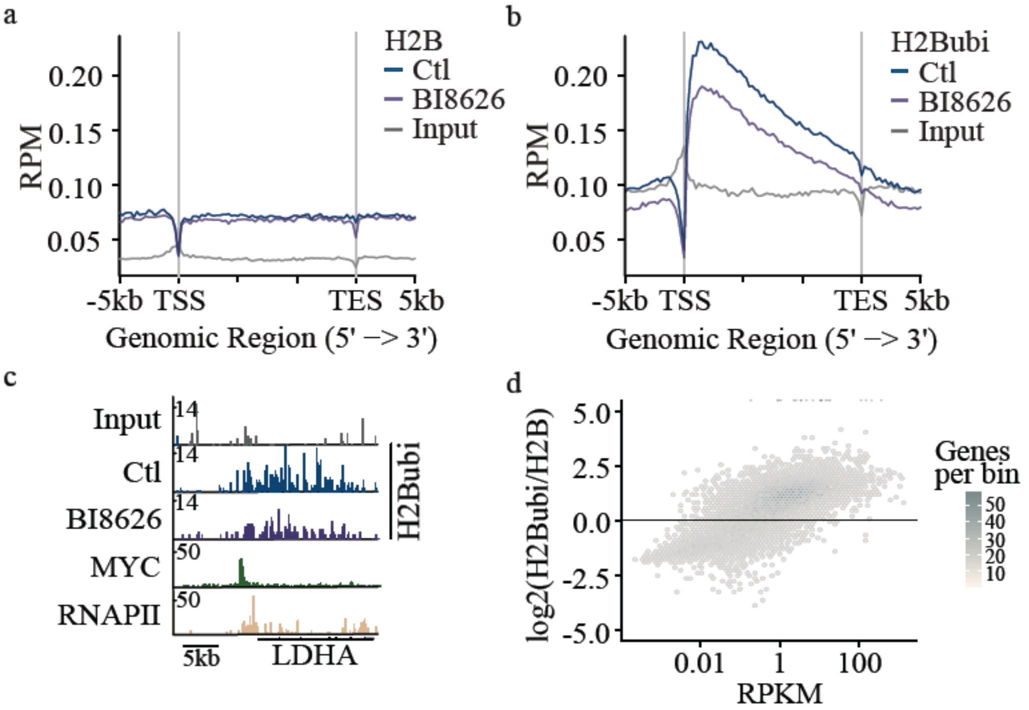

Figure 4.1.6: Analysis of H2B and ubiquitylated H2B chromatin distribution.

(a) Metagene plot over all expressed genes of a ChIP-Rx experiment of H2B in U2OS$^{\text{MYC-tet-on}}$ cells in presence of oncogenic MYC levels. Where indicated, treatment with BI8626 (10 µM, 4 hrs) (n=2). (b) Metagene plot over all expressed genes of a ChIP-Rx experiment of ubiquitylated H2B ("H2Bubi") in U2OS$^{\text{MYC-tet-on}}$ cells. Treatment as in (a) (n=2). (c) Representative browser tracks of the LDHA locus of ChIP-Rx experiments from (a) and (b). (d) Density plot depicting dependency of H2B ubiquitylation calculated by the fold change of H2Bubi over H2B reads (y-axis) for each gene on respective gene expression level (x-axis, log10 scale). Data for H2Bubi and H2B from (a) and (b), gene expression data from poly(A)-RNA-sequencing of U2OS$^{\text{MYC-tet-on}}$ in presence of oncogenic MYC levels, performed by Leonie Uhl. Parts of this figure appear in a similar form in Endres et al. (2021).

Inhibition of HUWE1 had no effect on the distribution of H2B in its total form which remained evenly distributed across genomic regions as shown by metagene analysis of all expressed genes (Figure 4.1.6a). BI8626 treatment suppressed the abundance of H2Bubi compared to the untreated condition (Figure 4.1.6b). The decrease was confirmed by visual inspection of browser tracks as shown for the *LDHA* locus (Figure 4.1.6c). The overlay of H2Bubi tracks with tracks from MYC and RNAPII ChIP-

Rx-sequencing experiments (Figure 4.1.3, Figure 4.1.4) exemplarily showed the correlation of H2B ubiquitylation with MYC binding. Additionally, the absence of H2Bubi signal at the nucleosome free region at the TSS confirmed the signal specificity.

Reviewing the H2Bubi abundance relative to total H2B abundance per gene in correlation to gene expression displayed a linear relationship (Figure 4.1.6d). This is in line with the correlation of H2B ubiquitylation and RNAPII occupancy and processivity (Hou et al., 2019).

From these observations I conclude that MYC enhances global H2B ubiquitylation at K120 in a HUWE1 dependent manner.

4.1.3 MYC-promotes double-strand repair in transcribed regions

Ubiquitylation of H2B supports both, transcriptional elongation and DNA damage repair (Moyal et al., 2011). With respect to the role of MYC in regulation of H2B ubiquitylation, I investigated subsequent roles of MYC in DNA damage repair. For this, etoposide, a topoisomerase II specific inhibitor, was used to induce dose-dependent DNA breakage (Chen and Liu, 1994).

4.1.3.1 MYC alleviates cellular effects of topoisomerase inhibition

Etoposide inhibits topoisomerase II, which relieves torsional stress that is caused by the transcription fork and induces DSBs. These are either a result of a direct collision of the inhibited topoisomerase II-DNA complex with the transcription or replication fork, or a result of transcription-replication collisions due to changes in DNA supercoiling (Tammaro et al., 2013; Xiao et al., 2003). The consequences are reduced DNA synthesis and proliferation (see chapter 3.5).

I assessed respective effects of etoposide treatment by quantitative cell cycle immunofluorescence and assigned cycle phases based on DNA content (Hoechst) and DNA synthesis (EdU-incorporation). Within three hours of treatment, the percentage of cells actively synthesizing DNA decreased from approximately 60% down to 7% in cells with physiological MYC levels. Treatment of cells 24 hours after MYC induction resulted in a smaller decrease in DNA-synthesizing cells, down to 27%. This is illustrated in the scatter plot and quantified in the form of pie-charts (Figure 4.1.7). The MYC induction alone had neglectable effects on DNA synthesis.

Considering the effects of MYC induction on H2B ubiquitylation and the relieve of cellular effects that are caused by topoisomerase inhibition, I hypothesized that MYC prevents accumulation of induced DSBs.

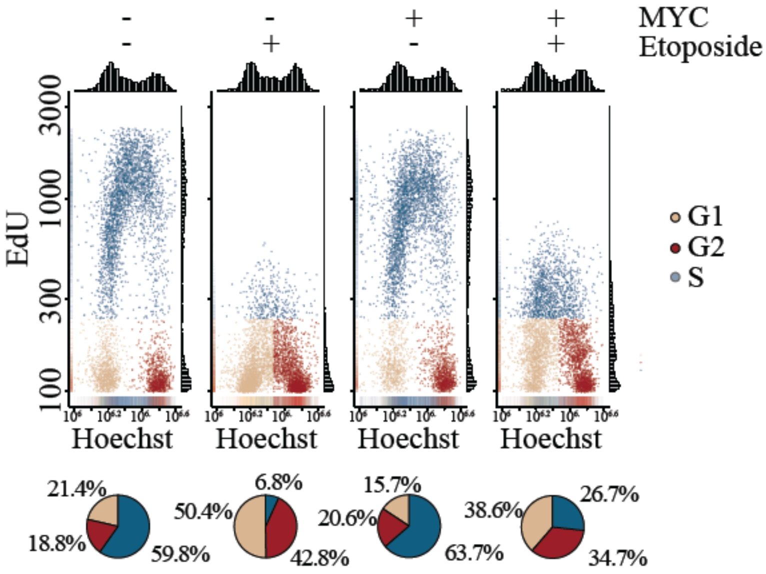

Figure 4.1.7: MYC induction restores etoposide-induced DNA synthesis suppression.

(top) Cell cycle distribution and EdU incorporation in U2OS$^{MYC\text{-}tet\text{-}on}$. Dox (24 hrs) and etoposide (25 µM, 3 hrs) were added as indicated (n=3). 5,000 cells per condition of a representative replicate are shown. (bottom) Pie chart visualizing the cell cycle distribution of cells shown in (top). Parts of this figure appear in a similar form in Endres et al. (2021).

4.1.3.2 MYC prevents double-strand break accumulation at transcribed genes

To verify whether MYC induction prevents accumulation of etoposide induced DSBs, I applied a DSB-sequencing protocol that was based on Breaks Labelling In Situ and Sequencing (BLISS) (Yan et al., 2017).

The protocol was extended by an additional digestion step with the rare-cutting restriction nuclease AsiSI prior to protocol start (BLISS8). In silico digestion predicts more than thousand AsiSI recognition sites, while only 100-200 are accessible in cells (Clouaire et al., 2018). The number of reads after sequencing in these defined areas is used to normalize the samples.

I validated the BLISS8 protocol by examining the predicted restriction sites by browser tracks (Figure 4.1.8a) and global quantification which is illustrated in the bar graph (Figure 4.1.8b). Direct comparison with non AsiSI-restricted samples exhibited a highly specific signal at restriction sites that were predicted by *in silico* digestion within a window of 100 base pairs, irrespective of the localization within genic or intergenic regions.

A metagene analysis revealed a basal number of DSBs occurring at actively transcribed genes (Figure 4.1.8c, left, Ctl) immediately downstream of the transcription start site, as indicated by the overlay with RNAPII ChIP-Rx-sequencing data. This observation is in line with previous publications on transcription induced double-strand breaks (Madabhushi et al., 2015) and independent of MYC induction. Weakly expressed genes are devoid of DSBs (Figure 4.1.8c, right). Contrasting, the accumulation of DSBs at actively transcribed genes upon etoposide treatment is completely rescued by MYC induction (Figure 4.1.8c, left, Etoposide). To a similar extend double-strand breaks that accumulate upon etoposide treatment in antisense-direction were rescued.

In line with the role of H2Bubi in co-transcriptional DDR, I was able to show that MYC limits genomic instability in presence of transcription and possibly replication dependent DSB induction.

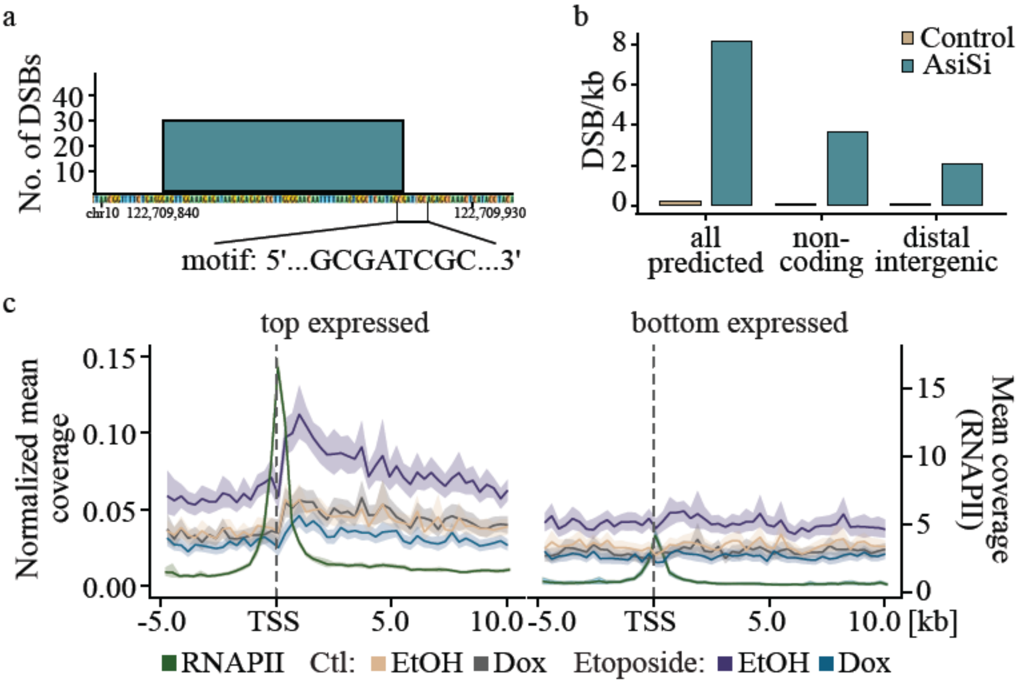

Figure 4.1.8: MYC prevents double-strand break accumulation at transcribed genes.

(a) Browser track of AsiSI-induced DSBs in BLISS8 at exemplary in silico predicted AsiSI recognition sites. (b) Box plot of BLISS8 reads of AsiSI treated and untreated samples at in silico predicted AsiSI recognition sites; respective categories include all predicted sites, only non-coding sites and distal intergenic sites. (c) Density plot showing normalized mean coverage and estimated confidence interval of double-strand breaks (BLISS8) and total RNAPII (ChIP-Rx-seq) around the transcription start sites of top (n=3954; left) and bottom (n=3012; right) expressed genes in U2OS$^{MYC\text{-}tet\text{-}on}$. Treatment as indicated with Dox (24 hrs) and etoposide (25 µM, 3 hrs). RNAPII data for overlay of respective regions derived from Figure 4.1.4. Parts of this figure appear in a similar form in Endres et al. (2021).

4.1.4 Summary of the data presented in context of co-transcriptional stress resilience.

Ubiquitylation of MYC is essential for its effect on transcriptional elongation (Jaenicke et al., 2016). The data presented in the previous chapter show a rapid transfer of PAF1c from MYC onto RNAPII mediated by HUWE1. This step controls MYC-dependent transcription elongation. Simultaneously, the chromatin structure is altered by MYC and HUWE1 through stimulation of histone H2B ubiquitylation in favor of transcription elongation as well as DSB repair. For this reason, I concluded that MYC couples transcription elongation and DSB repair to prevent genomic instability of MYC-driven tumor cells (Figure 4.1.9).

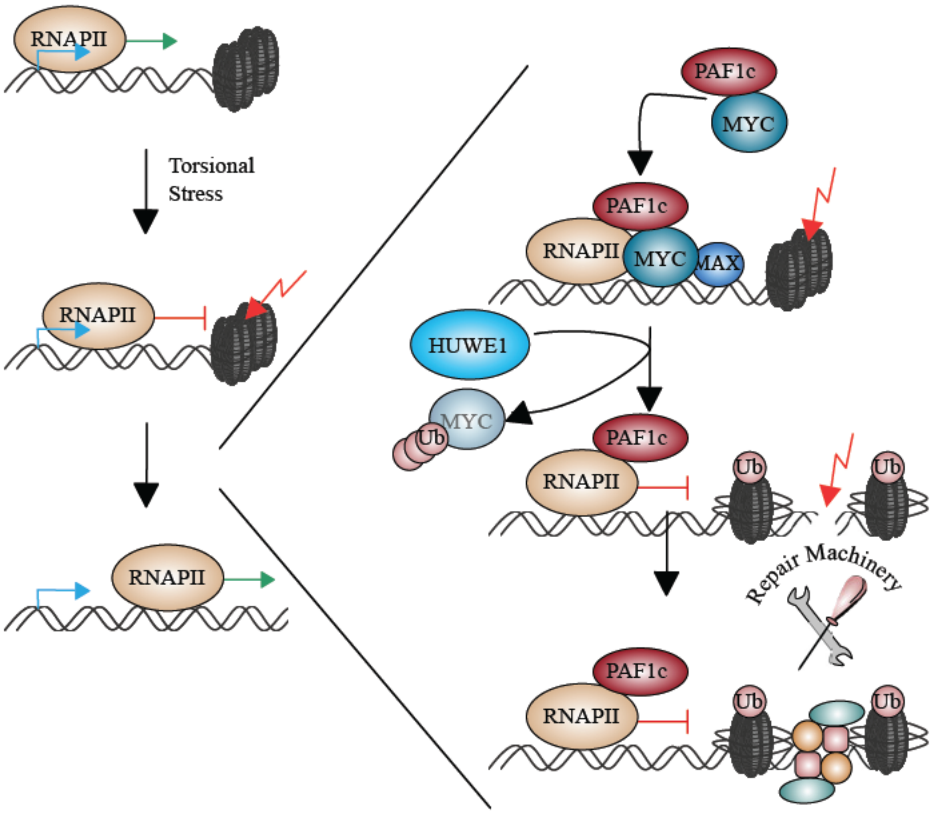

Figure 4.1.9: Model of HUWE1 mediated transfer of PAF1c from MYC onto RNAPII.

Model summarizing the findings on HUWE1 mediated transfer of PAF1c from MYC onto RNAPII. Parts of this figure appear in a similar form in Endres et al. (2021).

4.2 MYC multimers shield stalled replication forks from RNA polymerase

4.2.1 Multimerization of MYC

The MYC protein contains multiple highly disordered regions, which increase the probability of multivalent intra- and intermolecular contacts. Multivalency is a natural driver of oligomeric and polymeric assemblies (Banani et al., 2017). In agreement, the ability of MYC to multimerize has been observed *in vitro* (Boija et al., 2018) and consequently gives rise to the question of multivalent interactions, phase separation and its consequences for the MYC protein *in cellulo*. I explored these hypotheses in context of the second part of this thesis.

4.2.1.1 MYC proteins form foci in cellulo

The resolution limit of optical microscopy is dictated by the wavelength of light and resides between 200 – 500 nm. At this resolution MYC shows a homogenous distribution throughout the nucleus, only sparing nucleoli (Figure 4.2.1a). However, an increase in the resolution down to 20 nm utilizing direct stochastic optical reconstruction microscopy (dSTORM) (van de Linde et al., 2011) revealed a throughout focal distribution of MYC in unperturbed cells (Figure 4.2.1b). The quantification demonstrated that up to 14% percent of all MYC molecules reside in foci that were composed of more than 100 molecules. A cumulative density function visualizes the quantification of MYC distribution (Figure 4.2.1c), which significantly differs from controls of homogenously distributed signals (simulated) and signals emanating from very diluted MYC antibody.

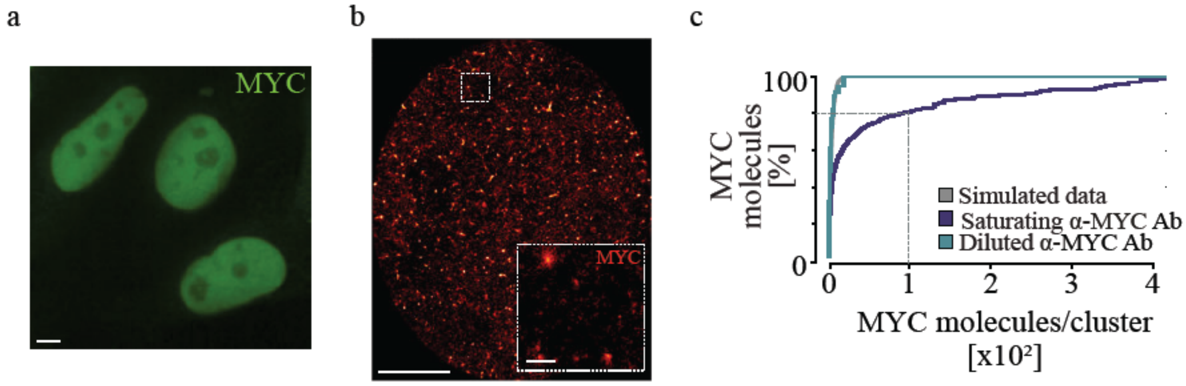

Figure 4.2.1: Heterogenous distribution of MYC in unperturbed cells.

(a) Immunofluorescence picture of MYC in unperturbed U2OS cells. Scale bar: 1 µm. (b) Direct stochastic optical reconstruction microscopy (dSTORM) using MYC antibody Y69 in unperturbed U2OS cells at saturated labeling conditions. Scale bar: 5µm. Inset is a zoom-in. Scale bar: 1 µm. (n=7 cells). Probability density functions for MYC molecules per cluster in unperturbed U2OS cells under saturating (purple) and diluted (blue) antibody labeling conditions and in data simulating a single-molecule distribution (grey). Inset: Signal distribution at <10 MYC molecules per cluster (n=7 cells). (b) performed by Apoorva Baluapuri and Marvin Jungblut, (c) performed by Sören Doose. Parts of this figure appear in a similar form in Solvie et al. (in press).

4.2.1.2 MYC proteins form foci in response to perturbation of transcription or ubiquitin system

To investigate the stimulus that is underlying the foci formation, a small molecule screen was conducted. In context of this screen, I tested several compounds with following targets: the Aurora-A kinase, cell cycle regulators, components of the DDR, apoptotic pathways, PP1, the splicing machinery, the topoisome, several key factors in the transcription machinery, and the ubiquitin-proteasome system. The interference with the ubiquitin-system in form of proteasome inhibition (MG-132 and RA-190) or USP7 inhibition (P22077) significantly enhanced foci formation. To a similar extend, interference with transcription elongation by inhibition of the FACT complex (CBL0137) and splicing (PlaB) resulted in increased foci numbers as visualized by a bar graph which is grouped by functionality of the compound targets (Figure 4.2.2a). To detect the enhanced foci formation of MYC I utilized the Harmony High Content Imaging and Analysis Software; an example of the applied algorithm is displayed in Figure 4.2.2b. Visual inspection confirmed the screen results which displayed a wide range of size and structure of induced foci within each condition and cell. I obtained similar results by enhancing foci formation with heat-shock, which was identified in a screen of physiological stressors (Solvie et al., *in press*) (Figure 4.2.2c).

The on-target effects of the inhibitors were confirmed by siRNA depletion of the PlaB target *SF3B1*, the proteasome subunit *PSMA3* and the FACT complex subunit *SUPT16H* as shown by representative images and quantification (Figure 4.2.2d).

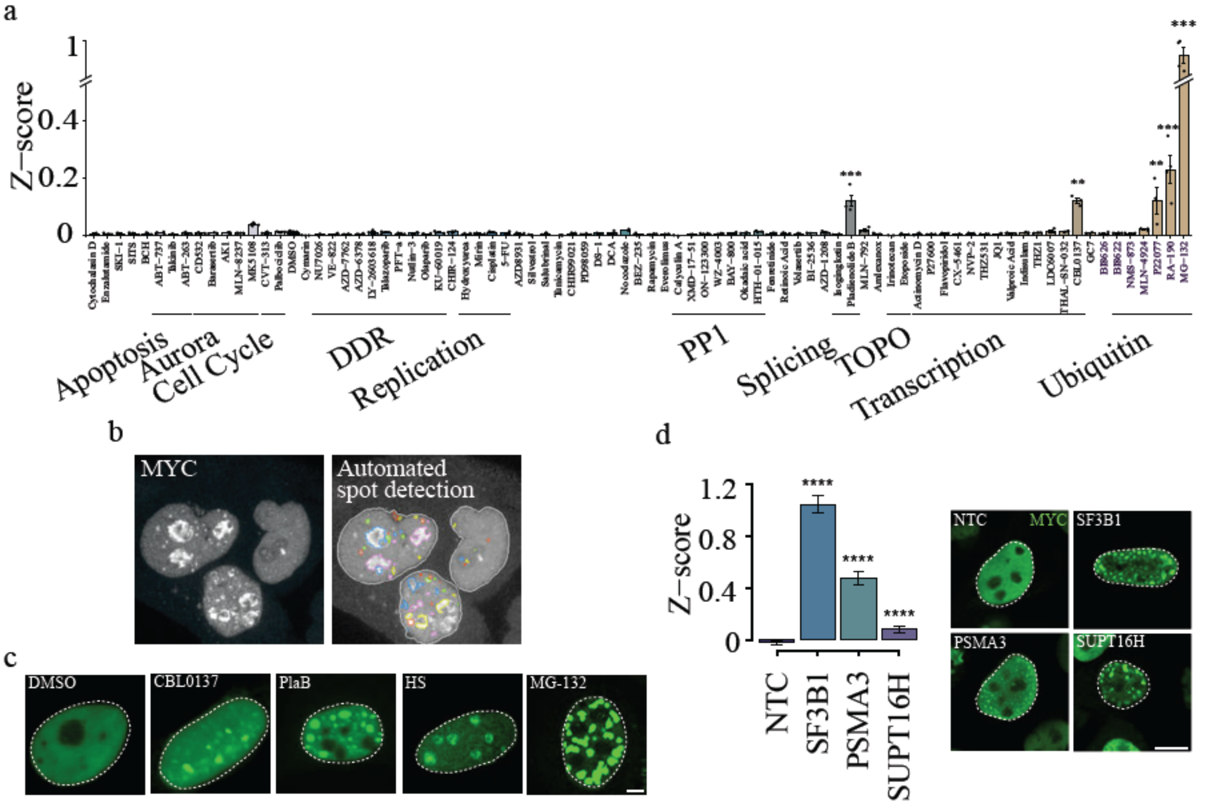

Figure 4.2.2: MYC proteins form foci in response to perturbation of transcription or ubiquitin system.

(a) Bar plot quantifying small molecule screen in U2OS$^{MYC\text{-}tet\text{-}on}$ *cells (Dox 24 hrs). Treatment with indicated compounds for 4 hrs. Shown are Z-scores for biological replicates with mean ± S.E.M. Grouping according to targets (DDR: DNA damage response, TOPO: Topoisome). At minimum, 500 cells were analyzed in each condition per replicate (n=3). For statistics, Mann-Whitney U, two-sided, was applied. (b) Representative example of automated spot detection. (c) Immunofluorescence pictures of MYC in U2OS*$^{MYC\text{-}tet\text{-}on}$ *cells treated with Dox (24 hrs) and Pladienolide B (PlaB, 1 µM), CBL0137 (5 µM), MG-132 (20 µM) for 4 hrs or heat shock (HS: 42°C, 30 min). Scale bar: 1 µm (n=8). Parts of the experiment were performed by Leonie Uhl. (d) Validation using siRNAs in U2OS*$^{MYC\text{-}Tet\text{-}On}$ *cells (Dox, 24 hrs). Multimers per nucleus assessed by immunofluorescence. Shown are Z-score normalized numbers of multimers with mean ± S.E.M. Two sided Mann-Whitney U test to NTC (left). Exemplary pictures (right). Scale bar: 10 µm. Parts of this figure appear in a similar form in Solvie et al. (in press).*

4.2.1.3 Dynamics of MYC foci

The concept of phase separation (see chapter 3.6) is based on dynamic and multivalent interactions and thus phase separated condensates display characteristics which are defined by the nature of these interactions. Among them are high dynamics, rapid exchange with the environment of participating proteins and reversibility. In the following chapter I present data that investigates the stress induced MYC foci in light of those characteristics.

In order to determine the reversibility and dynamics of MYC foci, I removed the enhancing stimulus after four hours of treatment. At indicated time points cells were fixed and processed for immunofluorescence staining of MYC. Subsequently, the foci number was imaged and assessed as introduced in the previous chapter (Figure 4.2.3a). I discovered that all stimuli were reversible except for the splicing inhibitor PlaB, with different half-lives ($T_{1/2}^{CBL0137}$~2 min; $T_{1/2}^{heat-shock}$ ~40 min; $T_{1/2}^{MG-132}$ ~120 min). The CBL0137 induced foci displayed the highest dynamics and formed and dissolved within seconds to minutes. MYC foci induced by heat-shock and MG-132 dissolved within a time frame of 30 minutes to more than 2 hours. I confirmed the experiments by live-cell imaging of U2OS expressing a MYC-eGFP fusion protein (data not shown). Yet, the reversibility of the compounds and their effects is not considered in this experiment and may bias the assumed dynamics significantly.

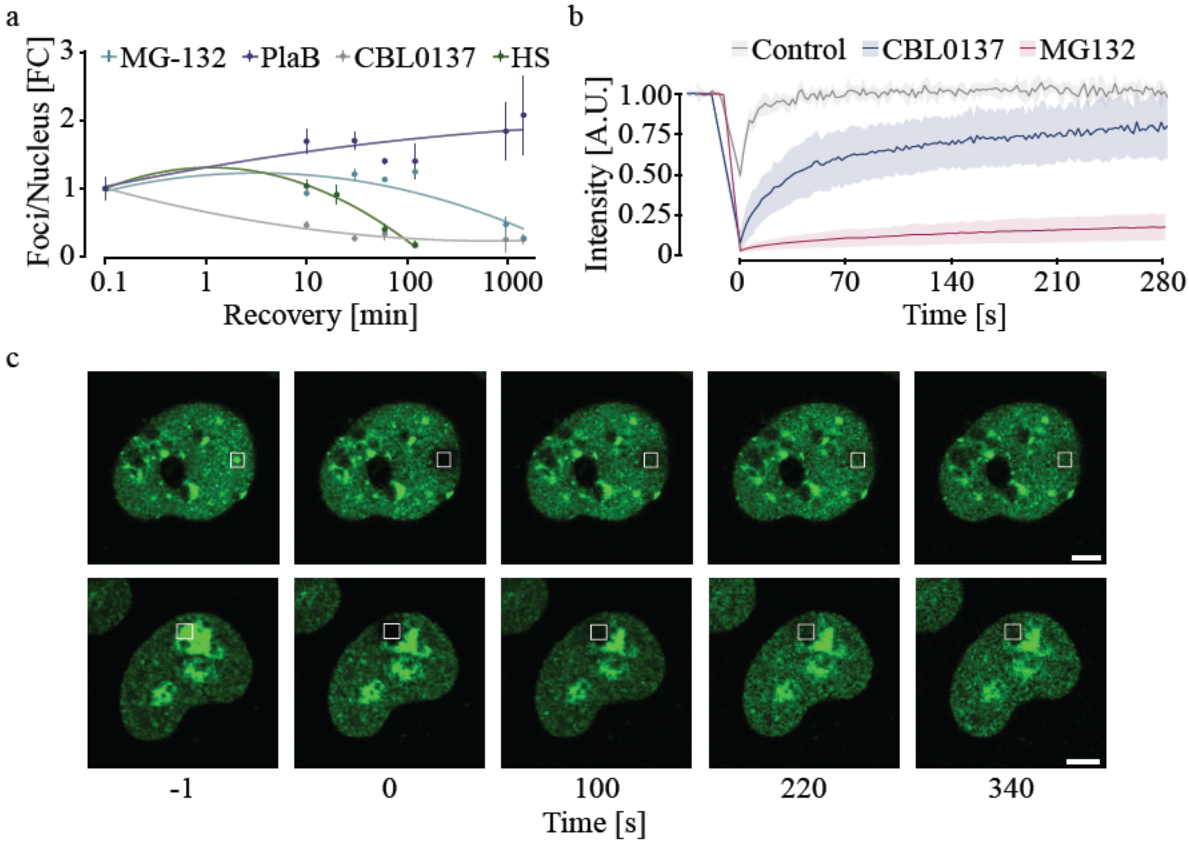

Figure 4.2.3: Dynamics of MYC foci.

(a) Immunofluorescence of U2OS$^{MYC-tet-on}$ cells treated with Dox (24 hrs)), MG-132 (20 µM), CBL0137 (5 µM) and PlaB (1 µM) for 4 hours or HS (42°C for 30 min) prior to removal. Data are mean ± S.E.M. Lines represent a polynomial regression model of 2nd-order (n=3). (b) Quantification of fluorescence recovery after photobleaching (FRAP) experiments of U2OS$^{MYC-eGFP}$ treated with CBL0137 (5 µM, 4 hrs) or MG-132 (20 µM, 4 hrs). Shown are normalized mean +/- S.D (n=3). (c) Representative pictures of FRAP experiments in (b) at indicated time points after photo bleaching of the MG-132 treated condition. Scale bar: 2 µm. Parts of this figure appear in a similar form in Solvie et al. (in press).

The exchange of MYC molecules within foci compared to the remaining nucleus was studied by fluorescence recovery after photobleaching (FRAP). In preparation for this experiment, I infected U2OS cells stably with a lentiviral expression construct of a MYC-eGFP fusion protein (U2OS$^{MYC-eGFP}$).

Upon treatment with MG-132 or CBL0137, MYC foci were inspected by live cell imaging and bleached with a high-powered laser, which destroyed all fluorophores within a defined area. The recovery of fluorescence inside the previously bleached area was measured relative to the intensity in the remaining nucleus. The results displayed a quick recovery after bleaching for CBL0137 induced foci and indicates a rapid exchange of MYC molecules between foci and the surrounding area (Figure 4.2.3b). The recovery of MG-132 induced foci took place to a much lesser extend and did not fully recover after four minutes. The results are quantified in Figure 4.2.3b and confirmed by exemplary images (Figure 4.2.3c). Based on the analyzed data and further results from *in vitro* experiments (data not shown) (Solvie et al., *in press*) I concluded that the stress-induced foci of MYC proteins display all characteristics of liquid-liquid phase separated condensates.

4.2.1.4 MYC foci are sphere-like structures of multimeric MYC

Phase separated compartments can contain two classes of proteins, the “clients” that are recruited subsequent to phase transition or “hosts” that are essential to the phase transition process. In light of this, I investigated whether MYC foci are formed by multimerization of MYC molecules among each other or whether MYC participates in condensation only as a client.

In line with published observations (Boija et al., 2018) the multimerization of MYC *in vitro* was recapitulated using recombinant full-length MYC protein fused to a fluorophore (MYC-mCherry). A fraction of these multimers formed hollow, sphere-like structures (Figure 4.2.4a) and further investigation with dextran molecules of several sizes revealed a mesh-like structure (data not shown) (Solvie et al., *in press*). PLAs between individual MYC proteins and co-immunoprecipitation of differentially tagged MYC confirmed the MYC-multimeric nature of foci *in cellulo* as well as in samples from myeloma patients, previously medicated with the proteasome inhibitor bortezomib (data not shown) (Solvie et al., *in press*).

The sphere-like structures, comprised of a condensed shell and a less dense interior, which were found *in vitro* are commonly found *in cellulo* and exemplarily pictures, recorded by structural illumination microscopy (SIM) are shown in Figure 4.2.4b.

As apparent from visual inspection (Figure 4.2.2 and Figure 4.2.4a,b), MYC multimers occur in a vast variety of sizes. I evaluated the size distribution and found the majority of multimers to occur in a range between 1 and 10 μm^2, thereby covering the size of multimers *in vitro* up to the size of nucleoli (Figure 4.2.4c)

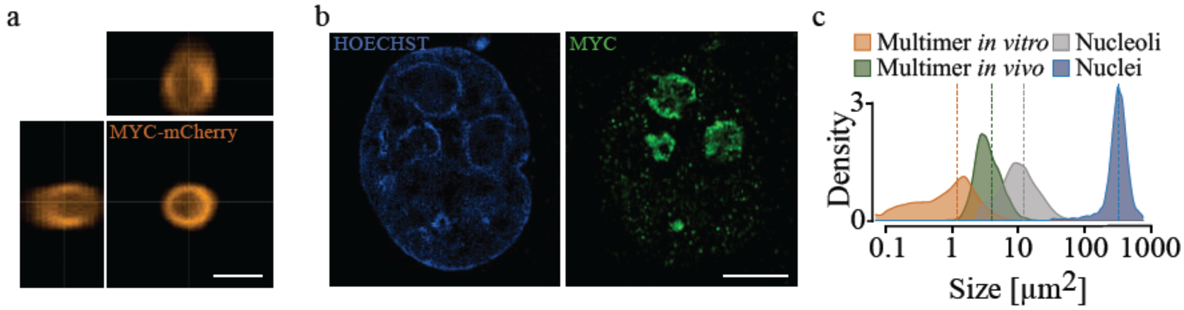

Figure 4.2.4: Morphological characteristics of MYC multimers.

(a) Confocal microscopy showing X-, Y-, and Z-axis views of recombinant MYC-mCherry (16 µM) forming multimeric structures. Scale bar: 5 µm (n=5). Experiment performed by Daniel Fleischhauer. (b) Structured illumination microscopy (SIM) of MYC in U2OS cells treated with MG-132 (4 hrs). Cells are counter stained with DAPI (n=3). Scale bar: 5 µm. Experiment performed in collaboration with Theresa Klein. (c) Histogram of subcellular structures and MYC multimers. The area of MYC multimers in cells induced by MG-132 (20 µM, 4 hrs) is compared to the size of nucleoli, nuclei, and MYC spheres formed in vitro. Dotted line indicates distribution mean. A minimum of 1800 objects were analyzed per compartment. Parts of this figure appear in a similar form in Solvie et al. (in press).

In summary, in the preceding chapters I presented the stress induced potential of MYC proteins to form foci with display characteristics of liquid-liquid phase separated condensates. Further I reported that the formation of MYC foci is driven by homotypic interaction of MYC proteins and thus will be referred to as multimers.

4.2.2 Multimerization changes functional implication of MYC

The composition of cellular compartments, membrane-bound or membrane-less, is dictating their function; in membrane-less compartments composition is thought to be selectively regulated through multivalent interactions between scaffold proteins, and participating clients (Banani et al., 2016). Therefore, I explored the composition of MYC multimers in the following experimental setups.

4.2.2.1 Optical screening of multimer associated proteins

To investigate the biological function of compartments formed by MYC multimers, I screened the co-localization of candidate partner proteins by quantitative high-throughput microscopy (Figure 4.2.5a). Subsequent to induction of multimers, cells were stained by immunofluorescence for MYC to visualize MYC multimers and simultaneously co-stained for the indicated proteins of interest (POI). To visualize the quantified co-localization (PCC) and the corresponding significance for each POI and each treatment, I utilized volcano plots (Figure 4.2.5a).

From these graphs two observations become apparent. First, proteins associated with MYC's function in transcription control significantly co-localize with MYC multimers, namely SPT5, EXOSC10, MAX and MIZ1. I revealed by visual inspection an exclusive localization of the listed proteins in the multimer shell.

Second, several POIs that are involved in binding of stalled replication forks were found to co-localize with the multimeric structures. Those POIs occupied the interior of MYC multimers and were not found in the dense multimer shell; BRCA1 and FANCD2 were identified as such. RAD9 and TopBP1 displayed a similar phenotype but only upon FACT inhibition and heat-shock respectively.

Additionally, I found K48- and K6-linked ubiquitin chains to co-localize with MYC multimers, while several other candidate proteins did not correlate or even anti-correlated with the multimeric structures. Due to the finding that elongating RNAPII (pS2), as well as paused RNAPII (pS5) anti-correlate with MYC multimers (Figure 4.2.5a,b), I concluded that the multimeric structures are not hubs of active transcription.

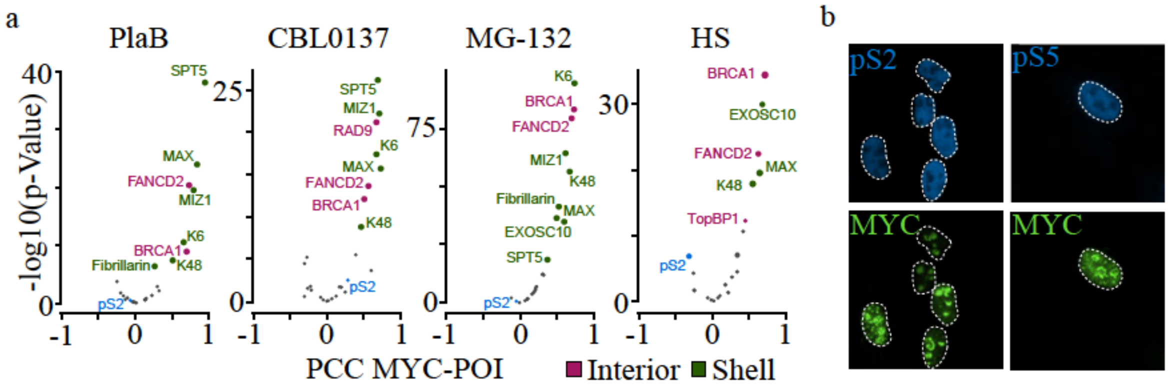

Figure 4.2.5: Optical screening of multimer associated proteins.

(a)Volcano plot of proteins located in MYC multimers upon treatment of U2OS$^{MYC\text{-}Tet\text{-}On}$ cells with Dox (24 hrs), PlaB (4 hrs), MG-132 (4 hrs), CBL0137 (4 hrs) or HS (42°C, 30 min). x axis: Pearson correlation coefficient (PCC) between the partitioning ratio of MYC and of the protein of interest (POI) assessed by quantitative immunofluorescence. p-value is the significance level of Pearson's product-moment correlation t-test, two-sided. Average of 500 cells analyzed per protein. (b) Immunofluorescent pictures of a co-staining of MYC and pS2 or pS5 respectively. Treatment with Dox (24 hrs) and MG-132 (20 µM, 4 hrs). Parts of this figure appear in a similar form in Solvie et al. (in press).

4.2.2.2 MYC multimers protect stalled replication forks

To follow up on the observation that proteins which are associated with stalled replication forks demonstrate affinities towards the multimer interior, I quantified the co-localization with respect to the dense shell or the hollow interior. The results revealed more than 90% of all multimers to stain positive for FANCD2 and BRCA1. Of those multimers with positive co-staining, up to 25% could be determined by the applied algorithm as hollow, sphere-like structures that engulfed the respective protein (Figure 4.2.6a). The quantification of positional co-localization was accomplished as follows and further visualized by an exemplary analysis sequence (Figure 4.2.6b). First, MYC multimers are detected.

These multimers are then assessed for less dense areas on the interior and subsequently divided into border and center region, qualifying the multimer as hollow sphere; if the multimer does not show any detectable structures, it is considered as homogenous.

In the course of additional investigations of factors which are involved in association with stalled replication forks, I revealed the engulfment of phosphorylated ATR (pATR) (Figure 4.2.6a,c) and DNA-PKcs within multimers (data not shown).

Taken together, these results suggest that the majority of all multimers forms at sites of stalled replication forks, with a high tendency to engulf these sites, and not in proximity to sites of active transcription.

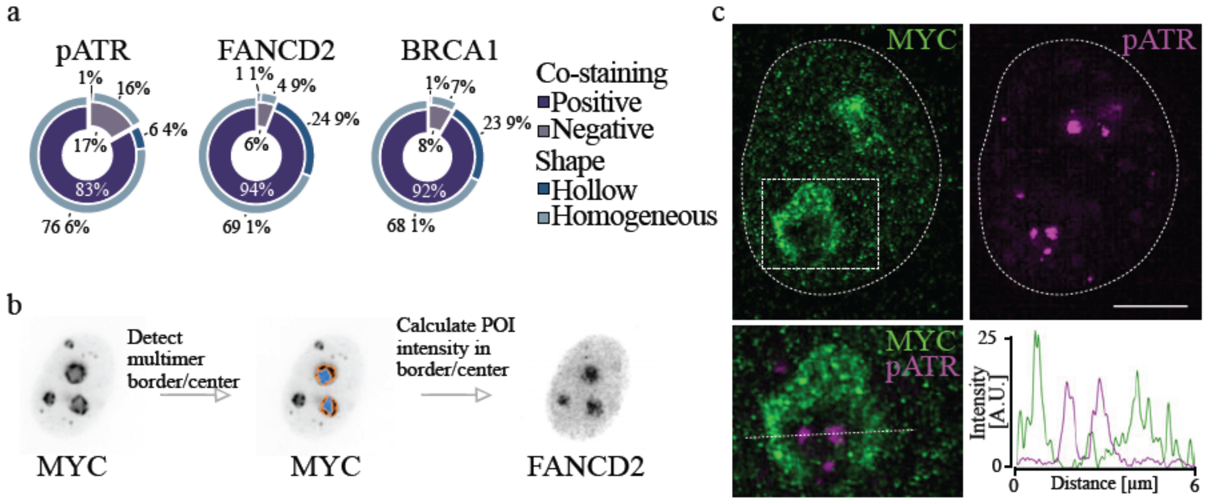

Figure 4.2.6: MYC multimers protect stalled replication forks.

(a) Positional co-localization of indicated proteins with MYC multimers in U2OS$^{MYC\text{-}Tet\text{-}On}$ cells upon treatment with Dox (24 hrs) and MG-132 (20 µM, 4 hrs). Inner circle indicating the proportion of MYC multimers co-localizing with indicated protein. Outer circle indicating proportion of MYC multimers with homogeneous shape or hollow sphere. (b) Illustration of the positional co-localization workflow. (c) Structured illumination microscopy of MYC and pATR in U2OS$^{MYC\text{-}Tet\text{-}On}$ cells (Dox: 24 hrs). Inset shows overlay (left) and scan (right). Scale bar: 5 µm (n=3). Parts of this figure appear in a similar form in Solvie et al. (in press).

4.2.2.3 *MYC multimers form independent of nucleoli*

MYC proteins can accumulate in nucleoli upon inhibition of the proteasome (Arabi et al., 2003). However, the disruption of nucleoli by inhibition of rRNA synthesis with an RNAPI inhibitor (CX-5461) did not influence MYC multimerization, as shown by representative immunofluorescence pictures (Figure 4.2.7a). These results demonstrate that multimerization does not depend on nucleoli formation. Instead, I found that BRCA1 accumulates inside multimers that co-localize with Fibrillarin (Figure 4.2.7b); for this, the three proteins, MYC, the nucleolar marker Fibrillarin, and BRCA1 were co-stained for each cell. Thus, I concluded that co-localization of multimers with nucleolar structures is likely due to DNA damage occurring on the inside of the nucleoli.

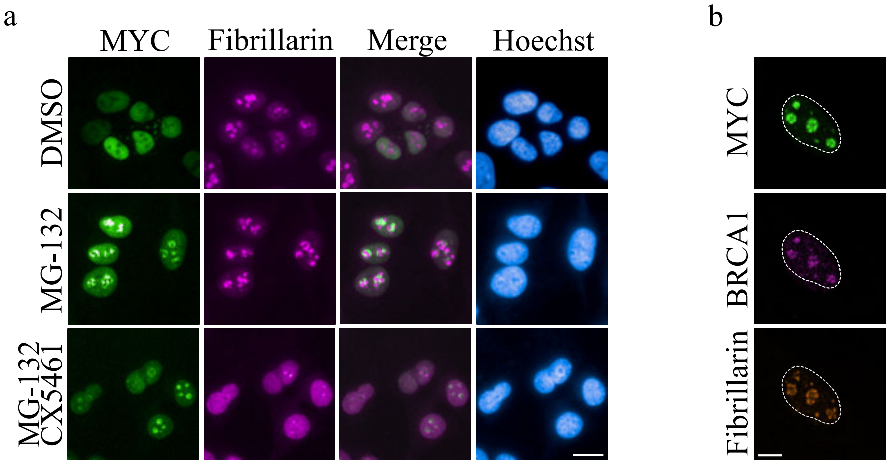

Figure 4.2.7: MYC multimers form independent of nucleoli.

(a) Immunofluorescence of MYC and Fibrillarin upon treatment with Dox (24 hrs), MG-132 (20 µM, 4 hrs) or CX5461 (0.5 µM, 4 hrs) in U2OS$^{MYC\text{-}Tet\text{-}On}$ *cells. Scale bar: 5 µm (n=3). (b) Confocal imaging of triple staining of MYC, BRCA1 and Fibrillarin upon MG-132 treatment (4 hrs, 20 µM) Scale bar: 5 µm (n=3). Parts of this figure appear in a similar form in Solvie et al. (in press).*

4.2.2.4 APEX2-MYC quantitative mass spectrometry

The results of optical screening approaches are limited by the availability of validated and specific antibodies. Approaches that use mass spectrometry (MS) overcome these limitations and are able to quantify large interactomes in an unbiased and highly specific manner. Many MS strategies which are utilized to map interactomes require affinity purification. Affinity purification protocols include cell lysis, fractionation, and purification steps while maintaining protein-protein interactions. However, interactions that are highly dynamic and mediated by multivalency are not preserved in this approach. A strategy to overcome this limitation is covalent labeling of proteins in living cells (Dionne and Gingras, 2022). Hence, I performed spatially resolved quantitative mass spectrometry with the engineered peroxidase APEX2 to screen for multimer associated proteins in an unbiased manner.

First, I established a U2OS cell line stably expressing an APEX2-MYC fusion protein by lentiviral infection (U2OS$^{APEX2\text{-}MYC}$) and subsequently controlled function, localization, and expression of the fusion construct. Accordingly, I incubated the parental U2OS and U2OS$^{APEX2\text{-}MYC}$ cells with biotin-phenol (BP) and pulsed them with hydroxy peroxide (H_2O_2). Subsequently, short-lived biotin-phenoxyl radicals are produced via the oxidation of BP in an APEX2 catalyzed manner. The radical will immanently react with electron rich residues of proximal peptides e.g., tyrosine residues, and thereby covalently tag these peptides with biotin. I corroborated the peroxidase function of the fused APEX2 enzyme by immunofluorescence staining with a fluorescently labeled streptavidin, displaying the presence of immobilized biotin specifically in cells expressing the fusion protein; in absence of BP and H_2O_2 the staining was negative. In line with a specific enrichment of immobilized biotin in MYC multimers, immunofluorescence staining for MYC, and FLAG revealed co-localization of the fusion protein with MYC multimers; the fusion construct contains an additional FLAG-tag (Figure 4.2.8a).

Differences in the interactome of MYC that was generated by proximity labeling disclosed a substantial shift in interactions. The heterodimeric interactome displayed proximity to RNAPII, identified by the subunit POLR2A, and transcription associated factors e.g., HCFC1 and GTF3C1. The interactome that was captured after induction of multimerization by MG-132 treatment reported enrichment of transcription termination factors like the RNA exosome, ribosomal maturation factors, RNA modifiers like YTHDC1, Topoisomerase 2 and proteins well known to undergo phase transition, e.g. FUS (Figure 4.2.8b). These observations are underlined by results from a GO-term analysis (Figure 4.2.8c).

I related the disorder content of all identified peptides in the above discussed interactome study to the disorder content of peptides which were enriched in the absence of foci enhancing stimulus (heterodimeric enriched) as well as to the peptides that were enriched in the presence of foci enhancing stimulus (multimeric enriched). The cumulative density function which I utilized to summarize the results of the predictions displayed a greater content of disordered regions in multimeric enriched proteins compared to all identified proteins. In contrast, the presence of disordered regions was decreased in heterodimeric enriched proteins (Figure 4.2.8d). In detail, more than 40% of all proteins that were identified in the in the multimeric interactome showed a content of least 50% disordered regions. This is only the case for up to 16% of all heterodimeric enriched proteins.

This analysis is in line with the presence of commonly phase separated proteins like FUS in the MYC interactome upon MG-132 treatment and underlines the importance of selective multivalent interactions. These interactions do not only drive the formation of MYC multimers but also dictate a selectivity for participating clients and thereby create a functionally distinct multimer composition. The composition of multimers implies a role of MYC in protection of stalled replication forks, which is significantly different from the functions of the "heterodimeric" MYC at promoter regions in a physiological context.

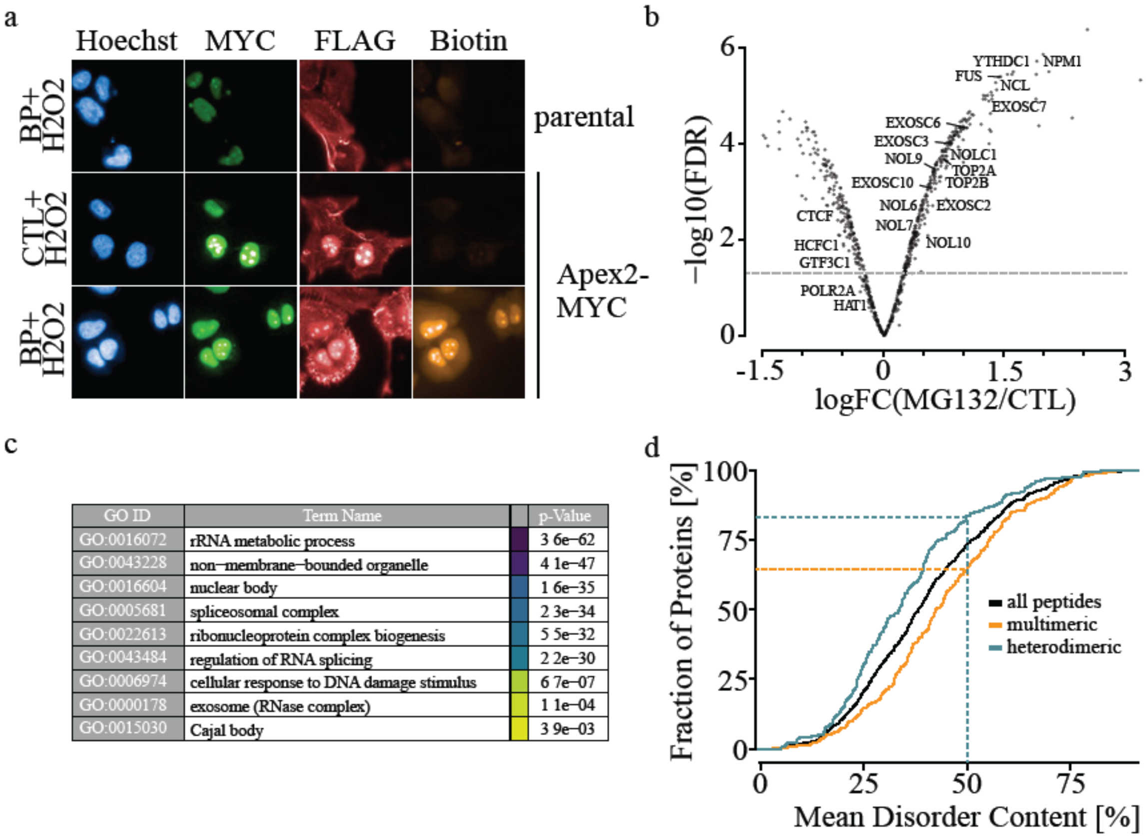

GO ID	Term Name		p-Value
GO:0016072	rRNA metabolic process	🟪	3 6e−62
GO:0043228	non−membrane−bounded organelle	🟪	4 1e−47
GO:0016604	nuclear body	🟦	1 6e−35
GO:0005681	spliceosomal complex	🟦	2 3e−34
GO:0022613	ribonucleoprotein complex biogenesis	🟦	5 5e−32
GO:0043484	regulation of RNA splicing	🟦	2 2e−30
GO:0006974	cellular response to DNA damage stimulus	🟩	6 7e−07
GO:0000178	exosome (RNase complex)	🟨	1 1e−04
GO:0015030	Cajal body	🟨	3 9e−03

Figure 4.2.8: APEX2-MYC quantitative mass spectrometry.

(a) Immunofluorescence pictures of parental U2OS and U2OS$^{APEX2\text{-}MYC}$ cells stained for expression of the APEX2-MYC fusion protein (FLAG), biotinylated proteins and their co-localization with MYC multimers upon induction of the biotinylating (BP: 1 mM, 2 hrs; H_2O_2: 1 mM, 2 min) or control reaction (H_2O_2: 1 mM, 2 min). (b) Volcano-plot of proximity labeling experiment (APEX2) in U2OS$^{APEX2\text{-}MYC}$ cells. Shown are changes in labeling in response to treatment with MG-132 (4 hrs) (n=3). FDR calculated using moderated t-test (Limma package). (c) GO-term analysis of significantly (FDR<0.05) enriched proteins upon MYC multimerization. Hypergeometric p-values with correction for multiple testing using the gSCS algorithm in gprofiler2. Selected GO-terms shown. (d) Cumulative density function of the mean disorder content of peptides identified in the multimeric enriched, heterodimeric enriched or combined interactome. Disorder content predicted using IUPred2A. Parts of this figure appear in a similar form in Solvie et al. (in press).

4.2.3 MYC multimerization is driven by HUWE1-mediated ubiquitylation

4.2.3.1 Biophysical drivers of MYC multimerization

Multivalent contacts are driven by low-complexity regions of a protein (see chapter 3.6); predictions indicate that several regions in the MYC protein may have the ability to mediate such contacts. Owing to these predictions, I sought to determine whether a specific or several IDRs are involved in driving the phase transition process and tested structural mutants for their ability to multimerize.

The tested mutants included deletions of MBs, the C- or N-terminus of MYC, as well as substitution mutants of lysine residues to prevent ubiquitylation of MYC (Figure 4.2.9a). Thus, I transfected U2OS cells with lentiviral expression constructs of respective mutant and assessed the respective behavior based on the introduced tag.

In line with the prediction that imply the majority of the N-terminal region of MYC to consist of IDRs, a mutant lacking the complete N-terminus (ΔN) lost the ability to multimerize upon stimulation with MG-132 (Figure 4.2.9b). Depletion of the very N-terminal TAD domain including MB2 (ΔTAD) impaired the ability of the mutant to form multimers to a lesser extent, likewise to the results reported by a mutant that is lacking all MBs (ΔBox). Deletion of MB2 alone (ΔBoxII) did not display any significant differences in the ability to multimerize compared to the wild type construct, while a deletion of the C-terminus (ΔC) and of MBI (ΔBoxI) led to an increase in the ability of the respective mutants to multimerize.

Similar to the effects that a depletion of the complete N-terminus displayed, a mutant that is devoid of all lysine residues (K-less) rendered MYC proteins incapable of multimerization (Figure 4.2.9b).

Altogether, I concluded that multimerization of MYC relies on the multiplicity of the predicted unstructured regions in the N-terminus and to a similar extend on ubiquitylation of MYC.

To further explore the observation that ubiquitylation is an essential requirement of multimerization *in cellulo*, a SILAC-based ubiquitin remnant profiling experiment was performed. Upon treatment with PlaB, CBL0137 and induction of replication stress (HU) the lysine residues K148 and K389 on MYC were ubiquitylated (Figure 4.2.9c). Consequently, these two lysine residues were reconstituted in the K-less MYC construct ($\text{MYC}^{\text{K-R148KR389K}}$) which restored the ability of the construct to multimerize (data not shown) (Solvie et al., *in press*). These experiments further underlined the importance of ubiquitylation in the regulation of MYC multimerization.

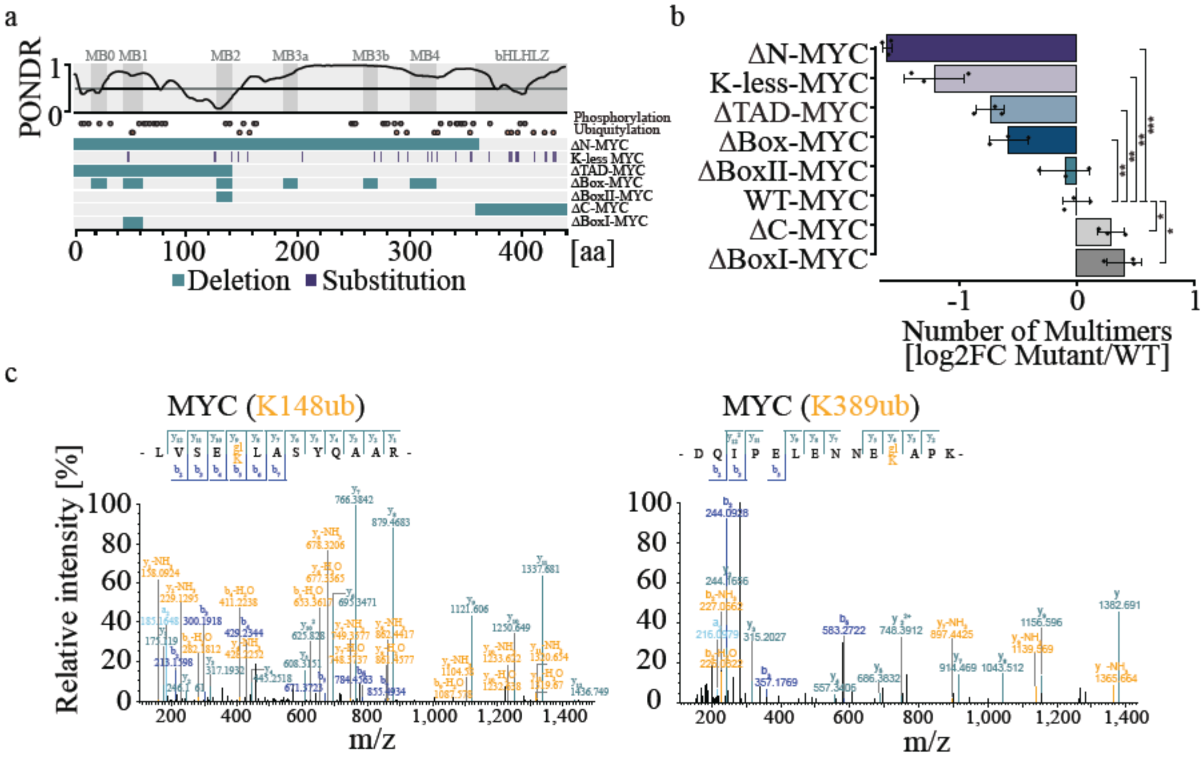

Figure 4.2.9: Biophysical drivers of MYC multimerization.

(a) Graph of predicted disordered domain (PONDR, VSL-2) of the MYC protein with indications of depleted or substituted regions in the MYC-mutants used. (b) Bar graph visualizing multimerization ability of MYC-mutants compared to wildtype MYC (WT) upon MG-132 (20 µM, 4 hrs) treatment. Shown is the mean ± S.D. of three independent experiments. Unpaired t-test, two-sided, was used for comparison to WT-MYC. (c) Representative MS spectrum visualizing MYC ubiquitylation at K148 (left) and K389 (right) in diGLY experiments performed upon treatment with PlaB (1 µM, 2 hrs), CBL0137 (5 µM, 2 hrs) or HU (5 mM, 4 hrs) (n=3). Experiment performed by Ekaterina Isaakova. Parts of this figure appear in a similar form in Solvie et al. (in press).

4.2.3.2 Non-proteolytic ubiquitylation as driver of MYC multimerization

Due to the apparent role of ubiquitylation in the process of phase-transition of MYC, I investigated the possible role of specific chain-linkage types (see chapter 3.7) as explained in the following chapter.

The optical screening approach in Figure 4.2.5 reported the co-localization of K48- and K6-linked ubiquitin chains with multimers shown in form of representative images (Figure 4.2.10a). Contrasting, K63-linked ubiquitin chains were not observed in multimers.

K48- and K6-linked chains have very different functions in cellular and more specifically, in MYC biology. For this reason, I assessed the balance between K48- and K6-linked chains in proximity of MYC during multimer formation by PLAs between MYC and the respective ubiquitin linkage-type; the signals were corrected for the background determined by a respective single antibody control (Figure 4.2.10b). While the abundance of K48-linked chains decreased in proximity to MYC upon multimerization, I observed an increase in the abundance of K6-linked chains. In accordance with this observation, I found two DUBs, USP28 and USP36, to accumulate in proximity of MYC, particularly at sites of multimerization (Figure 4.2.10b,c). Both DUBs are published to antagonize FBXW7-mediated K48-linked ubiquitylation of MYC (Chen et al., 2019).

These results argue for a role of non-proteolytic ubiquitylation as driver of the phase transition of MYC proteins. This is in contrast to the role of K48-specific, proteolytic ubiquitylation of MYC which is actively suppressed during multimerization.

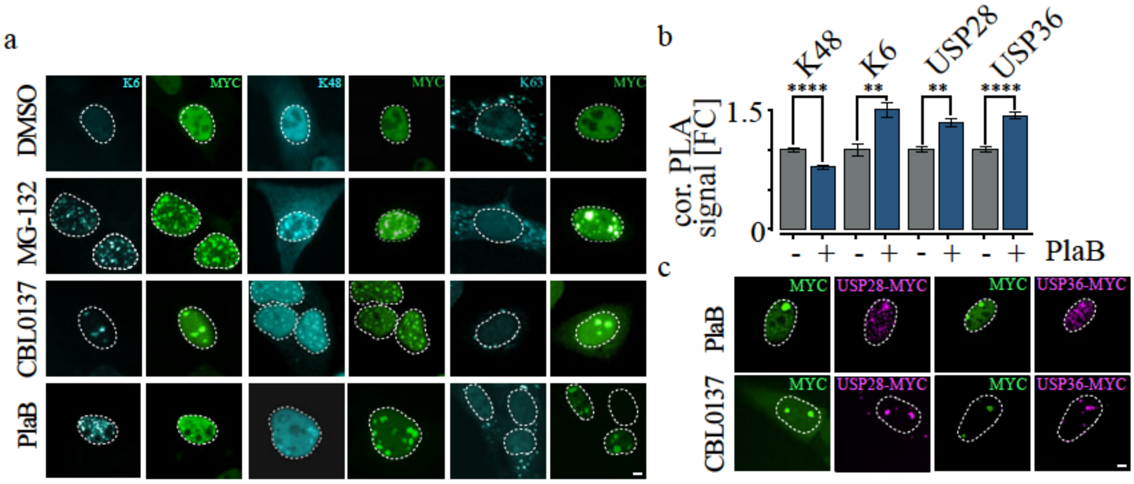

Figure 4.2.10: Non-proteolytic ubiquitylation as driver of MYC multimerization.

(a) Immunofluorescence of MYC multimers and specific ubiquitin chains in U2OS$^{MYC\text{-}Tet\text{-}On}$ cells treated as indicated (Dox: 24 hrs; MG-132: 4 hrs; CBL0137: 4 hrs; PlaB: 4 hrs). Scale bar: 5 µm (n=3). (b) Quantification of PLAs between MYC and indicated proteins in Dox (24 hrs) and PlaB (4 h, 1 µM) treated U2OS$^{MYC\text{-}Tet\text{-}On}$ cells. Signals are corrected for corresponding single antibody control and presented as fold change to untreated. Data are expressed as mean ± S.E.M. Two sided Mann-Whitney U test was used for comparison to untreated cells from data derived from 3 independent experiments. (c) Representative images of confocal immunofluorescence of MYC with USP28-MYC and USP36-MYC PLAs within the same cells at indicated treatments. Scale bar: 5 µm. Parts of this figure appear in a similar form in Solvie et al. (in press).

4.2.3.3 MYC multimerization depends on HUWE1 activity

HUWE1 is a major ligase of K6-linked ubiquitin chains in the cell and a major ligase of MYC, with a proposed specificity for the lysine residue K148 (Heidelberger et al., 2018). In light of these indications, I explored the hypothesis that HUWE1 dependent ubiquitylation of MYC drives multimerization. Therefore, I treated cells with MG-132 to induce multimerization in combination with the HUWE1 inhibitor BI8626. Quantitative immunofluorescence revealed a significant reduction of the multimerization ability of MYC upon HUWE1 inhibition which is shown by representative images and the respective quantification (Figure 4.2.11a). Titration of the HUWE1-inhibitor displayed dose dependent effects of BI8626 on multimerization with a half maximal effect at a concentration of approximately 10 µM. This is consistent with concentrations of BI8626 that are applied in literature (Peter et al., 2014) (Figure 4.2.11b).

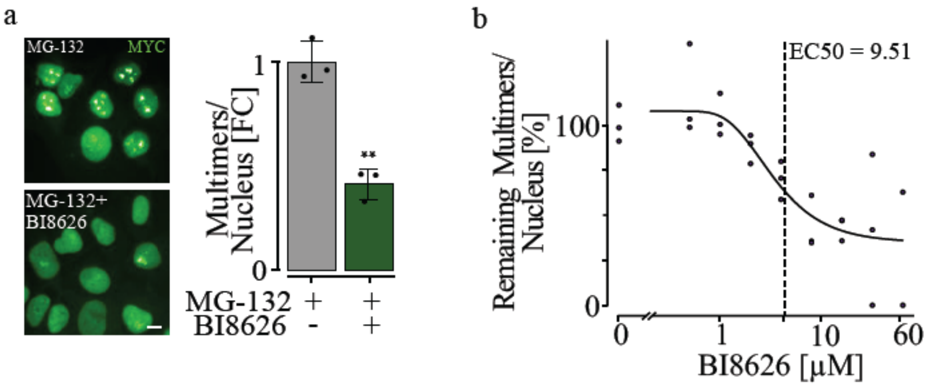

Figure 4.2.11: MYC multimerization depends on HUWE1 activity.

(a) Immunofluorescence pictures (left) and quantification (right) of multimer formation in $U2OS^{MYC\text{-}Tet\text{-}On}$ *cells in presence of oncogenic MYC levels upon treatment with MG-132 (20 µM, 4 hrs) and BI8626 (10 µM, 4 hrs) as indicated. Students t-test, two sided. (b) Dose response curve of MYC multimer formation in response to MG-132 (20 µM, 4 hrs) and BI8626 treatment at indicated concentrations in* $U2OS^{MYC\text{-}Tet\text{-}On}$ *cells in presence of oncogenic MYC levels using a four-parameter Weibull function (n=3). Parts of this figure appear in a similar form in Solvie et al. (in press).*

Considering these lines of evidence, I came to the conclusion that the multimerization process of MYC does not only depend on the IDRs in the MYC N-terminus, as indicated by several algorithms, but also displays an additional dependency on non-proteolytic ubiquitylation which is mediated by HUWE1.

4.2.4 Co-factors of MYC multimerization

With help of the above presented data, I established, that several factors that are involved in the ubiquitin-proteasome pathway and in transcription elongation influence the ability of MYC to multimerize.

To investigate whether additional factors which are directly involved in MYC biology play a role in multimerization I targeted the respective factors in an siRNA screen and assessed possible effects on MYC multimerization. For this, I transfected $U2OS^{MYC\text{-}Tet\text{-}On}$ cells in presence of oncogenic MYC levels and measured the effects on multimerization which was induced by previously discussed stimuli. The results were assessed by quantitative immunofluorescence with MYC multimers as readout. To normalize the data, I calculated Z-scores separately across each replicate and stimuli and visualized the results in form of a heat map (Figure 4.2.12). To explore similarities between different siRNAs, the appearance in the heat map was grouped based on their respective scores with the help of unsupervised clustering. The resulting dendrogram displays similarity of effects between siRNAs and was calculated across all treatment conditions.

An additional color-label was introduced on top of the heat map which categorizes the siRNAs into five functional groups.

Scores are represented by colors of the heat map and range from dark blue (fewest multimers) to yellow (most multimers) and are assigned based on the Z-score.

In total, seven clusters were formed.

Cluster one consists of two siRNAs which target SF3B1 and PSMA3 respectively and presents the smallest cluster of the heat map. At the same time, the clustering and dendrogram indicate a high similarity between the two proteins in context of MYC multimerization. Besides the combination with MG-132 treatment, depletion of the targets by siRNA led to a strong enhancement of multimerization, confirming effects exerted by inhibition of the proteasome (*PSMA3*) and splicing (*SF3B1*) genetically.

The second cluster consists primarily of siRNAs targeting proteins which are involved in transcription elongation, as well as binders of stalled replication forks; besides their role in elongation, SPT5, SPT6 and EXOSC10 are similarly involved in termination (Cortazar et al., 2019; Lemay et al., 2014; Narain et al., 2021). Like cluster one, depletion of the respective proteins resulted in equally enhanced foci formation across all conditions except for inhibition of the proteasome with deviating results. The targeting of *SUPT16H* genetically validated inhibition of the FACT-complex.

Cluster three is made up of factors that suppress multimerization in combination with MG-132 and PlaB treatment, while they are enhancing multimerization in presence of the remaining conditions.

Mainly DUBs are driving the composition of the fourth cluster, which groups siRNAs that moderately enhance multimerization across all conditions.

The fifth cluster consists of four MYC co-factors and their depletion strongly suppresses multimerization except for the combination with the inhibition of splicing.

Cluster six and seven group siRNAs with primarily repressing or no effect on MYC multimerization.

In summary, these results display a dependency of MYC multimerization on a group of MYC partner-proteins, that include SPT5, the PAF1 complex members CTR9 and CDC73, as well as the scaffold protein RUVBL1. To a lesser extent the depletion of proteins that are involved in the ubiquitin system shows a decreased multimerization ability in all conditions, which indicates a possibly redundant role of several E3-ligases and DUBs of MYC in the multimerization process. In contrast, proteins that are involved in binding of stalled replication forks and transcriptional control seemingly suppress multimerization as their absence enhances this ability of MYC. Finally, the results imply potentially different pathways in order to induce multimerization of MYC, with respect to the heterogeneous effects in several clusters.

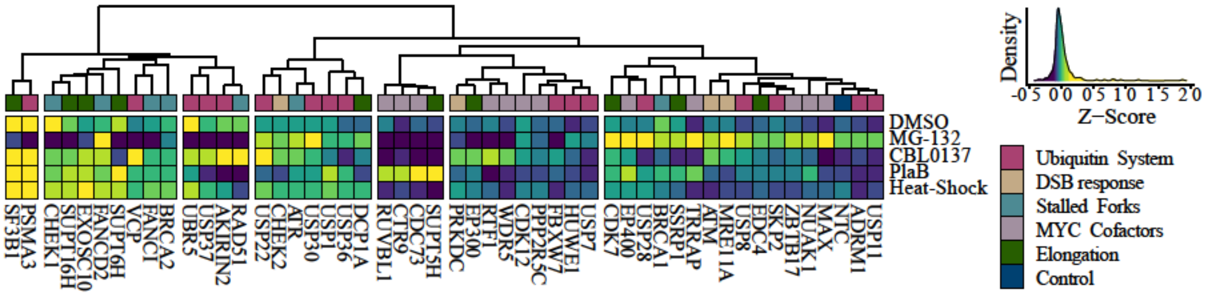

Figure 4.2.12: siRNA screening for MYC-multimerization co-factors.

(a) Heat map of row-wise normalized MYC multimerization in U2OS$^{MYC\text{-}Tet\text{-}On}$ cells in presence of oncogenic MYC levels. Cells were treated with MG-132 (20 µM, 4 hrs), CBL0137 (5 µM, 4 hrs), PlaB (1 µM, 4 hrs), or Heat-Shock (37°C, 30 min) as indicated. Dendrogram displays similarity between siRNAs based on their effect on multimerization across all treatments. Unsupervised clustering groups siRNAs into 7 groups based on effect similarity. Color-code in the first row represents functionality of targeted protein. Parts of this figure appear in a similar form in Solvie et al. (in press).

4.2.5 Cellular effects of MYC multimerization

MYC multimers form around stalled replication forks (see chapter 4.2.2). This evidence suggests a possible involvement of MYC multimers in stabilization and clearance of these. Therefore, I investigated effects of MYC multimerization on fork stability, genomic stability, and downstream cellular effects.

4.2.5.1 MYC multimerization protects the replication fork upon stress

To assess fork progression and stability, fiber assays were performed. In detail, two thymidine analogues (CldU, IdU) were sequentially incorporated into DNA which allows quantification of newly synthesized DNA fibers in the respective time frames. Depletion of the cellular dNTP pool by addition of hydroxyurea (HU) results in stalling of replication forks. Subsequent measurement of the length of the last synthesized fiber allows conclusions on fork stability (Figure 4.2.13a). Upon fork collapse, the adjacent DNA fiber will be resected by MRE11 and therefore appears as reduction in fiber length (Mijic et al., 2017).

Assessment of the fork stability 24 hours after MYC depletion displayed a significant regression of fiber length compared to the fiber length in control cells (Figure 4.2.13b). This phenotype is partially rescued by co-treatment of stalled replication forks with Mirin, a small molecule inhibitor of MRE11. This result confirms that the observed shortening of DNA fibers is mediated by the nucleolytic activity of MRE11 and thus fork degradation (Figure 4.2.13a,b).

Experiments that allow the replication forks to resume elongation by washing out HU, enable to study the number of restarting forks.

In line with the degradation of stalled replication forks that was observed in the previous setup of fiber assays (Figure 4.2.13b), MYC depletion resulted in a significant decrease in the number of forks that can restart and resume replication upon the removal of HU (Figure 4.2.13c).

To link the observed phenotypes more specifically to MYC multimerization, fiber assays were repeated in presence of HUWE1 inhibition (Figure 4.2.13d). The results reproduced those of MYC depletion (Figure 4.2.13e,f).

Nevertheless, the role of MYC and HUWE1 in reduction of co-transcriptional DNA damage, which I presented in the first part of this thesis (see chapter 4.1), can potentially result in similar phenotypes due to the fact that DSBs and stalled transcription forks are major sources of replication stress (see chapter 3.5). A MYC-mutant that allows multimerization but does not recruit the PAF1 complex to promoter regions could determine the multimerization specific impact of MYC on the replication fork stability.

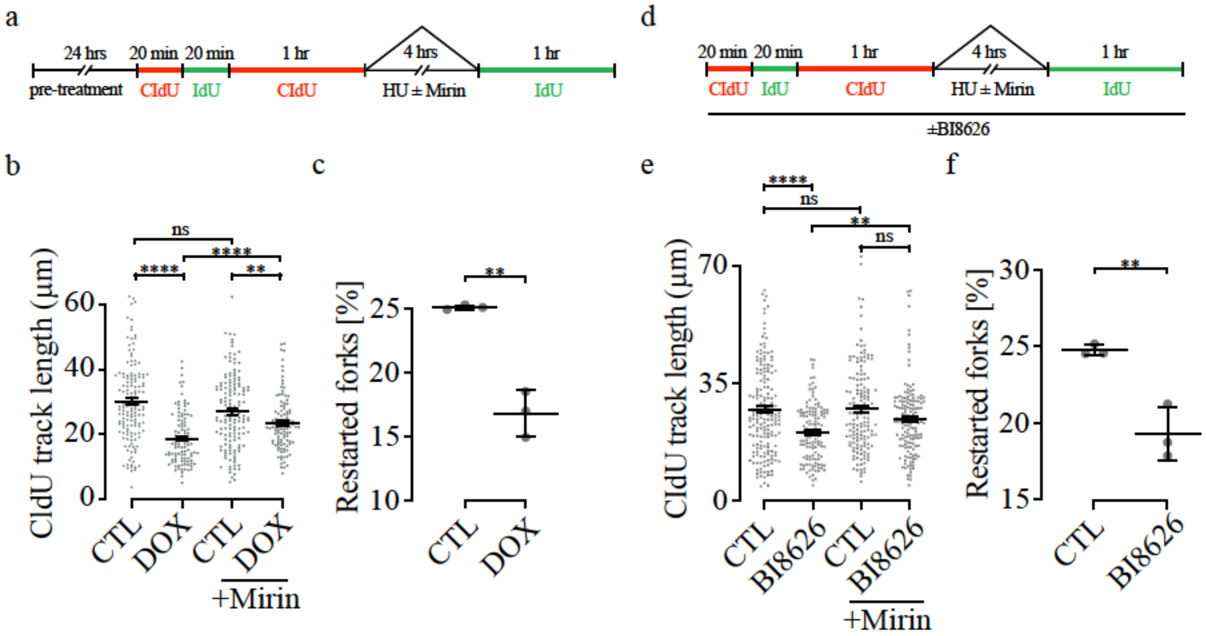

Figure 4.2.13: MYC multimerization protects the replication fork upon stress.

(a) Scheme of fiber assays in KPC cells expressing doxycycline-inducible shRNAs targeting MYC. Treatment with Dox (24 hrs), HU (2.5 mM, 4 hrs) and Mirin (50 µM, 4 hrs) as indicated. Timepoints represent assessment of unperturbed DNA replication (T1), fork degradation (T2) and fork restart (T3). (b) Fiber assay assessing fork degradation in presence or absence of MYC as described in (a). The mean second CldU track length (µm) and one of three biological replicates with similar results is shown. (c) Fiber assay assessing dependency of fork restart on MYC abundance as described in (a). (d) Scheme of fiber assays in KPC cells upon treatment with BI8626 (10 µM, 8.5 hrs), HU (2.5 mM, 4 hrs) and Mirin (50 µM, 4 hrs) as indicated. Measurements as described in (a). (e) Fiber assay assessing the impact of HUWE1 activity on fork degradation as described in (d). The mean second CldU track length (µm) and one of three biological replicates with similar results is shown. (f) Fiber assay assessing dependency of fork restart on HUWE1 activity as described in (d). Fiber assays performed by Celeste Giansanti and Jennifer Jansen. Parts of this figure appear in a similar form in Solvie et al. (in press).

4.2.5.2 Interference with MYC multimerization leads to replication catastrophe upon stress

Interference with the multimerization of MYC reduces the stability of stalled replication forks. In light of these results, I studied the phosphorylation state of RPA32 at S4/S8 which signals excessive replication fork stalling, replication catastrophe and DSBs (see chapter 3.5) in this condition.

Whole cell lysates were used for immunoblots with additional sonication steps to ensure complete solubilization of tightly chromatin bound proteins. In presence of replication stress that was induced by treatment with HU, HUWE1 inhibition strongly increased the amount of phosphorylated RPA32 (S4S8RPA) compared to the control condition (Figure 4.2.14a). This is further reflected by the shift of total RPA32 from the unphosphorylated lower towards the phosphorylated higher band in immunoblots. Contrary, I observed only a mild increase of RPA32 phosphorylation by inhibition of HUWE1 in presence of oncogenic MYC levels. Induction of MYC was controlled by immunoblotting for MYC.

I validated these results by CUT&RUN sequencing of S4S8RPA and observed a particular increase of chromatin abundance at active promoters upon HUWE1 inhibition. These sites were not responsive to induction of replication stress (HU) alone (Figure 4.2.14b). The metagene analysis contains peaks called in all active promoter regions. Notably, the S4S8RPA signal in cells that were exposed to HU and BI8626 simultaneously is highly specific for the promoter region and the signal regresses outside of the active promoter region to background. The treatment with HU alone and the control show a more stochastic presence of S4S8RPA outside of the promoter regions.

S4S8RPA acts as a marker for replication catastrophe (Toledo et al., 2017) and in order to study the resulting DNA breakage, I sequenced DSBs using BLISS (Figure 4.2.14c). The detected DSBs were assigned by proximity to locations spanning genic, intergenic and promoter regions. In line with results for S4S8RPA immunoblots and CUT&RUN sequencing, HUWE1 inhibition increased the amount of DSBs in presence of replication stress. In contrast, MYC induction limited the amount of DSBs, in a HUWE1 dependent manner (Figure 4.2.14c).

To link the observed results more closely to MYC multimerization, I performed BLISS experiments in a cell system that allows depletion of endogenous MYC (MYC-AID). I rescued the depletion of MYC by inducible expression of different MYC constructs. In presence of replication stress, the expression of wildtype MYC rescued accumulation of DSBs in comparison to K-less MYC which displayed an amount of DSBs that resided at levels of cells without MYC (MYC OFF) (Figure 4.2.14d). In contrast, $\text{MYC}^{\text{K-R148KR389K}}$ (see Figure 4.2.9) showed the ability to strongly limit the accumulation of DSBs (Figure 4.2.14e).

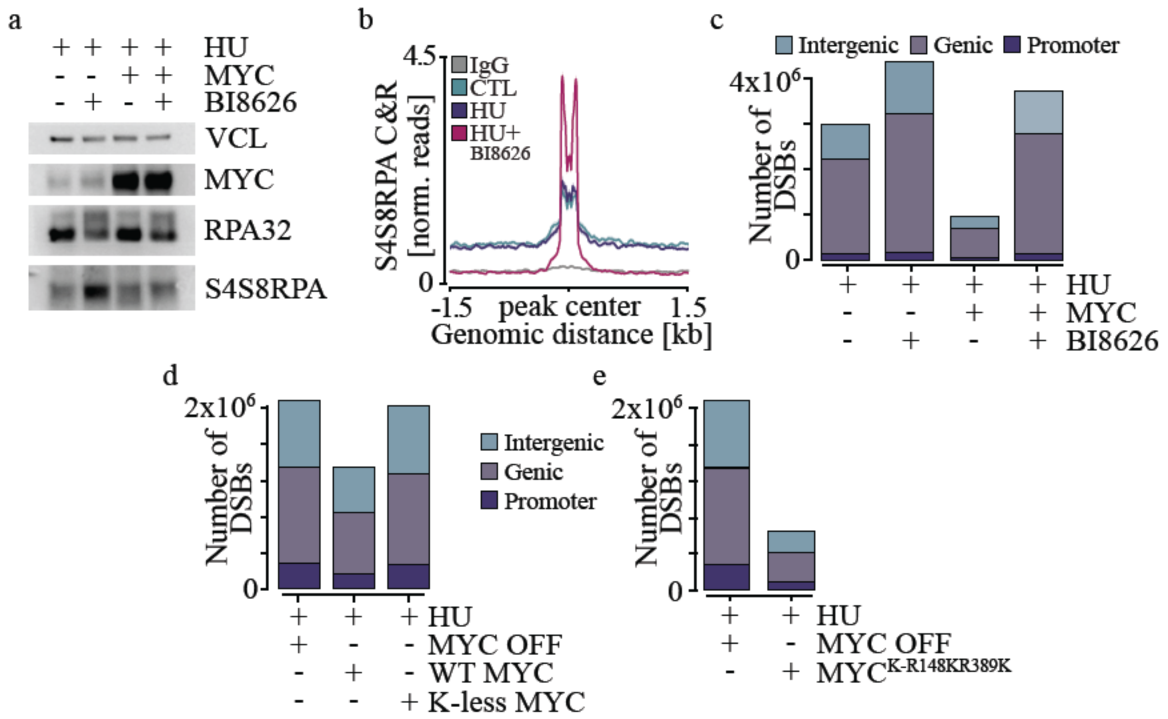

Figure 4.2.14: Interference with MYC Multimerization leads to replication catastrophe upon stress

(a) Immunoblot assessing phosphorylation state or S4S8RPA of U2OS$^{MYC\text{-}Tet\text{-}On}$ cells upon treatment with Dox (24 hrs), HU (3.5 µM, 8 hrs) and BI8626 (10 µM, 8.5 hrs). Interference with MYC Multimerization leads to apoptosis upon stress. (b) Spike normalized reads from S4S8RPA CUT&RUN experiment shown centered around 4,252 common peaks called around promoters in U2OS$^{MYC\text{-}Tet\text{-}On}$ cells treated with Dox (24 hrs), HU (3.5 µM, 8 hrs) and BI8626 (10 µM, 8.5 hrs). Analysis performed by Apoorva Baluapuri. (c) Bar plot quantifying double strand breaks in U2OS$^{MYC\text{-}Tet\text{-}On}$ cells as determined by BLISS across triplicates. Treated with Dox (24 hrs), HU (3.5 mM, 8 hrs) and BI8626 (10 µM, 8.5 hrs) as indicated (n=3). (d) Bar plot quantifying double strand breaks (BLISS) in U2OS$^{MYC\text{-}AID}$ cells. Expression of WT, K-less or no MYC is induced by Dox 18 hrs before depletion of endogenous MYC by indole acetic acid (IAA, 8 hrs) treatment. Treatment with HU (3.5 mM, 8 hrs) as indicated. Representative replicate shown (n=2). (e) Bar plot quantifying double strand breaks (BLISS) in U2OS$^{MYC\text{-}AID}$ cells. Expression of MYC$^{K\text{-}R148KR389K}$ or no MYC is induced by Dox 18 hrs before depletion of endogenous MYC by indole acetic acid (IAA, 8 hrs) treatment. Treatment with HU (3.5 mM, 8 hrs) as indicated. Representative replicate shown (n=2). Parts of this figure appear in a similar form in Solvie et al. (in press).

Taken together, I observed that the ability of MYC to multimerize has the ability to limit replication catastrophe and the accumulation of DSBs. This phenotype is not solely observed at promoters but additionally at intergenic sites, which is in line with a major localization of MYC multimers outside of promoter regions.

4.2.5.3 Interference with MYC multimerization leads to apoptosis upon stress

The downstream cellular effect of replication catastrophe and excessive DNA damage is apoptosis. Hence, I determined the number of cells that displayed an apoptotic phenotype in response to replication stress by flowcytometry and explored the effect that the ability to form MYC multimers has. A staining for Annexin V and Propidium Iodide allows quantification of cells in late apoptosis. Approximately 9% of all untreated $U2OS^{MYC\text{-}Tet\text{-}On}$ cells upon MYC induction fulfilled the criteria for late apoptosis (Figure 4.2.15a). Treatment with HU or BI8626 alone increased the amount of late apoptosis to around 15-18%. In contrast, I observed around 43% of all cells that showed a late apoptotic phenotype with the combination of replication stress and HUWE1 inhibition. The results of biological triplicates are summarized in form of a bar graph (Figure 4.2.15b).

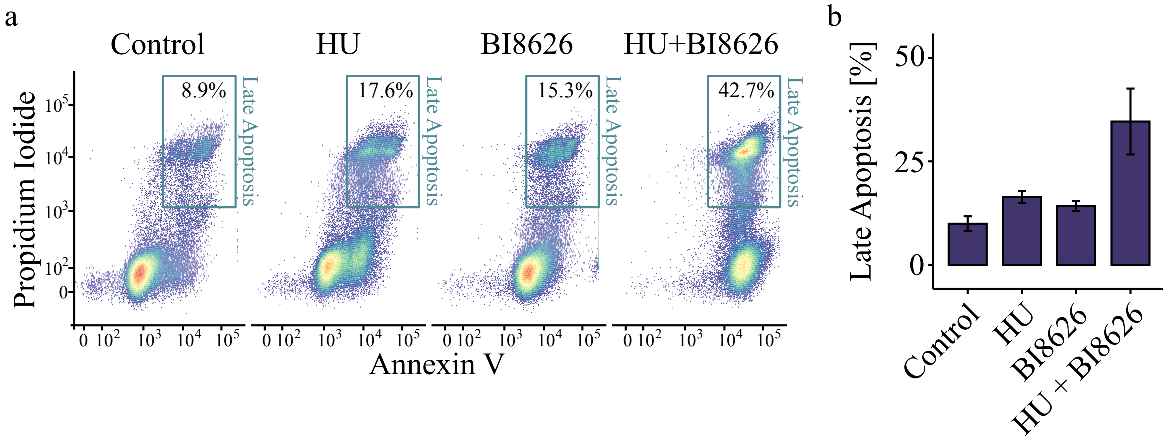

Figure 4.2.15: Interference with MYC Multimerization leads to apoptosis upon stress.
(a) Scatter plot of Annexin V-Propidium Iodide FACS data of $U2OS^{MYC\text{-}Tet\text{-}On}$ *cells treated with Dox (24 hrs), and BI8626 (10 µM, 24 hrs) and HU (2 mM, 23.5 hrs). Gating for late apoptosis defined by high values for propidium iodide and Annexin V measurement and percentage calculated as proportion of all cells in the respective condition. Representative experiment of biological triplicates shown. (b) Bar plot quantifying the percentage of cells in late apoptosis of three biological replicates per condition.*

4.2.6 Summary on the findings of MYC multimerization

The data presented in context of the second project in this thesis describe the potential of MYC proteins to undergo phase transition in response to perturbation of transcription and replication. The MYC multimers that are induced by these stresses are found in proximity of stalled replication forks on chromatin and recruit factors of the DNA-damage response and transcription termination machinery. Further, I identified ubiquitylation as an essential switch to prompt phase transition and cells that were devoid of the ability to form multimers display high rates apoptosis in response to replication stress (Figure 4.2.16).

Genomic instability, an original hallmark of cancer, is acquired by mutations in DNA repair and cell cycle checkpoint genes. Consequently, tumor cells are particularly susceptible to interference with DNA replication. Hence, I propose a model where phase transition of MYC proteins acts as an intrinsic mechanism of MYC-driven tumors to ensure unperturbed genomic replication and thereby proliferation in these non-physiological conditions.

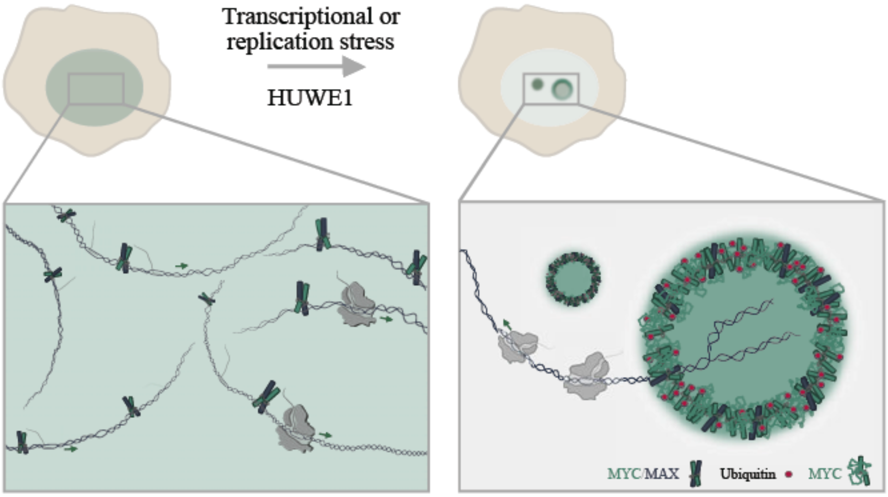

Figure 4.2.16: Model summarizing the findings on MYC multimerization.

Model summarizing the findings on MYC multimerization. Model was designed by Leonie Uhl. Parts of this figure appear in a similar form in Solvie et al. (in press).

5 Discussion

The widely accepted transforming principle of MYC is the regulation of gene expression upon heterodimerization with MAX and MIZ1 (Grandori et al., 2000; Lin et al., 2012; Nie et al., 2012; Sabo et al.; Walz et al., 2014). However, the question remains whether the apparent differences between MYC binding to DNA and the effects on mRNA production can be accounted for by the gene-specific, the affinity or the global amplifier model (see chapter 3.4). The fact that this question has not yet been satisfyingly answered promotes the idea that the oncogenic functions of MYC are gene expression independent. This hypothesis is supported by data from several papers that have been published in recent years (Endres et al., 2021; Herold et al., 2019; Papadopoulos et al., 2021; Roeschert et al., 2021) as well as by data presented in this thesis.

5.1 Guardian of oncogenic transcription

Tumor cells sustain high and deregulated levels of transcription and replication due to defects in cell-cycle checkpoint signaling and dysregulation of transcriptional programs (Bradner et al., 2017; Hanahan and Weinberg, 2011). The data analyzed in this thesis strongly indicate functions of MYC that enable a tumor cell to tolerate the supraphysiological stress levels by limiting co-transcriptional and co-replicational damage.

First, oncogenic MYC levels increase H2B ubiquitylation at lysine 120 which disrupts chromatin compaction and thereby allows efficient recruitment of the DSB repair machinery (Moyal et al., 2011). This is directly reflected by the MYC-dependent prevention of transcriptionally induced DSBs, which can be enhanced by topoisomerase II inhibition (Kouzine et al., 2013). Mechanistically, H2B is ubiquitylated at lysine 120 by RNF20-RNF40 in cooperation with the PAF1c subunit RTF1 (Van Oss et al., 2016). Although the recruitment of the PAF1c by MYC to promoters has been published (Jaenicke et al., 2016), data from ChIP-Rx-sequencing and PLA experiments demonstrate a subsequent handover of the PAF1c from MYC to RNAPII in a HUWE1-dependent manner. Accordingly, perturbation of HUWE1 function reduces the amount of MYC-driven H2B ubiquitylation at lysine 120. Taking into account that MYC is capable of preventing genomic instability in response to transcription stress, the identified pathway proposes MYC as mediator of co-transcriptional DNA damage repair.

Second, the data presented here reveal the ability of MYC to multimerize and these multimers were shown to form adjacent to stalled replication forks. In unperturbed cells, replication is initiated at thousands of sites across the genome – a process that is well timed and coordinated with transcription.

However, tumor cells commonly display a shortening of G1 phase and the premature firing of origins of replication which provokes transcription-replication conflicts and replication stress (Macheret and Halazonetis, 2018). The MYC paralog MYCN has been shown to coordinate transcription and replication by termination of transcription via the RNA exosome (Papadopoulos et al., 2021). Similarly, multimers contain several exosome subunits, particularly in the shell, as well as SPT5 which has been implicated to have roles in transcriptional termination (Cortazar et al., 2019). These observations suggest a model according to which MYC multimers can create a zone of termination thereby shielding the enclosed replication fork from RNA polymerase.

The interior of MYC multimers contains BRCA1, FANCD2, and phosphorylated ATR, representing an accumulation of binders and stabilizers of stalled replication forks (Cimprich and Cortez, 2008; Lachaud et al., 2016; Thakar and Moldovan, 2021). In line with this observation, MYC multimers are increasing the stability of replication forks that are exposed to replication stress. Their function is to prevent a fork collapse and thus enhancing fork restart upon deprivation of stress. Unresolved stalling and collapse of replication forks directly translates to the formation of DSBs, excessive genomic instability and ultimately cell death (Toledo et al., 2017). In accordance with that, the absence of MYC multimers sensitizes cells to replication stress (see chapter 4.2.5).

The observations described above may shed new light on the oncogenic properties of MYC. In the face of oncogenic and hence deregulated transcription and replication, MYC acts as a stress resilience factor that compensates oncogenic stress levels by surveilling transcription and replication to preserve genomic integrity. The ability of MYC to exert these versatile functions relies on a specific switch between interaction partners. A large body of evidence indicates that a significant extend of the protein-protein contacts that are subjected to these rapid changes are governed by transient and multivalent interactions.

5.2 Phase separation of MYC

Diverse transcription factors participate in phase-separated condensates that stimulate transcription and from by multivalent interactions of their highly disordered activation domains (Boija et al., 2018). 79% of all MYC residues are predicted to reside in disordered regions and form two major IDRs that are located towards the N-terminal region of MYC (Figure 3.3.3). The very N-terminal IDR of MYC is a transcription activation domain (Kato et al., 1990) and a recent publication on phase separation of transcription factors described MYC to undergo phase transition *in vitro* (Boija et al., 2018). The data presented in this thesis recapitulate this finding and further demonstrate the ability of MYC to phase separate *in vivo*.

In unperturbed cells, hubs of MYC can be detected by super resolution microscopy. Up to 14% of all MYC molecules in a nucleus reside in hubs of more than 100 MYC molecules (Figure 4.2.1). A screening approach for biological and biophysical stimuli which can enhance phase separation of MYC to a level that is detectable by confocal microscopy, determined interference with transcription elongation in form of inhibition of splicing or of the FACT-complex as such. Similarly, interference with the ubiquitin-proteasome-system as well as exposure to heat-shock, which has recently been published to result in premature termination (Cugusi et al., 2022), enhanced phase transition of MYC proteins, which caused by MYC multimerization as reported in chapter 4.2.1.4. The biophysical properties of these respectively enhanced MYC multimers, which are apparent by confocal microscopy (Figure 4.2.2), can be studied in several ways. Contrary, the small size and laborious measurement of multimeric structured hubs in unperturbed cells render these difficult to study and require advanced strategies for future investigations. Therefore, the question remains whether the discussed stimuli solely increase the size of the MYC hubs that are observed in unperturbed cells and accordingly, whether they fulfil the same biological function. Hubs in unperturbed cells may otherwise represent for instance transcriptional condensates as previously hypothesized (Boija et al., 2018).

There are several features which distinguish MYC multimers from biologically inactive aggregates. First, previous publications discuss accumulation of MYC in nucleoli upon proteasomal inhibition (Arabi et al., 2003; Welcker et al., 2004a). In contrast, the data in this thesis demonstrate that MYC multimers are unaffected by nucleolar disruption (see chapter 4.2.2.3). Additionally, the differences in size distribution of multimers and nucleoli exclude a solely nucleolar dependency. Notably, the data that was generate by a triple-staining of MYC, Fibrillarin and BRCA1 indicates that multimer formation around nucleoli is likely to be induced by DNA damage occurring on the inside of the nucleoli (see chapter 4.2.2.3).

Second, inhibition of the proteasome can lead to assemblies of misfolded proteins that are otherwise targeted by the cellular degradation machinery and eventually form stable, irreversible aggregates (Sweeney et al., 2017). However, FRAP and reversibility assays clearly distinguish MYC multimers from these biologically inactive aggregates (see chapter 4.2.1.3).

Third, MYC multimers can form hollow structures *in vitro* (Solvie et al., *in press*) and *in cellulo*. In the latter case, functionally distinct groups of proteins are concentrated either in the interior or in the multimer shell. Heterotypic electrostatic interactions can induce formation of phase separated, spherical structures *in vivo (Alshareedah et al., 2020).* However, phase separation *in vitro* is solely driven by homotypic interactions and thus the hollow structures *in vitro* remain to be further investigated; biophysical properties of the MYC protein could result in a specific order of MYC-MYC interactions similar to lipids for instance.

Posttranslational modifications (PTMs) change the biophysical properties of the target region and are likely to change the stability of transient, local structures, modulate compactness, or lead to order-disorder transitions (Bah and Forman-Kay, 2016). In line with this, my data show that non-proteolytic ubiquitylation plays an essential role in driving multimerization and thus phase separation of MYC. Two lysine residues are particularly important in this process, K148 and K389.

K389 resides in the loop region of the helix-loop-helix domain of MYC. Due to the function of this domain in DNA-binding, ubiquitylation is likely to result in clashes with the DNA helix.

K148 is located in proximity to MBII and ubiquitylation may disrupt binders of this conserved region such as the scaffolding protein TRRAP (McMahon et al., 1998). Further, K148 is a target site of the HUWE1 ubiquitin ligase (Heidelberger et al., 2018). HUWE1 drives the handover of the PAF1c from MYC onto RNAPII and reduces the interaction of MYC with the PAF1c as apparent from sequencing and PLA data shown in this thesis. PAF1c has been shown to enhance chromatin affinity of MYC (Endres et al., 2021) similarly to what was previously shown for WDR5 (Thomas et al., 2015). This is in line with the fact that chromatin distribution of MYC does not only depend on its intrinsic DNA binding specificity (Guo et al., 2014). Taken together, HUWE1-mediated ubiquitylation decreases chromatin affinity of MYC similar to the predicted effects of ubiquitylation at K389.

Considering the ability of recombinant MYC protein to condensate *in vitro*, I suggest a model in which MYC's intrinsic propensity of MYC to multimerize is antagonized by interactions with binding partners and DNA. Conversely, ubiquitylation of MYC disrupts these interactions and thereby drives MYC multimerization and phase separation in this model.

HUWE1 has been identified as major driver of MYC multimerization. Nonetheless, more than 18 E3-ligases and at least 6 DUBs are described to control MYC ubiquitylation with contrasting results ranging from modulation of protein stability to activity (Sun et al., 2021). Therefore, further investigations may identify additional drivers and inhibitors of the phase transition process with the intriguing possibility that specific stimuli drive multimerization via distinct E3-ligases.

5.3 Segregation from stereotypic interactors by non-proteolytic ubiquitylation of MYC

In the previous chapter multivalent interactions and ubiquitylation have been discussed as mechanism to disrupt protein-protein interactions in context of phase-transition of MYC. Setting these observations into a different context might even serve as an explanation for yet another conundrum of MYC biology.

Depending on the experimental method and the cut-off score, about 80 proteins interact with MYC and MYCN (Baluapuri et al., 2020). The interactomes can be partitioned into categories comprising primarily chromatin remodeling, transcriptional regulation, RNA processing, transcriptional termination, DNA damage and the ubiquitin system (Baluapuri et al., 2020; Kalkat et al., 2018). Considering this, several of the interactors display opposing functions and a simultaneous interaction is unlikely. However, the mechanism controlling the selectivity and timing of the interactions remains unclear.

Several interactions with MYC are accounted for by conserved interaction motives like the phospho-dependent FBXW7 degron, the GSK3 motive, the Proline-Directed Kinase motive (MAPK), and also by motives that are predicted to mediate interaction with BRCA1 or SUMO proteins (ELM database). However, the majority of interactions lack any structural specificity. Exemplary, the investigations that aimed to identify specific regions of MYC which mediate the interaction with SPT5 or PAF1c resulted in only mild quantitative differences despite major deletions in the MYC protein but never in a complete loss of interaction (Baluapuri et al., 2019; Endres et al., 2021). In light of these results, the interactions between SPT5 or PAF1c and MYC are likely mediated by unspecific interactions through the IDRs in the MYC N-terminus.

IDRs provide the basis for primarily multivalent, transient, and promiscuous interactions with different partner proteins on different occasions (Banani et al., 2017; Wright and Dyson, 2015) which elucidates on the lack of specific binding motives and regions between MYC and the multiplicity of interaction partners.

As previously discussed, ubiquitylation can alter the biophysical properties of the modified regions and thus is likely to alter interaction opportunities which exemplary has been shown for OTULIN and LUBAC (Zhao et al., 2020). Accordingly, ubiquitylation offers a mechanism to control timing and specificity of the MYC interactome and thereby allowing a rapid switch from promoter proximal interactions with activating transcription factors like WDR5 or TRRAP towards factors involved in transcription termination and DDR, e.g. the RNA exosome and BRCA1.

As such, the ubiquitin-driven segregation model does not only explain the switch between heterodimeric and multimeric MYC but also refines the PAF1c hand-over from MYC onto RNAPII: HUWE1-mediated ubiquitylation will disrupt the interaction of MYC with PAF1c and thereby likely increase the affinity of PAF1c to RNAPII.

Proteolytic ubiquitylation of MYC, primarily mediated by K48-linked chains, offers a straight-forward explanation on the subsequent effects. In contrast, non-proteolytic ubiquitylation and respective repercussions demand more thorough inquiry. The data reported in this thesis presents an unexplored perspective on the versatile mechanisms of MYC by considering non-proteolytic ubiquitylation as a separator of multivalent interactions with the vast and diverse interactome which determines MYC’s functionality. Consequently, studies that explore ubiquitylation sites which govern interactions that favor oncogenesis will empower to design molecules that mimic ubiquitylation at respective sites thereby specifically targeting the oncogenic function of MYC.

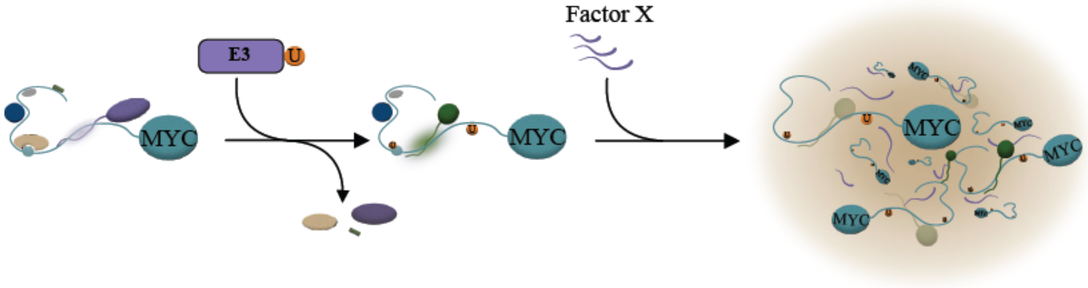

Figure 5.3.1: Segregation from stereotypic interactors by non-proteolytic ubiquitylation of MYC.
MYC in its soluble form is bound by several interactors, either by contacts that are mediated through classical motives or multivalency. Upon ubiquitylation of MYC, for instance by the E3-ligase HUWE1, certain interactors loose affinity in favor of different interactors, while others are unaffected. Subsequently, the presence of "factor X" will result in entropically favorable homotypic interactions ultimately resulting in phase transition. "factor X" may represent abundance of charges in the solvent, e.g., in form of RNAs, an increase of local concentration of MYC, or interaction with a specific protein/molecule.

5.4 Implications for oncogenesis and therapy

MYCN can alleviate transcription and replication stress by interaction with AURKA, BRCA1 and the RNA exosome (Herold et al., 2019; Papadopoulos et al., 2021; Roeschert et al., 2021). In this thesis, I present data that support two new mechanisms by which MYC facilitates stress resilience: MYC couples the processes of transcription and DNA damage repair and moreover, MYC shields stalled replication forks by the formation of multimeric structures and thereby limits the formation of DSBs.

Tumorigeneses is driven by alterations in the genome which commonly result in defects in cell-cycle checkpoint signaling and dysregulation of transcriptional programs (Bradner et al., 2017; Hanahan and Weinberg, 2011). On the one hand, these phenotypes enable tumors to proliferate rapidly, but on the other hand they disturb the coordination between transcription and replication. Consequently, this results in high levels of replication and transcriptional stress, a typical features of oncogenesis (Garcia-Muse and Aguilera, 2016; Macheret and Halazonetis, 2018) that is accompanied by an increased dependency of tumor cells on factors that help to compensate these supraphysiological stress levels.

In view of this, the mechanisms involving MYC as a stress resilience factor are an important contribution to MYC's oncogenic function and thus of considerable therapeutic value.

The two mechanisms that are reported in this thesis and have been shown to confer MYC-mediated stress resilience, are based on rapid changes in protein-protein interactions between MYC and its interactors. Several lines of evidence suggest that these interactions are mediated by multivalency and controlled by non-proteolytic ubiquitylation.

Based on these observations, I propose two approaches to target the stress resilience function of MYC specifically.

First, interfering with the ubiquitylation of MYC at lysine residues K148 and K389 can prevent the changes in protein-protein interaction that are required to couple transcription with DNA damage response and for the multimerization of MYC. Therefore, compounds that inhibit the respective E3-ligase are desirable. HUWE1 was identified as the E3-ligase with the strongest effects on the mechanisms reported in this thesis. The validation of these effect of HUWE1 in *in vivo* models is thus an apparent approach. However, the available HUWE1 inhibitor is not suitable for *in vivo* applications which necessitates the development of a more potent HUWE1 inhibitor.

The changes in protein-protein interaction of MYC with its interactors are stress-dependent, non-proteolytic and reversible (see chapter 4.2.1) which implies that the specific ubiquitylation of MYC is antagonized by one or more DUBs. The identification of DUBs that are involved in this process will give rise to new therapeutic targets to interfere with the dynamic changes in the MYC interactome which is likely to impair the oncogenic mechanisms of MYC that are discussed in this thesis.

Second, the ability of MYC to multimerize relies on dynamic, multivalent interactions, and evidence suggest that for example also MYC and PAF1c interact via IDRs. Therefore, a further promising approach to target the oncogenic mechanisms of MYC that I addressed in this thesis is the interference with MYC’s IDRs. IDRs and thus also MYC have been considered undruggable (see chapter 3.3). However, recent advances in chemistry make it possible to design specific binders of IDRs (Boija et al., 2021) which opens new opportunities to target these structures and consequently MYC.

6 Materials

Substantial parts of this chapter have been published in Endres et al. (2021) and Solvie et al. (*in press*).

6.1 Cells

HEK293TN, NIH3T3 and U2OS cells were grown in DMEM (Sigma-Aldrich and Thermo Fisher Scientific). Media were supplemented with 10% fetal calf serum (FCS) (Biochrom and Sigma-Aldrich) and penicillin/streptomycin (Sigma-Aldrich). All cells were routinely tested for mycoplasma contamination and STR genotyped before use. Cells were treated at the following concentrations, if not stated otherwise: doxycycline: 1 µg/ml; MG-132: 20 µM; Pladienolide B (PlaB): 1 µM; CBL0137: 5 µM; BI8626: 10 µM; HU: 3.5 mM; aphidicolin: 400 nM.

6.2 Antibodies

Antigen	**Manufacturer**	**Identifier**
Mono- & polyubiquitinylated conjugates (FK2)	Enzo Life Sciences	BML-PW8810
K6 Affimer® reagent containing a GFP/His tag	Merck	MABS1918
(B-10)	Santa Cruz Biotechnology	sc-136985
GFP	Santa Cruz Biotechnology	sc-9996
RNA Polymerase II RPB1 Antibody (pS2)	Biolegend/Biozol	BLD-920204
RNA Polymerase II RPB1 Antibody (pS5)	Biolegend/Biozol	BLD-904001
BRCA1	Santa Cruz Biotechnology	sc-6954
TopBP1 Thermo Fischer Scientific	Thermo Fischer Scientific	PA5-65178
SMC3 Bethyl Laboratories	Bethyl Laboratories	A300-060A
pATM (Ser1981)	Abcam	ab81292
MRE11	Abcam	ab208020
Topo II alpha	Santa Cruz Biotechnology	sc-13058
gamma H2AX	Abcam	ab2893
ATR (phospho T1989)	Abcam	ab227851
TOP1	Bethyl Laboratories	A302-589A
EXOSC10	Abcam	ab50558
Fibrillarin	Abcam	ab5821
FANCD2 [EPR2302]	Abcam	ab221932
RAD9	Thermo Fischer Scientific	PA5-21275
Phospho RPA32 (S33)	Bethyl Laboratories	A300-246A
Phospho RPA32 (S4/S8)	Bethyl Laboratories	A300-245A
SPT5	Santa Cruz Biotechnology	sc-133217X
Ubiquitin Antibody, Lys48-Specific, clone Apu2	Merck	05-1307
Ub-K63 (JM09-67)	Thermo Fischer Scientific	MA5-32573

Antigen	Manufacturer	Identifier
MAX	Proteintech	10426-1-AP
SPT6	Novus Biologicals	NB100-2582
Pol II (A-10)	Santa Cruz Biotechnology	sc-17798
Pol II (F-12)	Santa Cruz Biotechnology	sc-55492
MYC (clone Y69)	Abcam	ab32072
MYC (C33)	Santa Cruz Biotechnology	sc-42
phospho-Ser2-RNAPII	Abcam	ab5095
RNAPII	MBL International	MABI0601
Histone H2B	Abcam	ab1790
H2B (Lys120) (D11) XP®	Cell Signaling Technology	5546
HUWE1/Mule antibody	Abcam	ab70161
PAF1	Abcam	ab20662
VCL	Sigma-Aldrich	V9131
CHK1(FL-476)	Santa Cruz Biotechnology	sc-7898
phospho-Chk1 (Ser345) (133D3)	Cell Signaling Technology	cs-2348
SUMO2/3	Thermo Fischer Scientific	PA5-11373
HA tag	Abcam	ab9110
KAP1	Bethyl Laboratories	A300-274A
phospho-MYC (S62)	Abcam	ab51156
phospho-MYC (S373)	Abcam	ab30643
MYC (C-19)	Santa Cruz Biotechnology	sc-788
MYC (N-262)	Santa Cruz Biotechnology	sc-764
phospho-MYC (S62)	Abcam	ab78318
MYCN (NCM II 100)	Santa Cruz Biotechnology	sc-56729
Anti-N-Myc Mouse mAb (NCM II 100, OP13)	Merck	OP13
Donkey polyclonal anti-goat IgG-HRP secondary	Santa Cruz Biotechnology	sc-2020
ECL-Anti-rabbit IgG Horseradish Peroxidase	GE Healthcare / Fisher	GENA934
ECL-Anti-mouse IgG Horseradish Peroxidase	GE Healthcare / Fisher	GENA931
IRDye 800CW Donkey anti-Rabbit IgG (H + L)	LI-COR Biosciences	926-32213
IRDye 680RD Donkey anti-Mouse IgG (H + L)	LI-COR Biosciences	926-68072
Goat anti-Mouse IgG (H+L) Highly Cross-Adsorbed Secondary Antibody, Alexa Fluor 488	Thermo Fisher Scientific	A-11029
Goat anti-Rabbit IgG (H+L) Highly Cross-Adsorbed Secondary Antibody, Alexa Fluor 488	Thermo Fisher Scientific	A-11034
Goat anti-Mouse IgG (H+L) Highly Cross-Adsorbed Secondary Antibody, Alexa Fluor 568	Thermo Fisher Scientific	A-11031
Goat anti-Rabbit IgG (H+L) Highly Cross-Adsorbed Secondary Antibody, Alexa Fluor 568	Thermo Fisher Scientific	A-11036

Antigen	Manufacturer	Identifier
Goat anti-Mouse IgG (H+L) Highly Cross-Adsorbed Secondary Antibody, Alexa Fluor 647	Thermo Fisher Scientific	A-21235
Goat anti-Rabbit IgG (H+L) Highly Cross-Adsorbed Secondary Antibody, Alexa Fluor 647	Thermo Fisher Scientific	A-21245

6.3 Buffers and solutions

Buffer/Solution	Components
BCA Solution A	1% BCA-Na_2 2% Na_2CO_3
BCA Solution B	4% $CuSO_4$ 0.16% Na-tartrate 0.4% NaOH 0.95% $NaHCO_3$
Blocking Buffer	20 vol% Intercept Blocking Buffer 80 vol% TBS
Bradford Solution	8.5 vol% orthophosphoric acid 4.75 vol% ethanol 0.01% Coomassie Brilliant Blue G-250
ChIP Blocking Buffer	5 mg/ml BSA in PBS
ChIP Elution Buffer	50 mM Tris pH 8.0 1 mM EDTA 1 vol% SDS 50 mM $NaHCO_3$
ChIP Lysis Buffer I	20 mM Tris pH 7.5 150 mM NaCl 1% NP-40 1% Na-deoxycholate 0.1 vol% SDS 1 mM EDTA
ChIP Lysis Buffer II (RIPA)	50 mM HEPES pH 7.9 140 mM NaCl 1 mM EDTA 1 vol% Triton X-100 0.1% Na-deoxycholate 0.1 vol% SDS 1 mM PMSF freshly added protease and phosphatase inhibitors freshly added

Buffer/Solution	Components
ChIP Wash Buffer I	20 mM Tris HCl pH 8,1 150 mM NaCl 2 mM EDTA 0.1 vol% SDS 1 vol% Triton-X-100
ChIP Wash Buffer II	20 mM Tris HCl pH 8,1 500 mM NaCl 2 mM EDTA 0.1 vol% SDS 1 vol% Triton-X-100
ChIP Wash Buffer III	10 mM Tris HCl pH 8,1 250 mM LiCl 1 mM EDTA 1% NP40 1% Deoxycholic acid sodium salt
ChIP Elution Buffer	1 vol% SDS 100 mM $NaHCO_3$
DNA Loading Buffer (6x)	40% Sucrose 0.2% Orange G 10 mM EDTA
Miniprep Resuspension Buffer	50 mM Tris HCL pH 8.0 10 mM EDTA pH 8.0 10 µg/ml RNAse A
Miniprep Lysis Buffer	200 mM NaOH 1 vol% SDS
Miniprep Precipitation Buffer	3.1 M KOAc pH 5.5
MOPS Running Buffer	50 mM MOPS 50 mM Tris 1 mM EDTA 0.1 vol% SDS 5 mM sodium bisulfite
NuPAGE Transfer Buffer	25 mM Bis-Tris 25 mM Bicine 1.025 mM EDTA 0.006 mM Chlorobutanol 20 vol% Methanol

Buffer/Solution	**Components**
PBS	137 mM NaCl 2.7 mM KCl 10.1 mM Na2HPO4 1.76 mM KH2PO4
Polyethyleneimine (PEI)	450 µl PEI (10%, MW 25,000 g/mol, Sigma) 150 µl HCl (2 N) 49.5 ml ddH2O
Proteinase K	10 mg/ml in ddH2O
Sample Buffer (Laemmli, 1)	62.5 mM Tris pH 6.8 666.7 mM ß-Mercaptoethanol 10 vol% Glycerin 2 vol% SDS 0.01 vol% Bromophenol blue
TE	10 mM Tris, pH 7.4 1 mM EDTA, pH 8.0
TAE	40 mM Tris pH 8.0 0.114 vol% acetic acid 1 mM EDTA
TBS	25 mM Tris base 140 mM NaCl pH 7.4 with HCl
TBS-T	1 x TBS 0.2% Tween-20
IF/PLA Fixation Buffer	4 vol% PFA in PBS
IF/PLA Permeabilization Buffer	0.1 vol% Triton-X in PBS
IF/PLA Blocking Buffer	1% BSA 0.1 vol% Tween-20 in PBS
EdU Cycloaddition Buffer	100 mM Tris HCL pH 8.5 4 mM $CuSO_4$ 10 µM AF647-Picolyl-Azide 10 mM L-Ascorbic Acid
APEX2 quenching Buffer	10 mM sodium azide 10 mM L-sodium ascorbate 5 mM Trolox in PBS

6.4 Chemicals

Reagent	Manufacturer	Identifier
Doxycycline hyclate	Sigma-Aldrich	Cat#D9891-10G
Indole-3-acetic acid sodium salt	Sigma-Aldrich	Cat# I5148-2G
Hoechst 33342	Sigma-Aldrich	Cat#B2261-25MG
5-Ethynyl-2'-deoxyuridine (5-EdU)	Jena Bioscience	Cat#CLK-N001-100
AF647-Picolyl-Azide	Jena Bioscience	Cat#CLK-1300-1
Lipofectamine RNAiMAX Transfection Reagent	Thermo Fisher Scientific	Cat#13778-150
Lipofectamine 2000	Thermo Fisher Scientific	Cat#11668019
Dynabeads Protein A	Thermo Fisher Scientific	Cat#10001D
Dynabeads Protein G	Thermo Fisher Scientific	Cat#10003D
Dynabeads® MyOne™ Streptavidin T1	Thermo Fisher Scientific	Cat#65601
4-Hydroxytamoxifen	Sigma-Aldrich	Cat#H7904
Opti-MEM I	Thermo Fischer Scientific	Cat#31985-047
Propidium iodide	Sigma-Aldrich	Cat#81845
Protease inhibitor cocktail	Sigma-Aldrich	Cat#P8340
Phosphatase inhibitor cocktail 2	Sigma-Aldrich	Cat#P5726
Phosphatase inhibitor cocktail 3	Sigma-Aldrich	Cat#P0044
NuPAGE LDS Sample Buffer (4X)	Sigma-Aldrich	Cat#NP0007
Pierce™ DTT (Dithiothreitol), No-Weigh™ Format	Thermo Fisher Scientific	Cat#20291
Benzonase nuclease purity >99% 25U/µl	Merck Millipore	Cat#70664-3
Proteinase K	Roth	Cat#7528.2
RNase A	Roth	Cat#7156.1
16% Paraformaldehyde, EM-Grade	Science Services GmbH	Cat#E15710
Penicillin-Streptomycin	Sigma-Aldrich	Cat#P4333-100ML
HiMark pre-stained HMW STD	Thermo Fisher Scientific	Cat#LC5699
UltraPure BSA (50 mg/mL)	Thermo Fisher Scientific	Cat#AM2616
Polybrene	Sigma-Aldrich	Cat#H9268
Protamine sulfate	Sigma-Aldrich	Cat#P3369
AsiSI	New England Biolabs	Cat#R0630
N-Ethylmaleimide	Sigma-Aldrich	Cat#E3876
Puromycin	InvivoGen	Cat#70664-3
Hygromycin B Gold solution	InvivoGen	Cat#ant-hg-05
Blasticidin	InvivoGen	Cat#ant-bl-05
CutSmart® Buffer	New England Biolabs	Cat#B7204S
T4 DNA Ligase Buffer	New England Biolabs	Cat#B0202S
Agencourt AMPure XP Beads	Beckman Coulter	Cat#A63881
Agencourt RNAClean XP Beads	Beckman Coulter	Cat#A63987
Odyssey Blocking Buffer in TBS	LI-COR Biosciences	Cat#927-50000

6.5 Compounds

Compound	Target	Concentration
5-FU	Thymidylate Synthase	100µM
ABT-263	BCL2	1µM
ABT-737	BCL2	1µM
Actinomycin D	POL1/2	8µM
AK1	AURKA	10µM
Amlexanox	TBK-IKKe	10µM
AZD-1208	PIM	10µM
AZD-6378	ATR	1µM
AZD-7762	CHK1	10µM
AZD-8931	ERB1-3	50nM
Barasertib	AURKB	10µM
BAY-880	NUAK1	10µM
BCH	SLC7A5	50µM
BEZ-235	mTOR	1µM
BI-2536	PLK1	1µM
BI8622	HUWE1	10µM
BI8626	HUWE1	10µM
Calyculin A	PP1/PP2A	25nM
CBL0137	FACT	5µM
CD532	AURKA	10µM
CHIR-124	CHK1	10µM
Cisplatin	DNA replication	5µM
CVT-313	CDK2	10µM
CX-5461	POL1	1µM
Cymarin	NA/K ATPase	300µM
Cytochalasin D	ACTB polymerization	500µM
DCA	PDH	2mM
DS-1	PIN1	10µM
Enzalutamide	AR	10µM
Etoposide	Topoisomerase II	25µM
Everolimus	mTOR	10µM
Fenretinide	vitamin A analog	10µM
Flavopiridol	CDKs	1µM
GC7	DHPS	1µM
HTH-01-015	NUAK1	10µM
Hydroxyurea	DNA	150µM
Indisulam	CDK	10µM

Compound	Target	Concentration
Irinotecan	Topoisomerase I	25µM
Isogingketin	pre-mRNA splicing	10µM
JQ1	BRDs	2.5µM
KU-60019	ATM	10µM
LDC6007	CDK9	1µM
LY-2603618	CHK1	10µM
MG-132	proteasome	20nM
Mirin	MRN complex	10µM
MK5108	AURKA	10µM
MLN-4924	NAE	10nM
MLN-792	SUMO	1µM
MLN-8237	AURKA	10µM
NMS-873	VCP/p97	10µM
Nocodazole	Microtubule polymerization	1µg/ml
NU7026	DNAPK	10µM
Nutlin-3	p53/MDM2	10µM
NVP-2	CDK9	1µM
Okadaic acid	PP1/PP2A	10nM
Olaparib	PARP	10µM
ON-123300	NUAK1	10µM
OSI-906	IGF1R	500nM
P22077	USP7	10µM
P27600	CDK9	1µM
Palbociclib	CDK4/6	500nM
PD98059	MEK	10µM
PFT	p53/MDM2	10µM
PlaB	splicing	1µM
RA-190	RPN13	1µM
Rapamycin	mTOR	100nM
Retinoic Acid	vitamin A analog	20µM
Salubrinal	eIF2α	1µM
Silvestrol	eIF4A	100nM
SITS	SLC4A2	25µM
SKI-1	Sphingosine Kinase	5µM
Takinib	TAK1	1µM
Talazoparib	PARP	10µM
THAL-SN-032	CDK9	1µM
THZ1	CDK7/12	1µM
THZ531	CDK12	10µM

Compound	Target	Concentration
Tunicamycin	ER stress	2.5 µg/ml
Valproic Acid	HDAC	200µM
VE-822	ATR	10µM
Volasertib	PLK1	10µM
WZ-4003	NUAK1	10µM
XMD-17-51	NUAK1	10µM

6.6 Commercial Kits

Kit	**Manufacturer**	**Identifier**
Duolink In Situ PLA Probe Anti-Rabbit PLUS, Affinity purified Donkey anti-Rabbit IgG (H+L)	Sigma-Aldrich	Cat#DUO92002 RRID: AB_2810940
Duolink In Situ PLA Probe Anti-Mouse MINUS, Affinity purified Donkey anti-Mouse IgG (H+L)	Sigma-Aldrich	Cat#DUO92004 RRID: AB_2713942
Duolink In Situ Wash Buffers, Fluorescence	Sigma-Aldrich	Cat#DUO82049
Duolink In Situ Detection Reagents Green	Sigma-Aldrich	Cat#DUO92014
NGS Fragment High Sensitivity Analysis Kit, 1-6,000 bp, 500 samples	Agilent	DNF-474-05
Standard Sensitivity RNA Analysis Kit (15nt), 500 samples	Agilent	DNF-471-0500
RNeasy Mini Kit	Qiagen	Cat#74106
MinElute PCR Purification Kit	Qiagen	Cat#28006
QIAquick PCR Purification Kit	Qiagen	Cat#28106
QIAquick Gel Extraction Kit	Qiagen	Cat#28704
NEBNext Ultra RNA Library Prep Kit for Illumina	New England Biolabs	Cat#E7530S
NEBNext Poly(A) mRNA Magnetic Isolation Modul	New England Biolabs	Cat#E7490L
NEBNext ChIP-Seq Prep Master Mix Set for Illumina	New England Biolabs	Cat#E6240S
NEBNext Ultra II DNA Library Prep	New England Biolabs	Cat#E7103L
NEBNext Multiplex Small RNA Library Prep Kit	New England Biolabs	Cat#E7560S
NextSeq 500/550 High Output Kit v2 (75cycles)	Illumina	FC-404-2005
Quant-iT Pico Green	Thermo Fischer Scientific	Cat#P7589
ABsolute QPCR Mix, SYBR Green, no ROX	Thermo Fischer Scientific	Cat#AB-1158/B
Quick Blunting Kit	New England Biolabs	Cat#E1201L
T4 DNA Ligase, conc.	New England Biolabs	Cat#M0202M

Kit	**Manufacturer**	**Identifier**
T4 RNA Ligase 2, truncated	New England Biolabs	Cat#M0242L
NEBNext High-Fidelity 2X PCR Master Mix	New England Biolabs	Cat#M0541L
MEGAscript T7 Transcription Kit	Thermo Fischer Scientific	Cat#AM1334
SuperScript III Reverse Transcriptase	Thermo Fischer Scientific	Cat#T18080044
RNaseOUT Recombinant Ribonuclease Inhibitor	Thermo Fischer Scientific	Cat#10777019
ON-TARGETplus Non-targeting Pool	Horizon Discovery Group	Cat#D-001810-10-50
ON-TARGETplus Set of Four siRNA Library- Human Ubiquitin Conjugation Subset 1	Dharmacon	GU-105615 Lot 11107
ON-TARGETplus Set of Four siRNA Library- Human Ubiquitin Conjugation Subset 2	Dharmacon	GU-105625 Lot 11108
ON-TARGET*plus* SMARTpool® siRNA Library - Human Ubiquitin Conjugation Subset 3	Dharmacon	GU-105635 Lot 11117
PTMScan Ubiquitin Remnant Motif (K-ε-GG) Kit	Cell Signaling Technology	Cat#5562
NEBuilder® HiFi DNA Assembly Master Mix	New England Biolabs	Caat#E2621L

6.7 Oligonucleotides

Sequence 5' – 3'	Source	Oligo
[P]GCGTGATGNNNNNNNNGATCGTCGGACTGTAGAACTCTGAACCCCTATAGTGAGTCGTATTACCGGCCTCAATCGAA	(Yan et al., 2017)	A1_Bottom
CGATTGAGGCCGGTAATACGACTCACTATAGGGGTTCAGAGTTCTACAGTCCGACGATCNNNNNNNNCATCACGC	(Yan et al., 2017)	A1_Top
[P]GGAACGACNNNNNNNNGATCGTCGGACTGTAGAACTCTGAACCCCTATAGTGAGTCGTATTACCGGCCTCAATCGAA	(Yan et al., 2017)	A2_Bottom
CGATTGAGGCCGGTAATACGACTCACTATAGGGGTTCAGAGTTCTACAGTCCGACGATCNNNNNNNNGTCGTTCC	(Yan et al., 2017)	A2_Top
[P]GATCATCANNNNNNNNGATCGTCGGACTGTAGAACTCTGAACCCCTATAGTGAGTCGTATTACCGGCCTCAATCGAA	(Yan et al., 2017)	A3_Bottom
CGATTGAGGCCGGTAATACGACTCACTATAGGGGTTCAGAGTTCTACAGTCCGACGATCNNNNNNNNTGATGATC	(Yan et al., 2017)	A3_Top
[P]GATGTCGTNNNNNNNNGATCGTCGGACTGTAGAACTCTGAACCCCTATAGTGAGTCGTATTACCGGCCTCAATCGAA	(Yan et al., 2017)	A4_Bottom
CGATTGAGGCCGGTAATACGACTCACTATAGGGGTTCAGAGTTCTACAGTCCGACGATCNNNNNNNNACGACATC	(Yan et al., 2017)	A4_Top
[P]GGATGATGNNNNNNNNGATCGTCGGACTGTAGAACTCTGAACCCCTATAGTGAGTCGTATTACCGGCCTCAATCGAA	(Yan et al., 2017)	A5_Bottom
CGATTGAGGCCGGTAATACGACTCACTATAGGGGTTCAGAGTTCTACAGTCCGACGATCNNNNNNNNCATCATCC	(Yan et al., 2017)	A5_Top
[P]GCGGTCGTNNNNNNNNGATCGTCGGACTGTAGAACTCTGAACCCCTATAGTGAGTCGTATTACCGGCCTCAATCGAA	(Yan et al., 2017)	A6_Bottom
CGATTGAGGCCGGTAATACGACTCACTATAGGGGTTCAGAGTTCTACAGTCCGACGATCNNNNNNNNACGACCGC	(Yan et al., 2017)	A6_Top
CAAGCAGAAGACGGCATACGAGATCGAGTAATGTGACTGGAGTTCCTTGGCACCCGAGAATTCCA	(Endres et al., 2021)	RPI_01
CAAGCAGAAGACGGCATACGAGATTCTCCGGAGTGACTGGAGTTCCTTGGCACCCGAGAATTCCA	(Endres et al., 2021)	RPI_02
CAAGCAGAAGACGGCATACGAGATAATGAGCGGTGACTGGAGTTCCTTGGCACCCGAGAATTCCA	(Endres et al., 2021)	RPI_03
CAAGCAGAAGACGGCATACGAGATGGAATCTCGTGACTGGAGTTCCTTGGCACCCGAGAATTCCA	(Endres et al., 2021)	RPI_04
CAAGCAGAAGACGGCATACGAGATTTCTGAATGTGACTGGAGTTCCTTGGCACCCGAGAATTCCA	(Endres et al., 2021)	RPI_05
CAAGCAGAAGACGGCATACGAGATACGAATTCGTGACTGGAGTTCCTTGGCACCCGAGAATTCCA	(Endres et al., 2021)	RPI_06

Sequence 5’ – 3’	**Source**	**Oligo**
CAAGCAGAAGACGGCATACGAGATAGCTTCAGGTGACTGGAGTTCCTTGGCACCCGAGAATTCCA	(Endres et al., 2021)	RPI_07
CAAGCAGAAGACGGCATACGAGATGCGCATTAGTGACTGGAGTTCCTTGGCACCCGAGAATTCCA	(Endres et al., 2021)	RPI_08
CAAGCAGAAGACGGCATACGAGATCATAGCCGGTGACTGGAGTTCCTTGGCACCCGAGAATTCCA	(Endres et al., 2021)	RPI_09
CAAGCAGAAGACGGCATACGAGATTTCGCGGAGTGACTGGAGTTCCTTGGCACCCGAGAATTCCA	(Endres et al., 2021)	RPI_10
CAAGCAGAAGACGGCATACGAGATGCGCGAGAGTGACTGGAGTTCCTTGGCACCCGAGAATTCCA	(Endres et al., 2021)	RPI_11
CAAGCAGAAGACGGCATACGAGATCTATCGCTGTGACTGGAGTTCCTTGGCACCCGAGAATTCCA	(Endres et al., 2021)	RPI_12
TGGAATTCTCGGGTGCCAAGG	Illumina	RA3
GCCTTGGCACCCGAGAATTCCA	Illumina	RTP
AATGATACGGCGACCACCGAGATCTACACGTTCAGAGTTCTACAGTCCGA	Illumina	RP1
GAGUUUGGAGUUUGUGAAG[dT][dT]	(Heidelberger et al., 2018)	siHUWE1
AGCTACGGAACTCTTGTGCGATGGTGAGCAAGGGCGAG	This study	MYC-GFP cloning frw
GATCCGTCGACACTAGTTTACTTGTACAGCTCGTCCATGCC	This study	MYC-GFP cloning rev
GCATGGACGAGCTGTACAAGTAAACTAGTGTCGACGGATCCGCC	This study	MYC-GFP cloning frw 2
TCCTCGCCCTTGCTCACCATCGCACAAGAGTTCCGTAGCTG	This study	MYC-GFP cloning rev 2
GCGCCAGTCCTCCGACAGACTGAGTCGGCCGGTGGATCCAATGGCCAGCGATTACAAGGAC	This study	APEX2-MYC cloning frw
CGTTAGGGGGGGGGAGGGAGAGGGGCGGATCCGTCGACACAGTTATGCACAAGAGTTCCGTAGC	This study	APEX2-MYC cloning rev
CTACCACCCTCATCTGAATCC	(Endres et al., 2021)	ChIP NCL frw
TTGTCTCGCTGGGAAAGG	(Endres et al., 2021)	ChIP NCL rev
TTTTCTCACATTGCCCCTGT	(Endres et al., 2021)	ChIP negative frw
TCAATGCTGTACCAGGCAAA	(Endres et al., 2021)	ChIP negative frw

6.8 Plasmid

Construct	Description
SFFV_puro	Empty lentiviral expression vector
SFFV_ΔN-MYC_puro	Lentiviral expression vector with CDS of human MYC lacking AA1-354
SFFV_ΔC-MYC_puro	Lentiviral expression vector with CDS of human MYC lacking AA355-439
SFFV_ΔTAD-MYC_puro	Lentiviral expression vector with CDS of human MYC lacking AA1-143
SFFV_ΔBox-MYC_puro	Lentiviral expression vector with CDS of human MYC lacking AA18-33;45-63;128-143;188-199;258-267;304-317
SFFV_ΔBoxI-MYC_puro	Lentiviral expression vector with CDS of human MYC lacking AA45-63
SFFV_ΔBoxII-MYC_puro	Lentiviral expression vector with CDS of human MYC lacking AA128-143
SFFV_WT-MYC_puro	Lentiviral expression vector with CDS of human MYC
SFFV_K-less-MYC_puro	Lentiviral expression vector with CDS of human MYC with all lysine residues substituted by arginine
SFFV_APEX2-MYC_puro	Lentiviral expression vector with the CDS of the APEX2 construct fused to n-terminus of the CDS of human wildtype MYC

6.9 Software

Package	Source	Availability
FASTQ Generation software v1.0.0	Illumina	http://illumina.com
FastQC v0.11.3	http://www.bioinformatics.babraham.ac.uk/projects/fastqc/	https://www.bioinformatics.babraham.ac.uk/projects/fastqc/
Tophat v2.1.0	Kim et al. (2013)	https://ccb.jhu.edu/software/tophat/index.shtml
Bowtie v1.2	Langmead et al. (2009)	http://bowtie-bio.sourceforge.net/index.shtml
Bowtie v2.3.2	Langmead and Salzberg (2012)	http://bowtie-bio.sourceforge.net/bowtie2/index.shtml
MACS v1.4.1	Zhang et al. (2008)	https://github.com/taoliu/MACS
BEDtools v2.26.0	Quinlan and Hall (2010)	https://bedtools.readthedocs.io/en/latest/

Package	**Source**	**Availability**
SAMtools v1.3	Li et al. (2009)	http://www.htslib.org/
ChimeraX-1.1.1	UCSC	https://www.cgl.ucsf.edu/
NGSplot v2.61	Shen et al. (2014)	https://github.com/shenlab-sinai/ngsplot
Integrated Genome Browser v9.0.0	Freese et al. (2016)	https://bioviz.org/
GraphPad Prism v5/6.0 for Mac	GraphPad software	https://www.graphpad.com/scientific-software/prism/
Harmony High Content Imaging and Analysis Software	PerkinElmer	http://www.perkinelmer.de/product/harmony-4-8-office-hh17000001
StepOne software v2.3	StepOne	https://www.thermofisher.com/de/de/home/technical-resources/software-downloads/StepOne-and-StepOnePlus-Real-Time-PCR-System.html
BD FACSDIVA Software v6.1.2	BD	http://www.bdbiosciences.com/us/instruments/research/software/flow-cytometry-acquisition/bd-facsdiva-software/m/111112/overview
EdgeR	Robinson et al. (2010)	https://bioconductor.org/packages/release/bioc/html/edgeR.html
R version 3.6.3	The R Foundation	https://www.R-project.org/
UMI-tools v1.0.0	Smith et al. (2017)	https://umi-tools.readthedocs.io/en/latest/index html
Image Studio version 5.2.5	LI-COR	http://opensource.licor.com/licenses/ImageStudio/index.html

6.10 Equipment

Equipment	**Manufacturer**
5200 Fragment Analyzer	Agilent
LAS-4000 mini	Fujifilm
Odyssey CLx	Li-Cor
Casy cell counter	Innovatis
Countess Automated Cell Counter	Thermo Fisher Scientific
Avanti J-26 XP	Beckman Coulter
Eppendorf 5417 R	Eppendorf
Eppendorf 5425	Eppendorf
Eppendorf 5430	Eppendorf
Galaxy MiniStar	VWR
Multifuge 1S-R	Heraeus
NextSeq 500	Illumina
NextSeq 2000	Illumina

Equipment	**Manufacturer**
BD FACS Canto II	BD Biosciences
BD FACS Aria III	BD Biosciences
Spectrofluorometer	Thermo Fisher Scientific
NanoDrop 1000	Thermo Fisher Scientific
Mastercycler pro S	Eppendorf
C1000 Thermal cycler	Bio-Rad
SP2	Leica
Operetta High Content	Perkin Elmer
Operetta CLS High Content	Perkin Elmer
Dry Bath System	Starlab
Thermomixer®comfort	Eppendorf
Vortex-Genie	Scientific Industries
Digital Sonifier W-250 D	Branson
M220	Covaris
epMotion® 5075	Eppendorf

7 Methods

Substantial parts of this chapter have been published in Endres et al. (2021) and Solvie et al. (*in press*).

7.1 Bacterial Transformation and plasmid DNA isolation

50 µl of competent XL1-Blue cells were thawed on ice and mixed with approximately 100 ng of pure plasmid or 1 µg of cloning reaction product. The mixture was incubated on ice for 30 min followed by 2 min at 42°C (heat shock) and another 2 min on ice. Subsequently, 750 µl prewarmed LB medium without antibiotics were added and incubated for 30 min at 37°C. Cells were spun down shortly, excessive LB removed and plated on LB-plates containing appropriate antibiotics. Consecutive to incubation over night at 37°C, single colonies were picked, grown over night at 37°C in 3 ml of LB-medium containing appropriate antibiotics while shaking. For analytic preparations (miniprep), half of the volume was spun down and resuspended in 200 µl Miniprep Resuspension Buffer. With the addition of 200 µl Miniprep Lysis Buffer the cells were lysed for 5 min and the reaction stopped with 200 µl Miniprep Precipitation Buffer. Following mixing by inversion, DNA was separated from cell debris by centrifugation at 20,000 rcf for 5 min, transferred into a fresh Eppendorf tube and washed with 500 µl Isopropanol. DNA was spun down for 30 min at 20,000 rcf, washed with 700 µl 70% Ethanol and again spun down. Drying was conducted by aspiration of all residual liquid and allowing the sample to evaporate all Ethanol at room temperature with open lid for 5 min. The pure DNA was resuspended in 20 µl of TE or H_2O.

For large-scale isolation (maxiprep) the PureLink HiPure Plasmid Maxiprep Kit (Life Technologies) was used following manufacturer's instructions and final eluate adjusted to a DNA concentration of 1 µg/µl.

7.2 Cloning

Cloning was performed using the NEBuilder HiFi DNA assembly kit (NEB) following manufacturer's instructions and enzymatic digestion. MYC-GFP fusion protein was cloned using the primer MYC-GFP cloning frw and rev to amplify eGFP CDS and MYC-GFP cloning frw 2 and rev 2 to amplify a lentiviral expression backbone carrying the MYC CDS (WT-MYC) with respective overhang.

The APEX2-MYC fusion protein construct was a kind gift by Petra Beli. The fusion protein was amplified using the APEX2-MYC cloning frw and rev primer and the empty lentiviral expression backbone linearized using AgeI and SpeI restriction digest.

The K-less-MYC construct was cloned from a lentiviral expression construct carrying a hygromycin resistance gene (Jaenicke et al., 2016) into a lentiviral expression construct carrying a hygromycin resistance gene using AgeI and SpeI.

ΔBoxI-MYC, ΔBoxII-MYC and ΔTAD-MYC were kind gifts from Julia Hofstetter-Hadry. ΔBox-MYC, ΔC-MYC and ΔN-MYC were kind gifts from Beril Kadioglu.

7.3 Transfection and lentiviral infection

Transfection of siRNA was performed using RNAiMAX reagent according to manufacturer's protocol. Cells were harvested 72 hrs after transfection. Transfection of cDNA was performed using PEI or Lipofectamine 2000. Cells were harvested 48 hrs after transfection. For lentivirus production, HEK293TN cells were transfected using PEI. For constitutive expression, lentivirus was produced by transfecting cDNA together with the packaging plasmid psPAX.2, and the envelope plasmid pMD2.G. Virus-containing supernatant was harvested between 24 hrs and 48 hrs after transfection. Cells were infected with lentiviral supernatants in the presence of 4 µg/µl polybrene for 24 hrs and subsequently selected with puromycin, if not stated otherwise. U2OS^{MYC-}GFP cells were sorted based on GFP signal with the BD FACS Aria III.

7.4 Immunoblot

Cells were lysed in RIPA lysis buffer (50 mM HEPES pH 7.9, 140 mM NaCl, 1 mM EDTA, 1% Triton X-100, 0.1% SDS, 0.1% sodium deoxycholate) containing protease and phosphatase inhibitors (Sigma-Aldrich) and incubated for 20 min at 4°C with rotation. The lysate was cleared by centrifugation and protein concentration was determined using the BCA assay. The cell lysate (same number of cells or amount of protein) was separated by BisTris-PAGE and transferred to PVDF membranes (Millipore). Membranes were blocked for 1 hr and probed using antibodies against indicated proteins. For visualization the LAS3000 or LAS4000 Mini (Fuji) or Odyssey CLx Imaging System (LICOR Biosciences) were used.

7.5 Immunoprecipitation

Cells were resuspended in lysis buffer (20 mM HEPES pH 7.9, 180 mM NaCl, 1.5 mM magnesium dichloride, 10% glycerol, 0.2% NP-40) supplemented with a cocktail of protease and phosphatase inhibitors (Sigma-Aldrich) and 20 mM N-Ethylmaleimide. After brief sonication, samples were incubated on ice for 30 min with 50 U Benzonase and cleared by centrifugation. Dynabeads (20 µl of Protein A/G beads, Thermo Fisher Scientific) were pre-incubated overnight at 4°C with rotation in the presence of 5 mg/ml BSA and 3 µg antibody targeting indicated proteins. Co-immunoprecipitation was carried out in lysis buffer with an adjusted amount of lysate according to protein concentration and incubated for 6 hrs at 4°C. Elution of dynabeads was performed by heating in 2x Laemmli sample buffer (15 mM Tris pH 6.8, 3% SDS, 0.015% bromophenol blue, 10% glycerol, 1.5 mM 1,4-Dithiothreitol) for 5 min at 95°C. Samples were analyzed by immunoblotting.

7.6 DNA fiber assay

Cells were treated as indicated and afterwards first labelled for 20 min with 5-chloro-2-deoxyuridine (CldU, 25 µM) followed by 20 min incubation with 5-iodo-2-deoxyuridine (IdU, 25 µM) and another hour with CldU (25 µM). For fork degradation assay, cells were subsequently treated with HU (2 mM, 4 hrs) and if indicated with Mirin (50 µM, 4 hrs). For fork restart assay, cells were additionally incubated in fresh medium for one hour with IdU (25 µM). Fibers were spread on glass slides and acid treated. The labelled tracks were incubated afterwards at 20ºC for 1 hr with rat anti-BrdU antibody (for BrdU and CldU) and mouse anti-BrdU antibody (for BrdU and IdU). Slides were fixed with 4% paraformaldehyde and incubated for 2 hrs at 20°C with Alexa Fluor 555-conjugated goat anti-rat antibody and Alexa Fluor 488-conjugated goat anti-mouse antibody. Images were acquired using an Axio Scope A1 using ZEN software for image acquisition and ImageJ was used for analysis of the fibers.

7.7 FRAP

For FRAP experiments U2OS cells stably expressing MYC-GFP were seeded in 8 well chambered cover slips (cellvis) and treated with MG-132 two hours before imaging. U2OS cells transfected with free cytosolic GFP were used as a control. The FRAP measurements were performed with the confocal laser scanning microscope LSM710 (Zeiss, Germany). A time series with 100 images was recorded with a 63x/1.4 NA oil immersion objective and 488 nm excitation wavelength. After five images a part of a Myc shell (large multimers) or the whole shell (small multimers) were bleached with maximal laser power at 488 nm and 555 nm. Subsequently 95 images were acquired over several minutes to measure the fluorescence recovery in the bleached region.

7.8 Proximity Ligation Assay

Cells were seeded in a 384 well format (PerkinElmer) and allowed to settle overnight. Where indicated, cells were treated accordingly. Fixation was performed with 4% paraformaldehyde with subsequent washing in PBS and permeabilized with 0.3% Triton X-100. Cells were blocked in 5% BSA in PBS for 60 min and incubated overnight at 4°C with primary antibodies against indicated proteins in 5% BSA in PBS. Cells were treated for 1 hr at 37°C with plus (Sigma-Aldrich) and minus (Sigma-Aldrich) probes directed at rabbit and mouse antibodies, respectively, and ligated for 30 min at 37°C. Next, in situ PCR amplification was done with Alexa 488-/647-conjugated oligonucleotides (Sigma-Aldrich) for 2 hrs at 37°C. Samples were counter-stained with Hoechst 33342 (Thermo Fisher Scientific). Image acquisition was done using the Operetta CLS High-Content Analysis System with 40x magnification (PerkinElmer) and were processed using Harmony High Content Imaging and Analysis Software (PerkinElmer) and R. Wells with focus error were discarded.

7.9 siRNA screen

For the siRNA-PLA screen 1,250 U2OS$^{MYC\text{-}tet\text{-}on}$ were seeded per well in a 384 well format (PerkinElmer) and allowed to settle for 10 h. Transfection was performed using RNAiMAX reagent (Thermo Fisher Scientific) according to manufacturer's protocol using a pool of 4 siRNAs against each listed E3-ligase from ubiquitin conjugation libraries (Dharmacon, GU-105635, GU-105625, GU-105615). 16 hrs post transfection; 1 µg/ml doxycycline or equal amounts of ethanol were added for 24 h. Where indicated, MG-132 (20 µM, Calbiochem / Merck) was added 4 hrs before fixation with 4% paraformaldehyde. Proximity Ligation Assay was performed as described. The readout parameter for statistical analysis was foci/nucleus as produced by the Harmony High Content Imaging and Analysis Software (PerkinElmer). Statistical analysis was performed in R by calculating the fold change to the non-targeting siRNA of the respective replicate and applying Welch's t-test over all replicates for each siRNA to the non-targeting control with subsequent correction for multiple testing using Benjamini and Hochberg's FDR method. To reduce the influence of outliers, generated by transfection, Proximity Ligation Assay and image acquisition, a modified Z-score ("robust Z-score") (Iglewicz and Hoaglin, 1993) was calculated as follows:

$$Z_{rob} = \frac{|x_i - \mathrm{med}(x_{i..n})|}{1.4826 * \mathrm{med}(|x_i - \mathrm{med}(x_{i..n})|)}$$

For the siRNA-Immunofluorescence screen, RNAi Cherry-pick Library (SMARTpool, Horizon Discovery) was diluted following manufacturer's instructions. U2OS$^{MYC\text{-}tet\text{-}on}$ were seeded in 96-well plates (PerkinElmer) and transfected the next day utilizing Lipofectamin RNAiMAX (Thermo Fisher Scientific) according to manufacturer's instructions with a final concentration of 25 nM siRNA per well. The following day medium was changed and MYC expression induced by Dox addition (1 µg/ml, 24 hrs). Cells were treated with indicated inhibitors for 4 hrs (MG-132, 20 µM; Pladienolide B, 1 µM; CBL0137, 5 µM) or permitted to mild heat shock (30 min, 42°C). Fixation and staining were performed 48 hrs after transfection as described in chapter Immunofluorescence staining.

7.10 BLISS/BLISS8

The original BLISS protocol was adapted and modified from Yan et al. (2017). For experiments in U2OS cells expressing doxycycline inducible MYC, cells were plated in a 24-well plate (Greiner) and incubated with ethanol or doxycycline (1 µg/ml) from the following day onwards for 24 h. Where indicated, etoposide was added (3 h, 25 µM). Cells were fixed by addition of paraformaldehyde directly to the media to a final concentration of 3.7%, washed with PBS and either stored at 4°C or directly processed. Lysis was performed by incubation in lysis buffer 1 (10 mM Tris-HCl, 10 mM NaCl, 1 mM EDTA, 0.2% Triton X-100, pH 8) for 1 hr at 4°C, brief rinsing in PBS and incubation in lysis buffer 2 (10 mM Tris-HCl, 150 mM NaCl, 1 mM EDTA, 0.3% SDS, pH 8) for 1 hr at 37°C. Following rinsing in PBS, cells were equilibrated in CutSmart buffer (New England Biolabs) previous to restriction enzyme digestion using AsiSi (New England Biolabs) according to manufacturer's protocol. Following rinsing in PBS and equilibrating the cells in CutSmart buffer, blunting of double-strand breaks using Quick Blunting Kit (New England Biolabs) following manufacturer's protocol was performed. Sense and antisense adapter-oligos were annealed by heating them for 5 min at 95°C, followed by a gradual cooldown to 25°C over a period of 45 min. Consecutive to equilibration in CutSmart buffer (New England Biolabs) and T4 Ligase buffer (New England Biolabs) annealed adapters were dispensed on samples and ligated using T4 DNA Ligase (New England Biolabs) using manufacturer's recommendations for 16 hrs at 16°C. Excessive Adapters were removed by repeated rinsing in a high-salt wash buffer (10 mM Tris-HCl, 2M NaCl, 2 mM EDTA, 0.5% Triton X-100, pH 8). Genomic DNA was extracted in DNA extraction buffer (1% SDS, 100 mM NaCl, 50 mM EDTA, 10 mM Tris-HCl, pH 8) supplemented with Proteinase K (1 mg/ml, Roth) for 16 hrs in a thermo-shaker at 55°C. DNA was isolated by phenol-chloroform extraction and isopropanol precipitation, resuspended in TE buffer and sonicated using the Covaris Focused Ultrasonicator M220 for 2 min to achieve a fragment size of 300-500 bp. Fragment size was assessed on the Fragment Analyzer (Agilent) using the NGS Fragment High Sensitivity Analysis Kit (1-6,000 bp; Agilent). The DNA was concentrated using Agentcourt AMPure XP Beads (Beckman Coulter), transcribed into RNA and DNA digested using MEGAscript™ T7 Transcription Kit (Thermo Fischer Scientific) following manufacturer's recommendations. A two-sided RNA cleanup with a ratio of 0.4 followed by 0.2 was performed using Agencourt RNAClean XP Beads (Beckman Coulter). RNA concentration was assessed on the Fragment Analyzer (Agilent) by using Standard Sensitivity RNA Analysis Kit (Agilent). Library preparation was performed by ligating the RA3 adapter to the samples with a T4 RNA Ligase 2 (New England Biolabs) supplemented with Recombinant Ribonuclease Inhibitor (Thermo Fischer Scientific). Samples were reverse transcribed using SuperScript III Reverse Transcriptase kit (Thermo Fischer Scientific) and library indexing and amplification performed using NEBNext High-Fidelity 2X PCR Master Mix (New England Biolabs) with RP1- and desired RPI-primer. The libraries were cleaned up using Agentcourt AMPure XP Beads (Beckman Coulter), quality, quantity and fragment size assessed on the Fragment Analyzer (Agilent) using the NGS Fragment High Sensitivity Analysis Kit (1-6,000 bp; Agilent). Sequencing was performed on the NextSeq500 Illumina platform for 75 cycles or on the NextSeq2000 Illumina platform with 72 cycles for read1 and 56 for read2. Adapters and oligos were custom synthesized and ordered from IDT. Unique Molecular Identifiers (UMIs) generated by random incorporation of the four standard dNTPs using the 'Machine mixing' option.

7.11 Immunofluorescence

Cells were plated in a 96-well plate (Greiner) and treated as indicated. For cell cycle immunofluorescence, cells were pulsed with 10 µM EdU (Jena Bioscience) 30 minutes before fixation. Fixation was performed with 4% paraformaldehyde in PBS. After washing with PBS, cells were permeabilized with 0.3% Triton X-100 in PBS and blocked with 5% BSA in PBS. Newly synthesized DNA was visualized by performing a copper(I)-catalyzed azide-alkyne cycloaddition (100 mM Tris pH 8.5, 4 mM CuSO4, 10 mM AFDye 647 Azide (Jena Bioscience), 10 mM L-Ascorbic Acid). Samples were stained with primary antibodies against indicated proteins in 5% BSA in PBS overnight at 4°C and after rinsing with PBS, incubated with secondary antibody (Thermo Fisher Scientific) for 1 hr at room temperature. Counter-staining was performed using Hoechst 33342 (Sigma-Aldrich). Images were taken with an Operetta High-Content Imaging System or Operetta CLS High-Content Imaging System with 20x/40x/63x magnification. Images were processed using Harmony High Content Imaging and Analysis Software and R. Cells were grouped into cell cycle phase according to EdU and Hoechst staining of the control condition.

7.12 Flow cytometry

Cells were treated with trypsin for 5 min to ensure detachment from the cell culture dish. Preceding, supernatant medium was collected. Detached cells and supernatant were centrifuged at 4°C for 5 min at 400 rcf. After a washing step with PBS, the pellet was resuspended in 100 µl Annexin V binding buffer and incubated with 2 µl Pacific Blue-conjugated Annexin V (25 µg/ml). Incubation was performed for 15 min in the dark and followed by addition of 400 µl of Annexin V binding buffer and 5 µl of PI (1 mg/ml). Data were acquired using the FACScanto II (BD Biosciences), analyzed with BD FACSDiva 6.1.2 and R using the packages flowCore (2.8.0) and ggcyto (1.24.1).

7.13 Inhibitor screening

Cells were seeded in 384-well plates (PerkinElmer) and 4 hours before fixation, compounds were dispensed in indicated concentrations (6.5 Compounds) with an epMotion 5075 liquid handling station (Eppendorf). Fixation and staining were performed as described (7.11 Immunofluorescence).

7.14 SILAC-based ubiquitin remnant profiling

U2OS SILAC-labeled cells were transfected with siRNAs targeting non-targeting control or HUWE1 as previously described or treated with BI8626 (10 µM, 24 hrs). Cells were lysed in modified RIPA buffer (50 mM Tris pH 7.5, 150 mM NaCl, 1 mM EDTA, 1% NP-40, 0.1% sodium deoxycholate) supplemented with protease inhibitors (Complete protease inhibitor cocktail tablets, Roche Diagnostics), 1 mM sodium orthovanadate, 5 mM β-glycerophosphate, 5 mM sodium fluoride and 10 mM N-ethylmaleimide. Proteins were digested with endoproteinase Lys-C (Wako Chemicals) and sequencing grade modified trypsin (Sigma-Aldrich). Modified peptide enrichment was done using di-glycine-lysine antibody resin (Cell Signaling Technology, 5562). Peptides were analyzed on a quadrupole Orbitrap mass spectrometer (Q Exactive Plus, Thermo Scientific) equipped with a UHPLC system (EASY-nLC 1000, Thermo Scientific) as described (Kelstrup et al., 2012; Michalski et al., 2012). MaxQuant (development version 1.5.2.8) was used to analyze the raw data files (Cox and Mann, 2008). Parent ion and MS2 spectra were searched against a human protein database obtained from UniProtKB released in May 2016 using Andromeda search engine (Cox et al., 2011). Experimental details were described previously (Heidelberger et al., 2018).

7.15 APEX2-MYC quantitative mass spectrometry

U2OS expressing an APEX2-MYC fusion protein were incubated with medium containing 1 mM Biotin-Phenol (Iris Biotech) for 2 hrs at 37°C. H_2O_2 was added to a final concentration of 1 mM and incubated for 2 min. Biotinylation was stopped by washing three times with quenching solution (10 mM sodium azide, 10 mM L-sodium ascorbate, 5 mM Trolox in PBS) containing protease and phosphatase inhibitors (Sigma-Aldrich) and 10 mM N-Ethylmaleimide and three more times in PBS. Cells were collected by centrifugation and lysed in RIPA buffer (50mM Tris-HCl pH 7.5, 0.1% SDS, 0.5% Na-Deoxycholate, 1% Triton X-100, 150 mM NaCl) containing protease and phosphatase inhibitors (Sigma-Aldrich). NaCl was added to a final concentration of 1 M, and cells lysed for 10 min rotating at 4°C. Lysates were sonicated using a Branson Sonifier in a 10 sec: 45 sec off cycle with 3 cycles and 20% duty output and subsequently cleared by centrifugation. RIPA devoid of NaCl was used to dilute samples to a final concentration of 200 mM NaCl. Biotinylated peptides were enriched using Pierce High Capacity NeutrAvidin Agarose (Thermo Fisher Scientific) according to manufacturer's recommendation. Samples were washed once with RIPA devoid of SDS, three times in PBS containing 2 M Urea (pH 8) and one more time in RIPA. Sample processing procedure for APEX2 TMT mass spectrometry was adapted from Cho et al (Cho et al., 2020). All following steps were performed at room temperature, unless specified otherwise. Proteins were digested on-bead for 1 hr in 2 M urea in 50 mM Tris-HCl (pH 7.5) containing 1 mM dithiothreitol and 0.4 µg of MS-approved trypsin (Serva) per sample. Supernatants were collected, and beads were washed twice with 2 M urea in 50 mM Tris-HCl (pH 7.5). Wash supernatants were collected and combined with respective peptide supernatants. Cysteines were reduced with 4 mM dithiothreitol and alkylated with 10 mM chloroacetamide. Samples were digested overnight with an additional 0.5 µg of trypsin. Digestion was stopped by adding fluoroacetic acid to 1%, and precipitates were removed by centrifugation after a 30 min incubation at 4°C. Supernatants were desalted using reversed-phase C18 StageTips (Rappsilber et al., 2007) and eluted in 50% ACN, 0.1% formic acid. Eluates were vacuum centrifuged until completely dry and reconstituted in 25 µl of 50 mM HEPES pH 8.5, 30% ACN. Samples were barcoded with 0.1 µg of acetonitrile-dissolved TMTPro labels (Thermo Scientific) for 1 hr and quenched with 5% hydroxylamine for 15 min (Li et al., 2020). An equal aliquot (5% vol) of each sample was mixed and the ratio check was performed as described (Zhang and Elias, 2017). Samples were vacuum-centrifuged until completely dry and stored at -80°C. After the ratio check, samples were reconstituted in 1% trifluoroacetic acid and masses adjusted treatment-wise. Samples were mixed together and desalted using reversed-phase C18 StageTips.

Samples were analyzed on a quadrupole Orbitrap mass spectrometer (Exploris 480, Thermo Scientific) equipped with a UHPLC system (EASY-nLC 1200, Thermo Scientific). They were loaded onto a C18 reversed-phase column (55 cm length, 75 mm inner diameter, packed in-house with ReproSil-Pur 120 C18-AQ 1.9-mm beads, Dr. Maisch GmbH) and eluted with a gradient from 2.4 to 36% acetonitrile containing 0.1% formic acid in 120 min. The mass spectrometer was operated in data-dependent mode, automatically switching between MS and MS2 acquisition. Survey full scan MS spectra (m/z 300–1,650, resolution: 60,000, target value: 3×10^6, maximum injection time: 40 ms) were acquired in the Orbitrap. The 20 most intense precursor ions were sequentially isolated, fragmented by higher energy C-trap dissociation (HCD) and scanned in the Orbitrap mass analyzer (normalized collision energy: 33%, resolution: 15,000, target value: 1×10^5, maximum injection time: 40 ms, isolation window: 0.8 m/z). Precursor ions with unassigned charge states, as well as with charge states of +1 or higher than +6, were excluded from fragmentation. Precursor ions already selected for fragmentation were dynamically excluded for 30 s. TurboTMT scan feature (TMTPro reagent) was implemented.

7.16 *d*STORM imaging

All *d*STORM measurements were performed on an inverse wide-field fluorescence microscope (IX-71; Olympus) with a 639 nm diode laser (Genesis MX639-1000, Coherent, Cleanup 640/10, Chroma) for excitation of Alexa Fluor 647. The laser was focused on the back-focal plane of an oil-immersion objective (APON 60x NA 1.45; Olympus). Emission light was separated from excitation light by a dichroic mirror (ZT405/514/635rpc, Chroma), spectrally filtered by a bandpass filter (Brightline HC 679/41; Semrock) and subsequently projected onto an EM-CCD camera chip (512 x 512 pixel at 16 µm; Ixon DU 897; Andor). The pixel size of the resulting image was determined to 128 nm. Measurements were performed in PBS-based photoswitching buffer containing 100 mM β-mercaptoethylamine (#M6500, Sigma-Aldrich) adjusted to pH 7.4. Each acquisition was conducted by illuminating the sample in HILO (Highly inclined and laminated optical sheet) with an irradiation intensity of ~2.5 kW/cm². A series of 15,000 frames was captured with an exposure time of 20 ms. Reconstruction of super-resolved images was performed using rapidSTORM3.3 (Wolter et al., 2012).

Localisations from *d*STORM were further analysed using custom codes (https://github.com/super-resolution/Solvie-et-al-supplement). Images represent localization histograms (20 nm bins) with a logarithmic intensity transform. Localization clusters (that can originate from multiple blink events of individual fluorophores as well as from multiple proteins) were determined using a DBSCAN algorithm (min_points=3, epsilon=20). Clusters were analysed with respect to the distribution of localizations per cluster and of convex hull areas. We estimated an average number of MYC signals per nucleus by recording *d*STORM images under saturating and sparse labelling conditions. From the sparse labelling condition, we estimated 11 ± 0.4 localizations recorded per antibody in 15,000 frames (mean ± S.E.M. from 7 cell nuclei). From saturating conditions, we estimated a localization density of 0.0013 ± 0.0001 (mean ± S.E.M. from 24 regions of interest 4 x 4 µm² of 6 cell nuclei). Assuming that all localizations originate in a 500 ± 200 nm thick slice of the nucleus, we computed a 3-dimensional protein density, which then was multiplied by a nuclear volume of 770 μm^{-3} either reference or short explanation how calculated

Ripley-h functions (Kiskowski et al., 2009) were computed on multiple 4 x 4 μm^2 regions of interest selected from the nucleus of multiple cells and averaged. For comparison we simulated *d*STORM data as a Neyman-Scott (clustered) point process, assuming a homogeneous cluster distribution with n localizations per cluster (where n is a random variable that follows a geometric distribution with mean of 11 localizations per protein, as estimated from experiments with sparse labelling conditions) and a normal spatial distribution (with sigma according to the localization precision of 12 nm) in each cluster. We also simulated a homogeneous distribution to visualize boundary effects. All simulations were carried out on identical regions of interest and with the same number of localizations. Simulations were repeated 100x to compute 95% confidence intervals for the Ripley-h function.

7.17 ChIP-Rx sequencing

For each ChIP-Rx sequencing experiment, $5x10^7$ cells per immunoprecipitation condition were fixed with formaldehyde (final concentration, 1%) for 5-10 min at room temperature. Fixation was stopped by adding 125 mM glycine for 5 min. Cells were harvested in ice-cold PBS containing protease and phosphatase inhibitors (Sigma-Aldrich). All further used buffers also contained protease and phosphatase inhibitors. As exogenous control (spike-in), murine NIH 3T3 cells were added at a 1:10 cell ratio during cell lysis. Cell lysis was carried out for 20 min in lysis buffer I (5 mM PIPES pH 8.0, 85 mM KCl, 0.5% NP-40) and nuclei were collected by centrifugation at 1,500 rpm for 20 min at 4°C. Crosslinked chromatin was prepared in lysis buffer II (10 mM Tris pH 7.5, 150 mM NaCl, 1 mM EDTA, 1% NP-40, 1% sodium deoxycholate, 0.1% SDS) and fragmented by sonication (total duration, 20 min with 10 s pulses and 45 s pausing) or by using the Covaris Focused Ultrasonicator M220 for 50 min per ml lysate. Fragment size of 150-300 bp was validated by agarose gel electrophoresis. Chromatin was centrifuged for 20 min at 14,000 rpm at 4°C before IP. For each IP reaction, 100 µl Dynabeads Protein A and Protein G (Thermo Fisher Scientific) were pre-incubated overnight with rotation in the presence of 5 mg/ml BSA and 15 µg of indicated antibody at 4°C. Chromatin was added to the beads, and IP was performed for at least 6 hrs at 4°C with rotation. Beads were washed three times each with washing buffer I (20 mM Tris pH 8.1, 150 mM NaCl, 2 mM EDTA, 1% Triton X-100, 0.1% SDS), washing buffer II (20 mM Tris pH 8.1, 500 mM NaCl, 2 mM EDTA, 1% Triton X-100, 0.1% SDS), washing buffer III (10 mM Tris pH 8.1, 250 mM LiCl, 1 mM EDTA, 1% NP-40, 1% sodium deoxycholate; including a 5 min incubation with rotation), and TE buffer (Thermo Fisher Scientific). Chromatin was eluted twice by incubating with 150 ml elution buffer (100 mM NaHCO3, 1% SDS) for 15 min with rotation. Input samples and eluted samples were de-crosslinked overnight. Protein and RNA were digested with proteinase K and RNase A, respectively. DNA was isolated by phenol-chloroform extraction and ethanol precipitation and analyzed by qPCR using StepOnePlus Real-

Time PCR System (Thermo Fisher Scientific) and SYBR Green Master Mix (Thermo Fisher Scientific) or sequencing on the Illumina Next-Seq500.

Prior to library preparation, DNA was quantified using the Quant-iT PicoGreen dsDNA assay (Thermo Fisher Scientific). DNA library preparation was performed using the NEBNext ChIP-Seq Library Prep Master Mix Set for Illumina (New England Biolabs) or NEBnext Ultra II DNA Library Prep Kit (New England Biolabs) following manufacturer's instructions. Quality of the library was assessed on the Fragment Analyzer (Agilent) using the NGS Fragment High Sensitivity Analysis Kit (1-6,000 bp; Agilent). Finally, libraries were subjected to cluster generation and base calling for 75 cycles on Illumina NextSeq500 platform.

7.18 Bioinformatics

Sequencing libraries were subjected to Illumina NextSeq 500/2000 sequencing according to the manufacturer’s instructions. After base calling with Illumina’s FASTQ Generation software v1.0.0, high quality PF-clusters were selected for further analyses and sequencing quality was ascertained using FastQC. ChIP-Rx samples were mapped separately to the human hg19 and to the murine mm10 genome using Bowtie1 (Langmead et al., 2009) or Bowtie 2 (Langmead and Salzberg, 2012) with default parameters. ChIP-Rx spike-in normalized reads were calculated by dividing the number of mapped reads mapped to hg19 by the number of reads mapped to mm10 for each sample and multiplying this ratio with the smallest number of reads mapped to mm10 for any sample. RNAseq samples were mapped to hg19 using Bowtie2 (Langmead and Salzberg, 2012) and samples were normalized to the number of mapped reads in the smallest sample. Reads per gene were counted using the “summarizeOverlaps” function from the R package “GenomicAlignments” using the “union”-mode and Ensembl genes. Non- and weakly expressed genes were removed (mean count over all samples <1). Differentially expressed genes were called with edgeR and p-values were adjusted for multiple-testing using the Benjamini-Höchberg procedure. Metagene plots were generated with ngs.plot.r (Shen et al., 2014). MYC-reads in promoter regions were determined by processing read-normalized MYC ChIP-Rx bam-files with the BEDtools intersectBed program (Quinlan and Hall, 2010). Promoter regions were defined here as TSS +/- 1 kb.

BLISS/BLISS8 samples were demultiplexed based on their condition-specific barcodes using UMI-tools (Smith et al., 2017), allowing 1 mismatch in the barcode, and separately mapped to hg19 using Bowtie2 (Langmead and Salzberg, 2012) with default parameters. Where indicated, respective samples of biological triplicates were merged preceding to mapping and collectively processed. Samples were filtered against an ENCODE Blacklist file to remove regions of high variance in mappability commonly found in satellite, centromeric and telomeric repeats (Amemiya et al., 2019) using bedtools intersect (Quinlan and Hall, 2010). To allow absolute quantification of double-strand breaks and remove PCR-introduced artifacts, duplicated reads were identified based on their UMI, grouped and deduplicated using UMI-tools (Smith et al., 2017) with default parameters. For normalization, deduplicated reads in

AsiSI specific restriction sites were counted using countBamInGRanges from the R package exomeCopy. The sample with the smallest number of AsiSI specific reads was divided by the number of respective reads from each sample. Resulting ratio was multiplied by the total amount of deduplicated reads and samples subsequently randomly subsampled to the calculated number of reads. AsiSI specific restriction sites were generated by in silico digestion of the hg19 genome. From the 1,123 predicted restriction sites, sites without mapped reads across all conditions in the respective experiment were dropped. BLISS8 density profiles were generated using the R package metagene2 with the assay parameter 'ChIPseq', 150 bp read extension and 50 bins to smoothen the graph. Gene sets were generated from RNA sequencing data using RPKM (gene expression).

BLISS8 stratification by expression is based on published K562 polyA-RNAseq data from the ENCODE portal (https://www.encodeproject.org/) with the following identifier: ENCSR040YBR. The R data set TxDb.Hsapiens.UCSC.hg19.knownGene was subsampled using the selected 5,576 bottom and 5,458 top expressed genes and filtered for a minimum gene length of 1,500 bp. Further stratifications are based on respective lists mentioned in this paragraph and adapted as described. Artefacts produced by proximal downstream transcriptional start sites were filtered out.

Positional co-localization of immunofluorescence data was performed by co-staining of MYC and the protein of interest. Acquisition was done using the Operetta CSL high-content imaging system at 40x or 20x. Graphical compartmentalization was performed in the Harmony high-content analysis software with following analysis sequence. First MYC multimers were found as described. To determine whether a multimer qualifies as sphere-like, the image was inverted and maxima with fixed threshold of size and relative intensity above background searched with the find spots algorithm; if successful, the remaining multimer area was defined as multimer shell. Multimers failing to fulfill these criteria were considered as unstructured. For calculations of positional co-localization the intensity of the co-stained protein in the multimer interior and multimer shell were determined. In R, the ratio of multimer shell over multimer interior for the co-stained protein were calculated for each individual multimer. Ratios below 1 are considered as indications of engulfment inside the MYC multimer. For all calculations at least 1,000 cells were considered.

For analysis of quantitative mass spectrometry, raw data files were analyzed using MaxQuant (version 1.6.14.0) (Cox and Mann, 2008). Parent ion and MS2 spectra were searched against a reference proteome database containing human protein sequences obtained from UniProtKB (version 2021_03) using Andromeda search engine (Cox et al., 2011). For APEX2-MYC, TMT label correction factors were imported into MaxQuant according to manufacturer's specifications. TMTPro labels were imported into MaxQuant by appending the modifications.xml file, as described (Petelski et al., 2021). TMTPro reporters were searched at the MS2 reporter ion level with a mass tolerance 0.003 Da and with PIF ≥ 0.75. Spectra were searched with a strict trypsin specificity and allowing up to two miscleavages. Cysteine carbamidomethylation was searched as a fixed modification, whereas protein N-terminal acetylation, methionine oxidation and N-ethylmaleimide modification of cysteines (mass difference to cysteine carbamidomethylation) were searched as variable modifications. Maximum number of modifications per peptide was set to 6. The dataset was filtered based on posterior error probability (PEP) to arrive at a false discovery rate of below 1% estimated using a target-decoy approach68. Statistical analysis and MS data visualization were performed using the R software environment (version 1.3.1093). Potential contaminants, reverse hits, hits only identified by site and hits with no unique peptides were excluded from the analysis. Corrected reporter intensities were normalized treatment-wise with the quantile normalization approach, using the Limma package. Additionally, to account for different MYC expression levels upon MG-132 treatment and allow better assessment of differential binding, intensities were normalized per TMT channel by dividing them with the MYC intensity from the respective channel. P-values and false discovery rates were calculated using a moderated t-test (Limma package). GO-term analysis was done using the gprofiler2 package for peptides increasing proximity to MYC significantly (FDR<0.05) upon MG-132 treatment.

8 Bibliography

Adhikary, S., Marinoni, F., Hock, A., Hulleman, E., Popov, N., Beier, R., Bernard, S., Quarto, M., Capra, M., Goettig, S., et al. (2005). The ubiquitin ligase HectH9 regulates transcriptional activation by Myc and is essential for tumor cell proliferation. Cell *123*, 409-421. 10.1016/j.cell.2005.08.016.

Aguilera, A., and Garcia-Muse, T. (2012). R loops: from transcription byproducts to threats to genome stability. Mol Cell *46*, 115-124. 10.1016/j.molcel.2012.04.009.

Alshareedah, I., Moosa, M.M., Raju, M., Potoyan, D.A., and Banerjee, P.R. (2020). Phase transition of RNA-protein complexes into ordered hollow condensates. Proc Natl Acad Sci U S A *117*, 15650-15658. 10.1073/pnas.1922365117.

Arabi, A., Rustum, C., Hallberg, E., and Wright, A.P. (2003). Accumulation of c-Myc and proteasomes at the nucleoli of cells containing elevated c-Myc protein levels. J Cell Sci *116*, 1707-1717. 10.1242/jcs.00370.

Bah, A., and Forman-Kay, J.D. (2016). Modulation of Intrinsically Disordered Protein Function by Post-translational Modifications. J Biol Chem *291*, 6696-6705. 10.1074/jbc.R115.695056.

Baluapuri, A., Hofstetter, J., Dudvarski Stankovic, N., Endres, T., Bhandare, P., Vos, S.M., Adhikari, B., Schwarz, J.D., Narain, A., Vogt, M., et al. (2019). MYC Recruits SPT5 to RNA Polymerase II to Promote Processive Transcription Elongation. Mol Cell *74*, 674-687 e611. 10.1016/j.molcel.2019.02.031.

Baluapuri, A., Wolf, E., and Eilers, M. (2020). Target gene-independent functions of MYC oncoproteins. Nat Rev Mol Cell Biol. 10.1038/s41580-020-0215-2.

Banani, S.F., Lee, H.O., Hyman, A.A., and Rosen, M.K. (2017). Biomolecular condensates: organizers of cellular biochemistry. Nat Rev Mol Cell Biol *18*, 285-298. 10.1038/nrm.2017.7.

Banani, S.F., Rice, A.M., Peeples, W.B., Lin, Y., Jain, S., Parker, R., and Rosen, M.K. (2016). Compositional Control of Phase-Separated Cellular Bodies. Cell *166*, 651-663. 10.1016/j.cell.2016.06.010.

Blackwood, E.M., and Eisenman, R.N. (1991). Max: a helix-loop-helix zipper protein that forms a sequence-specific DNA-binding complex with Myc. Science *251*, 1211-1217. 10.1126/science.2006410.

Boeynaems, S., Alberti, S., Fawzi, N.L., Mittag, T., Polymenidou, M., Rousseau, F., Schymkowitz, J., Shorter, J., Wolozin, B., Van Den Bosch, L., et al. (2018). Protein Phase Separation: A New Phase in Cell Biology. Trends Cell Biol *28*, 420-435. 10.1016/j.tcb.2018.02.004.

Boija, A., Klein, I.A., Sabari, B.R., Dall'Agnese, A., Coffey, E.L., Zamudio, A.V., Li, C.H., Shrinivas, K., Manteiga, J.C., Hannett, N.M., et al. (2018). Transcription Factors Activate Genes through the Phase-Separation Capacity of Their Activation Domains. Cell *175*, 1842-1855 e1816. 10.1016/j.cell.2018.10.042.

Boija, A., Klein, I.A., and Young, R.A. (2021). Biomolecular Condensates and Cancer. Cancer Cell *39*, 174-192. 10.1016/j.ccell.2020.12.003.

Bradner, J.E., Hnisz, D., and Young, R.A. (2017). Transcriptional Addiction in Cancer. Cell *168*, 629-643. 10.1016/j.cell.2016.12.013.

Buchel, G., Carstensen, A., Mak, K.Y., Roeschert, I., Leen, E., Sumara, O., Hofstetter, J., Herold, S., Kalb, J., Baluapuri, A., et al. (2017). Association with Aurora-A Controls N-MYC-Dependent Promoter Escape and Pause Release of RNA Polymerase II during the Cell Cycle. Cell Rep *21*, 3483-3497. 10.1016/j.celrep.2017.11.090.

Bunting, S.F., Callen, E., Wong, N., Chen, H.T., Polato, F., Gunn, A., Bothmer, A., Feldhahn, N., Fernandez-Capetillo, O., Cao, L., et al. (2010). 53BP1 inhibits homologous recombination in Brca1-deficient cells by blocking resection of DNA breaks. Cell *141*, 243-254. 10.1016/j.cell.2010.03.012.

Chatterjee, N., and Walker, G.C. (2017). Mechanisms of DNA damage, repair, and mutagenesis. Environ Mol Mutagen *58*, 235-263. 10.1002/em.22087.

Chen, A.Y., and Liu, L.F. (1994). DNA topoisomerases: essential enzymes and lethal targets. Annu Rev Pharmacol Toxicol *34*, 191-218. 10.1146/annurev.pa.34.040194.001203.

Chen, L., and Kashina, A. (2021). Post-translational Modifications of the Protein Termini. Front Cell Dev Biol *9*, 719590. 10.3389/fcell.2021.719590.

Chen, Y., Sun, X.X., Sears, R.C., and Dai, M.S. (2019). Writing and erasing MYC ubiquitination and SUMOylation. Genes Dis *6*, 359-371. 10.1016/j.gendis.2019.05.006.

Cho, K.F., Branon, T.C., Udeshi, N.D., Myers, S.A., Carr, S.A., and Ting, A.Y. (2020). Proximity labeling in mammalian cells with TurboID and split-TurboID. Nat Protoc *15*, 3971-3999. 10.1038/s41596-020-0399-0.

Cimprich, K.A., and Cortez, D. (2008). ATR: an essential regulator of genome integrity. Nat Rev Mol Cell Biol *9*, 616-627. 10.1038/nrm2450.

Clouaire, T., Rocher, V., Lashgari, A., Arnould, C., Aguirrebengoa, M., Biernacka, A., Skrzypczak, M., Aymard, F., Fongang, B., Dojer, N., et al. (2018). Comprehensive Mapping of Histone Modifications at DNA Double-Strand Breaks Deciphers Repair Pathway Chromatin Signatures. Mol Cell *72*, 250-262 e256. 10.1016/j.molcel.2018.08.020.

Conibear, A.C. (2020). Deciphering protein post-translational modifications using chemical biology tools. Nature Reviews Chemistry *4*, 674-695.

Cortazar, M.A., Sheridan, R.M., Erickson, B., Fong, N., Glover-Cutter, K., Brannan, K., and Bentley, D.L. (2019). Control of RNA Pol II Speed by PNUTS-PP1 and Spt5 Dephosphorylation Facilitates Termination by a "Sitting Duck Torpedo" Mechanism. Mol Cell *76*, 896-908 e894. 10.1016/j.molcel.2019.09.031.

Cox, J., and Mann, M. (2008). MaxQuant enables high peptide identification rates, individualized p.p.b.-range mass accuracies and proteome-wide protein quantification. Nat Biotechnol *26*, 1367-1372. 10.1038/nbt.1511.

Cox, J., Neuhauser, N., Michalski, A., Scheltema, R.A., Olsen, J.V., and Mann, M. (2011). Andromeda: a peptide search engine integrated into the MaxQuant environment. J Proteome Res *10*, 1794-1805. 10.1021/pr101065j.

Cugusi, S., Mitter, R., Kelly, G.P., Walker, J., Han, Z., Pisano, P., Wierer, M., Stewart, A., and Svejstrup, J.Q. (2022). Heat shock induces premature transcript termination and reconfigures the human transcriptome. Mol Cell *82*, 1573-1588 e1510. 10.1016/j.molcel.2022.01.007.

Cunningham, C.N., Baughman, J.M., Phu, L., Tea, J.S., Yu, C., Coons, M., Kirkpatrick, D.S., Bingol, B., and Corn, J.E. (2015). USP30 and parkin homeostatically regulate atypical ubiquitin chains on mitochondria. Nat Cell Biol *17*, 160-169. 10.1038/ncb3097.

Damgaard, R.B. (2021). The ubiquitin system: from cell signalling to disease biology and new therapeutic opportunities. Cell Death Differ *28*, 423-426. 10.1038/s41418-020-00703-w.

Dang, C.V. (2012). MYC on the path to cancer. Cell *149*, 22-35. 10.1016/j.cell.2012.03.003.

Das, S.K., Kuzin, V., Cameron, D.P., Sanford, S., Jha, R.K., Nie, Z., Rosello, M.T., Holewinski, R., Andresson, T., Wisniewski, J., et al. (2022). MYC assembles and stimulates topoisomerases 1 and 2 in a "topoisome". Mol Cell *82*, 140-158 e112. 10.1016/j.molcel.2021.11.016.

Dionne, U., and Gingras, A.C. (2022). Proximity-Dependent Biotinylation Approaches to Explore the Dynamic Compartmentalized Proteome. Front Mol Biosci *9*, 852911. 10.3389/fmolb.2022.852911.

Durcan, T.M., Tang, M.Y., Perusse, J.R., Dashti, E.A., Aguileta, M.A., McLelland, G.L., Gros, P., Shaler, T.A., Faubert, D., Coulombe, B., and Fon, E.A. (2014). USP8 regulates mitophagy by removing K6-linked ubiquitin conjugates from parkin. Embo J *33*, 2473-2491. 10.15252/embj.201489729.

Edenberg, E.R., Downey, M., and Toczyski, D. (2014). Polymerase stalling during replication, transcription and translation. Curr Biol *24*, R445-452. 10.1016/j.cub.2014.03.060.

Eilers, M., and Eisenman, R.N. (2008). Myc's broad reach. Genes Dev *22*, 2755-2766. 10.1101/gad.1712408.

Elbaum-Garfinkle, S., Kim, Y., Szczepaniak, K., Chen, C.C., Eckmann, C.R., Myong, S., and Brangwynne, C.P. (2015). The disordered P granule protein LAF-1 drives phase separation into droplets with tunable viscosity and dynamics. Proc Natl Acad Sci U S A *112*, 7189-7194. 10.1073/pnas.1504822112.

Endres, T., Solvie, D., Heidelberger, J.B., Andrioletti, V., Baluapuri, A., Ade, C.P., Muhar, M., Eilers, U., Vos, S.M., Cramer, P., et al. (2021). Ubiquitylation of MYC couples transcription elongation with double-strand break repair at active promoters. Mol Cell. 10.1016/j.molcel.2020.12.035.

Farrell, A.S., and Sears, R.C. (2014). MYC degradation. Cold Spring Harb Perspect Med *4*. 10.1101/cshperspect.a014365.

Ferlay, J., Colombet, M., Soerjomataram, I., Parkin, D.M., Pineros, M., Znaor, A., and Bray, F. (2021). Cancer statistics for the year 2020: An overview. Int J Cancer. 10.1002/ijc.33588.

Freese, N.H., Norris, D.C., and Loraine, A.E. (2016). Integrated genome browser: visual analytics platform for genomics. Bioinformatics *32*, 2089-2095. 10.1093/bioinformatics/btw069.

Gandarillas, A., and Watt, F.M. (1997). c-Myc promotes differentiation of human epidermal stem cells. Genes Dev *11*, 2869-2882. 10.1101/gad.11.21.2869.

Garcia-Muse, T., and Aguilera, A. (2016). Transcription-replication conflicts: how they occur and how they are resolved. Nat Rev Mol Cell Biol *17*, 553-563. 10.1038/nrm.2016.88.

Gomes, E., and Shorter, J. (2019). The molecular language of membraneless organelles. J Biol Chem *294*, 7115-7127. 10.1074/jbc.TM118.001192.

Grandori, C., Cowley, S.M., James, L.P., and Eisenman, R.N. (2000). The Myc/Max/Mad network and the transcriptional control of cell behavior. Annu Rev Cell Dev Biol *16*, 653-699. 10.1146/annurev.cellbio.16.1.653.

Greaves, M., and Maley, C.C. (2012). Clonal evolution in cancer. Nature *481*, 306-313. 10.1038/nature10762.

Gu, X., Zhuang, A., Yu, J., Chai, P., Jia, R., and Ruan, J. (2022). Phase separation drives tumor pathogenesis and evolution: all roads lead to Rome. Oncogene *41*, 1527-1535. 10.1038/s41388-022-02195-z.

Guo, J., Li, T., Schipper, J., Nilson, K.A., Fordjour, F.K., Cooper, J.J., Gordan, R., and Price, D.H. (2014). Sequence specificity incompletely defines the genome-wide occupancy of Myc. Genome Biol *15*, 482. 10.1186/s13059-014-0482-3.

Hanahan, D., and Weinberg, R.A. (2000). The hallmarks of cancer. Cell *100*, 57-70. 10.1016/s0092-8674(00)81683-9.

Hanahan, D., and Weinberg, R.A. (2011). Hallmarks of cancer: the next generation. Cell *144*, 646-674. 10.1016/j.cell.2011.02.013.

He, T.C., Sparks, A.B., Rago, C., Hermeking, H., Zawel, L., da Costa, L.T., Morin, P.J., Vogelstein, B., and Kinzler, K.W. (1998). Identification of c-MYC as a target of the APC pathway. Science *281*, 1509-1512. 10.1126/science.281.5382.1509.

Heidelberger, J.B., Voigt, A., Borisova, M.E., Petrosino, G., Ruf, S., Wagner, S.A., and Beli, P. (2018). Proteomic profiling of VCP substrates links VCP to K6-linked ubiquitylation and c-Myc function. EMBO Rep *19*. 10.15252/embr.201744754.

Herold, S., Kalb, J., Buchel, G., Ade, C.P., Baluapuri, A., Xu, J., Koster, J., Solvie, D., Carstensen, A., Klotz, C., et al. (2019). Recruitment of BRCA1 limits MYCN-driven accumulation of stalled RNA polymerase. Nature *567*, 545-549. 10.1038/s41586-019-1030-9.

Hershko, A., Eytan, E., Ciechanover, A., and Haas, A.L. (1982). Immunochemical analysis of the turnover of ubiquitin-protein conjugates in intact cells. Relationship to the breakdown of abnormal proteins. J Biol Chem *257*, 13964-13970.

Hong, S.Y., Kao, Y.R., Lee, T.C., and Wu, C.W. (2018). Upregulation of E3 Ubiquitin Ligase CBLC Enhances EGFR Dysregulation and Signaling in Lung Adenocarcinoma. Cancer Res *78*, 4984-4996. 10.1158/0008-5472.CAN-17-3858.

Hornbeck, P.V., Zhang, B., Murray, B., Kornhauser, J.M., Latham, V., and Skrzypek, E. (2015). PhosphoSitePlus, 2014: mutations, PTMs and recalibrations. Nucleic Acids Res *43*, D512-520. 10.1093/nar/gku1267.

Hou, L., Wang, Y., Liu, Y., Zhang, N., Shamovsky, I., Nudler, E., Tian, B., and Dynlacht, B.D. (2019). Paf1C regulates RNA polymerase II progression by modulating elongation rate. Proc Natl Acad Sci U S A *116*, 14583-14592. 10.1073/pnas.1904324116.

Hu, G., Katuwawala, A., Wang, K., Wu, Z., Ghadermarzi, S., Gao, J., and Kurgan, L. (2021). flDPnn: Accurate intrinsic disorder prediction with putative propensities of disorder functions. Nat Commun *12*, 4438. 10.1038/s41467-021-24773-7.

Hunkeler, M., Jin, C.Y., Ma, M.W., Monda, J.K., Overwijn, D., Bennett, E.J., and Fischer, E.S. (2021). Solenoid architecture of HUWE1 contributes to ligase activity and substrate recognition. Mol Cell *81*, 3468-3480 e3467. 10.1016/j.molcel.2021.06.032.

Jacquet, K., Fradet-Turcotte, A., Avvakumov, N., Lambert, J.P., Roques, C., Pandita, R.K., Paquet, E., Herst, P., Gingras, A.C., Pandita, T.K., et al. (2016). The TIP60 Complex Regulates Bivalent Chromatin Recognition by 53BP1 through Direct H4K20me Binding and H2AK15 Acetylation. Mol Cell *62*, 409-421. 10.1016/j.molcel.2016.03.031.

Jaenicke, L.A., von Eyss, B., Carstensen, A., Wolf, E., Xu, W., Greifenberg, A.K., Geyer, M., Eilers, M., and Popov, N. (2016). Ubiquitin-Dependent Turnover of MYC Antagonizes MYC/PAF1C Complex Accumulation to Drive Transcriptional Elongation. Mol Cell *61*, 54-67. 10.1016/j.molcel.2015.11.007.

Jumper, J., Evans, R., Pritzel, A., Green, T., Figurnov, M., Ronneberger, O., Tunyasuvunakool, K., Bates, R., Zidek, A., Potapenko, A., et al. (2021). Highly accurate protein structure prediction with AlphaFold. Nature *596*, 583-589. 10.1038/s41586-021-03819-2.

Kalkat, M., Resetca, D., Lourenco, C., Chan, P.K., Wei, Y., Shiah, Y.J., Vitkin, N., Tong, Y., Sunnerhagen, M., Done, S.J., et al. (2018). MYC Protein Interactome Profiling Reveals Functionally Distinct Regions that Cooperate to Drive Tumorigenesis. Mol Cell *72*, 836-848 e837. 10.1016/j.molcel.2018.09.031.

Kao, S.H., Wu, H.T., and Wu, K.J. (2018). Ubiquitination by HUWE1 in tumorigenesis and beyond. J Biomed Sci *25*, 67. 10.1186/s12929-018-0470-0.

Kato, G.J., Barrett, J., Villa-Garcia, M., and Dang, C.V. (1990). An amino-terminal c-myc domain required for neoplastic transformation activates transcription. Mol Cell Biol *10*, 5914-5920. 10.1128/mcb.10.11.5914-5920.1990.

Kim, D., Pertea, G., Trapnell, C., Pimentel, H., Kelley, R., and Salzberg, S.L. (2013). TopHat2: accurate alignment of transcriptomes in the presence of insertions, deletions and gene fusions. Genome Biol *14*, R36. 10.1186/gb-2013-14-4-r36.

Kim, S.Y., Herbst, A., Tworkowski, K.A., Salghetti, S.E., and Tansey, W.P. (2003). Skp2 regulates Myc protein stability and activity. Mol Cell *11*, 1177-1188. 10.1016/s1097-2765(03)00173-4.

Kim, W., Bennett, E.J., Huttlin, E.L., Guo, A., Li, J., Possemato, A., Sowa, M.E., Rad, R., Rush, J., Comb, M.J., et al. (2011). Systematic and quantitative assessment of the ubiquitin-modified proteome. Mol Cell *44*, 325-340. 10.1016/j.molcel.2011.08.025.

Kiskowski, M.A., Hancock, J.F., and Kenworthy, A.K. (2009). On the use of Ripley's K-function and its derivatives to analyze domain size. Biophys J *97*, 1095-1103. 10.1016/j.bpj.2009.05.039.

Kokic, G., Chernev, A., Tegunov, D., Dienemann, C., Urlaub, H., and Cramer, P. (2019). Structural basis of TFIIH activation for nucleotide excision repair. Nat Commun *10*, 2885. 10.1038/s41467-019-10745-5.

Kontomanolis, E.N., Koutras, A., Syllaios, A., Schizas, D., Mastoraki, A., Garmpis, N., Diakosavvas, M., Angelou, K., Tsatsaris, G., Pagkalos, A., et al. (2020). Role of Oncogenes and Tumor-suppressor Genes in Carcinogenesis: A Review. Anticancer Res *40*, 6009-6015. 10.21873/anticanres.14622.

Kouzine, F., Gupta, A., Baranello, L., Wojtowicz, D., Ben-Aissa, K., Liu, J., Przytycka, T.M., and Levens, D. (2013). Transcription-dependent dynamic supercoiling is a short-range genomic force. Nat Struct Mol Biol *20*, 396-403. 10.1038/nsmb.2517.

Lachaud, C., Moreno, A., Marchesi, F., Toth, R., Blow, J.J., and Rouse, J. (2016). Ubiquitinated Fancd2 recruits Fan1 to stalled replication forks to prevent genome instability. Science *351*, 846-849. 10.1126/science.aad5634.

Langmead, B., and Salzberg, S.L. (2012). Fast gapped-read alignment with Bowtie 2. Nat Methods *9*, 357-359. 10.1038/nmeth.1923.

Langmead, B., Trapnell, C., Pop, M., and Salzberg, S.L. (2009). Ultrafast and memory-efficient alignment of short DNA sequences to the human genome. Genome Biol *10*, R25. 10.1186/gb-2009-10-3-r25.

Lee, S.W., Li, C.F., Jin, G., Cai, Z., Han, F., Chan, C.H., Yang, W.L., Li, B.K., Rezaeian, A.H., Li, H.Y., et al. (2015). Skp2-dependent ubiquitination and activation of LKB1 is essential for cancer cell survival under energy stress. Mol Cell *57*, 1022-1033. 10.1016/j.molcel.2015.01.015.

Lemay, J.F., Larochelle, M., Marguerat, S., Atkinson, S., Bahler, J., and Bachand, F. (2014). The RNA exosome promotes transcription termination of backtracked RNA polymerase II. Nat Struct Mol Biol *21*, 919-926. 10.1038/nsmb.2893.

Levone, B.R., Lenzken, S.C., Antonaci, M., Maiser, A., Rapp, A., Conte, F., Reber, S., Mechtersheimer, J., Ronchi, A.E., Muhlemann, O., et al. (2021). FUS-dependent liquid-liquid phase separation is important for DNA repair initiation. J Cell Biol *220*. 10.1083/jcb.202008030.

Li, H., Handsaker, B., Wysoker, A., Fennell, T., Ruan, J., Homer, N., Marth, G., Abecasis, G., Durbin, R., and Genome Project Data Processing, S. (2009). The Sequence Alignment/Map format and SAMtools. Bioinformatics *25*, 2078-2079. 10.1093/bioinformatics/btp352.

Li, J., Van Vranken, J.G., Pontano Vaites, L., Schweppe, D.K., Huttlin, E.L., Etienne, C., Nandhikonda, P., Viner, R., Robitaille, A.M., Thompson, A.H., et al. (2020). TMTpro reagents: a set of isobaric labeling mass tags enables simultaneous proteome-wide measurements across 16 samples. Nat Methods *17*, 399-404. 10.1038/s41592-020-0781-4.

Lin, C.Y., Loven, J., Rahl, P.B., Paranal, R.M., Burge, C.B., Bradner, J.E., Lee, T.I., and Young, R.A. (2012). Transcriptional amplification in tumor cells with elevated c-Myc. Cell *151*, 56-67. 10.1016/j.cell.2012.08.026.

Liu, P., Gan, W., Su, S., Hauenstein, A.V., Fu, T.M., Brasher, B., Schwerdtfeger, C., Liang, A.C., Xu, M., and Wei, W. (2018). K63-linked polyubiquitin chains bind to DNA to facilitate DNA damage repair. Sci Signal *11*. 10.1126/scisignal.aar8133.

Llombart, V., and Mansour, M.R. (2022). Therapeutic targeting of "undruggable" MYC. EBioMedicine *75*, 103756. 10.1016/j.ebiom.2021.103756.

Lorenzin, F., Benary, U., Baluapuri, A., Walz, S., Jung, L.A., von Eyss, B., Kisker, C., Wolf, J., Eilers, M., and Wolf, E. (2016). Different promoter affinities account for specificity in MYC-dependent gene regulation. Elife *5*. 10.7554/eLife.15161.

Macheret, M., and Halazonetis, T.D. (2018). Intragenic origins due to short G1 phases underlie oncogene-induced DNA replication stress. Nature *555*, 112-116. 10.1038/nature25507.

Madabhushi, R., Gao, F., Pfenning, A.R., Pan, L., Yamakawa, S., Seo, J., Rueda, R., Phan, T.X., Yamakawa, H., Pao, P.C., et al. (2015). Activity-Induced DNA Breaks Govern the Expression of Neuronal Early-Response Genes. Cell *161*, 1592-1605. 10.1016/j.cell.2015.05.032.

Marechal, A., and Zou, L. (2015). RPA-coated single-stranded DNA as a platform for post-translational modifications in the DNA damage response. Cell Res *25*, 9-23. 10.1038/cr.2014.147.

McMahon, S.B., Van Buskirk, H.A., Dugan, K.A., Copeland, T.D., and Cole, M.D. (1998). The novel ATM-related protein TRRAP is an essential cofactor for the c-Myc and E2F oncoproteins. Cell *94*, 363-374. 10.1016/s0092-8674(00)81479-8.

Menolfi, D., and Zha, S. (2020). ATM, ATR and DNA-PKcs kinases-the lessons from the mouse models: inhibition not equal deletion. Cell Biosci *10*, 8. 10.1186/s13578-020-0376-x.

Meyer, H.J., and Rape, M. (2014). Enhanced protein degradation by branched ubiquitin chains. Cell *157*, 910-921. 10.1016/j.cell.2014.03.037.

Michel, M.A., Swatek, K.N., Hospenthal, M.K., and Komander, D. (2017). Ubiquitin Linkage-Specific Affimers Reveal Insights into K6-Linked Ubiquitin Signaling. Molecular Cell *68*, 233-246.e235. 10.1016/j.molcel.2017.08.020.

Mijic, S., Zellweger, R., Chappidi, N., Berti, M., Jacobs, K., Mutreja, K., Ursich, S., Ray Chaudhuri, A., Nussenzweig, A., Janscak, P., and Lopes, M. (2017). Replication fork reversal triggers fork degradation in BRCA2-defective cells. Nat Commun *8*, 859. 10.1038/s41467-017-01164-5.

Moyal, L., Lerenthal, Y., Gana-Weisz, M., Mass, G., So, S., Wang, S.Y., Eppink, B., Chung, Y.M., Shalev, G., Shema, E., et al. (2011). Requirement of ATM-dependent monoubiquitylation of histone H2B for timely repair of DNA double-strand breaks. Mol Cell *41*, 529-542. 10.1016/j.molcel.2011.02.015.

Nair, S.K., and Burley, S.K. (2003). X-ray structures of Myc-Max and Mad-Max recognizing DNA. Molecular bases of regulation by proto-oncogenic transcription factors. Cell *112*, 193-205. 10.1016/s0092-8674(02)01284-9.

Narain, A., Bhandare, P., Adhikari, B., Backes, S., Eilers, M., Dolken, L., Schlosser, A., Erhard, F., Baluapuri, A., and Wolf, E. (2021). Targeted protein degradation reveals a direct role of SPT6 in RNAPII elongation and termination. Mol Cell *81*, 3110-3127 e3114. 10.1016/j.molcel.2021.06.016.

Nie, Z., Guo, C., Das, S.K., Chow, C.C., Batchelor, E., Simons, S.S.J., and Levens, D. (2020). Dissecting transcriptional amplification by MYC. Elife *9*. 10.7554/eLife.52483.

Nie, Z., Hu, G., Wei, G., Cui, K., Yamane, A., Resch, W., Wang, R., Green, D.R., Tessarollo, L., Casellas, R., et al. (2012). c-Myc is a universal amplifier of expressed genes in lymphocytes and embryonic stem cells. Cell *151*, 68-79. 10.1016/j.cell.2012.08.033.

Noe Gonzalez, M., Blears, D., and Svejstrup, J.Q. (2021). Causes and consequences of RNA polymerase II stalling during transcript elongation. Nat Rev Mol Cell Biol *22*, 3-21. 10.1038/s41580-020-00308-8.

Papadopoulos, D., Solvie, D., Baluapuri, A., Endres, T., Ha, S.A., Herold, S., Kalb, J., Giansanti, C., Schülein-Völk, C., Ade, C.P., et al. (2021). MYCN recruits the nuclear exosome complex to RNA polymerase II to prevent transcription-replication conflicts. Mol Cell. 10.1016/j.molcel.2021.11.002.

Paull, T.T. (2015). Mechanisms of ATM Activation. Annu Rev Biochem *84*, 711-738. 10.1146/annurev-biochem-060614-034335.

Peng, K., Radivojac, P., Vucetic, S., Dunker, A.K., and Obradovic, Z. (2006). Length-dependent prediction of protein intrinsic disorder. BMC Bioinformatics *7*, 208. 10.1186/1471-2105-7-208.

Petelski, A.A., Emmott, E., Leduc, A., Huffman, R.G., Specht, H., Perlman, D.H., and Slavov, N. (2021). Multiplexed single-cell proteomics using SCoPE2. Nat Protoc *16*, 5398-5425. 10.1038/s41596-021-00616-z.

Peter, S., Bultinck, J., Myant, K., Jaenicke, L.A., Walz, S., Muller, J., Gmachl, M., Treu, M., Boehmelt, G., Ade, C.P., et al. (2014). Tumor cell-specific inhibition of MYC function using small molecule inhibitors of the HUWE1 ubiquitin ligase. EMBO Mol Med *6*, 1525-1541. 10.15252/emmm.201403927.

Popov, N., Schulein, C., Jaenicke, L.A., and Eilers, M. (2010). Ubiquitylation of the amino terminus of Myc by SCF(beta-TrCP) antagonizes SCF(Fbw7)-mediated turnover. Nat Cell Biol *12*, 973-981. 10.1038/ncb2104.

Quinlan, A.R., and Hall, I.M. (2010). BEDTools: a flexible suite of utilities for comparing genomic features. Bioinformatics *26*, 841-842. 10.1093/bioinformatics/btq033.

Rappsilber, J., Mann, M., and Ishihama, Y. (2007). Protocol for micro-purification, enrichment, pre-fractionation and storage of peptides for proteomics using StageTips. Nat Protoc *2*, 1896-1906. 10.1038/nprot.2007.261.

Robinson, M.D., McCarthy, D.J., and Smyth, G.K. (2010). edgeR: a Bioconductor package for differential expression analysis of digital gene expression data. Bioinformatics *26*, 139-140. 10.1093/bioinformatics/btp616.

Roeschert, I., Poon, E., Henssen, A.G., Garcia, H.D., Gatti, M., Giansanti, C., Jamin, Y., Ade, C.P., Gallant, P., Schulein-Volk, C., et al. (2021). Combined inhibition of Aurora-A and ATR kinase results in regression of MYCN-amplified neuroblastoma. Nat Cancer *2*, 312-326. 10.1038/s43018-020-00171-8.

Sabo, A., Kress, T.R., Pelizzola, M., de Pretis, S., Gorski, M.M., Tesi, A., Morelli, M.J., Bora, P., Doni, M., Verrecchia, A., et al. (2014). Selective transcriptional regulation by Myc in cellular growth control and lymphomagenesis. Nature *511*, 488-492. 10.1038/nature13537.

Saldivar, J.C., Cortez, D., and Cimprich, K.A. (2017). The essential kinase ATR: ensuring faithful duplication of a challenging genome. Nat Rev Mol Cell Biol *18*, 622-636. 10.1038/nrm.2017.67.

Scully, R., Panday, A., Elango, R., and Willis, N.A. (2019). DNA double-strand break repair-pathway choice in somatic mammalian cells. Nat Rev Mol Cell Biol *20*, 698-714. 10.1038/s41580-019-0152-0.

Sears, R., Nuckolls, F., Haura, E., Taya, Y., Tamai, K., and Nevins, J.R. (2000). Multiple Ras-dependent phosphorylation pathways regulate Myc protein stability. Genes Dev *14*, 2501-2514. 10.1101/gad.836800.

Sharp, P.A., Chakraborty, A.K., Henninger, J.E., and Young, R.A. (2022). RNA in formation and regulation of transcriptional condensates. RNA *28*, 52-57. 10.1261/rna.078997.121.

Shen, L., Shao, N., Liu, X., and Nestler, E. (2014). ngs.plot: Quick mining and visualization of next-generation sequencing data by integrating genomic databases. BMC Genomics *15*, 284. 10.1186/1471-2164-15-284.

Shin, Y., and Brangwynne, C.P. (2017). Liquid phase condensation in cell physiology and disease. Science *357*. 10.1126/science.aaf4382.

Shivji, M.K.K., Renaudin, X., Williams, C.H., and Venkitaraman, A.R. (2018). BRCA2 Regulates Transcription Elongation by RNA Polymerase II to Prevent R-Loop Accumulation. Cell Rep *22*, 1031-1039. 10.1016/j.celrep.2017.12.086.

Shou, Y., Martelli, M.L., Gabrea, A., Qi, Y., Brents, L.A., Roschke, A., Dewald, G., Kirsch, I.R., Bergsagel, P.L., and Kuehl, W.M. (2000). Diverse karyotypic abnormalities of the c-myc locus associated with c-myc dysregulation and tumor progression in multiple myeloma. Proc Natl Acad Sci U S A *97*, 228-233. 10.1073/pnas.97.1.228.

Singh, S., Szlachta, K., Manukyan, A., Raimer, H.M., Dinda, M., Bekiranov, S., and Wang, Y.H. (2020). Pausing sites of RNA polymerase II on actively transcribed genes are enriched in DNA double-stranded breaks. J Biol Chem *295*, 3990-4000. 10.1074/jbc.RA119.011665.

Smith, T., Heger, A., and Sudbery, I. (2017). UMI-tools: modeling sequencing errors in Unique Molecular Identifiers to improve quantification accuracy. Genome Res *27*, 491-499. 10.1101/gr.209601.116.

Solvie, D., Baluapuri, A., Uhl, L., Fleischhauer, D., Endres, T., Papadopoulos, D., Aziba, A., Gaballa, A., Mikicic, I., Isaakova, E., et al. (*in press*). Multimerization of MYC shields stalled replication forks from RNA polymerase. Nature.

Sun, X.X., Li, Y., Sears, R.C., and Dai, M.S. (2021). Targeting the MYC Ubiquitination-Proteasome Degradation Pathway for Cancer Therapy. Front Oncol *11*, 679445. 10.3389/fonc.2021.679445.

Swatek, K.N., and Komander, D. (2016). Ubiquitin modifications. Cell Res *26*, 399-422. 10.1038/cr.2016.39.

Sweeney, P., Park, H., Baumann, M., Dunlop, J., Frydman, J., Kopito, R., McCampbell, A., Leblanc, G., Venkateswaran, A., Nurmi, A., and Hodgson, R. (2017). Protein misfolding in neurodegenerative diseases: implications and strategies. Transl Neurodegener *6*, 6. 10.1186/s40035-017-0077-5.

Takahashi, K., and Yamanaka, S. (2006). Induction of pluripotent stem cells from mouse embryonic and adult fibroblast cultures by defined factors. Cell *126*, 663-676. 10.1016/j.cell.2006.07.024.

Tammaro, M., Barr, P., Ricci, B., and Yan, H. (2013). Replication-dependent and transcription-dependent mechanisms of DNA double-strand break induction by the topoisomerase 2-targeting drug etoposide. PLoS One *8*, e79202. 10.1371/journal.pone.0079202.

Tesi, A., de Pretis, S., Furlan, M., Filipuzzi, M., Morelli, M.J., Andronache, A., Doni, M., Verrecchia, A., Pelizzola, M., Amati, B., and Sabo, A. (2019). An early Myc-dependent transcriptional program orchestrates cell growth during B-cell activation. EMBO Rep *20*, e47987. 10.15252/embr.201947987.

Thakar, T., and Moldovan, G.L. (2021). The emerging determinants of replication fork stability. Nucleic Acids Res *49*, 7224-7238. 10.1093/nar/gkab344.

Thomas, L.R., Foshage, A.M., Weissmiller, A.M., Popay, T.M., Grieb, B.C., Qualls, S.J., Ng, V., Carboneau, B., Lorey, S., Eischen, C.M., and Tansey, W.P. (2016). Interaction of MYC with host cell factor-1 is mediated by the evolutionarily conserved Myc box IV motif. Oncogene *35*, 3613-3618. 10.1038/onc.2015.416.

Thomas, L.R., Wang, Q., Grieb, B.C., Phan, J., Foshage, A.M., Sun, Q., Olejniczak, E.T., Clark, T., Dey, S., Lorey, S., et al. (2015). Interaction with WDR5 promotes target gene recognition and tumorigenesis by MYC. Mol Cell *58*, 440-452. 10.1016/j.molcel.2015.02.028.

Toledo, L., Neelsen, K.J., and Lukas, J. (2017). Replication Catastrophe: When a Checkpoint Fails because of Exhaustion. Mol Cell *66*, 735-749. 10.1016/j.molcel.2017.05.001.

Tracz, M., and Bialek, W. (2021). Beyond K48 and K63: non-canonical protein ubiquitination. Cell Mol Biol Lett *26*, 1. 10.1186/s11658-020-00245-6.

van de Linde, S., Loschberger, A., Klein, T., Heidbreder, M., Wolter, S., Heilemann, M., and Sauer, M. (2011). Direct stochastic optical reconstruction microscopy with standard fluorescent probes. Nat Protoc *6*, 991-1009. 10.1038/nprot.2011.336.

Van Oss, S.B., Shirra, M.K., Bataille, A.R., Wier, A.D., Yen, K., Vinayachandran, V., Byeon, I.L., Cucinotta, C.E., Heroux, A., Jeon, J., et al. (2016). The Histone Modification Domain of Paf1 Complex Subunit Rtf1 Directly Stimulates H2B Ubiquitylation through an Interaction with Rad6. Mol Cell *64*, 815-825. 10.1016/j.molcel.2016.10.008.

Vennstrom, B., Sheiness, D., Zabielski, J., and Bishop, J.M. (1982). Isolation and characterization of c-myc, a cellular homolog of the oncogene (v-myc) of avian myelocytomatosis virus strain 29. J Virol *42*, 773-779. 10.1128/JVI.42.3.773-779.1982.

von der Lehr, N., Johansson, S., Wu, S., Bahram, F., Castell, A., Cetinkaya, C., Hydbring, P., Weidung, I., Nakayama, K., Nakayama, K.I., et al. (2003). The F-box protein Skp2 participates in c-Myc proteosomal degradation and acts as a cofactor for c-Myc-regulated transcription. Mol Cell *11*, 1189-1200. 10.1016/s1097-2765(03)00193-x.

Walz, S., Lorenzin, F., Morton, J., Wiese, K.E., von Eyss, B., Herold, S., Rycak, L., Dumay-Odelot, H., Karim, S., Bartkuhn, M., et al. (2014). Activation and repression by oncogenic MYC shape tumour-specific gene expression profiles. Nature *511*, 483-487. 10.1038/nature13473.

Welcker, M., Orian, A., Grim, J.E., Eisenman, R.N., and Clurman, B.E. (2004a). A nucleolar isoform of the Fbw7 ubiquitin ligase regulates c-Myc and cell size. Curr Biol *14*, 1852-1857. 10.1016/j.cub.2004.09.083.

Welcker, M., Orian, A., Jin, J., Grim, J.E., Harper, J.W., Eisenman, R.N., and Clurman, B.E. (2004b). The Fbw7 tumor suppressor regulates glycogen synthase kinase 3 phosphorylation-dependent c-Myc protein degradation. Proc Natl Acad Sci U S A *101*, 9085-9090. 10.1073/pnas.0402770101.

Welcker, M., Wang, B., Rusnac, D.V., Hussaini, Y., Swanger, J., Zheng, N., and Clurman, B.E. (2022). Two diphosphorylated degrons control c-Myc degradation by the Fbw7 tumor suppressor. Sci Adv *8*, eabl7872. 10.1126/sciadv.abl7872.

Wolter, S., Loschberger, A., Holm, T., Aufmkolk, S., Dabauvalle, M.C., van de Linde, S., and Sauer, M. (2012). rapidSTORM: accurate, fast open-source software for localization microscopy. Nature methods *9*, 1040-1041. 10.1038/nmeth.2224.

Wright, P.E., and Dyson, H.J. (2015). Intrinsically disordered proteins in cellular signalling and regulation. Nat Rev Mol Cell Biol *16*, 18-29. 10.1038/nrm3920.

Wu-Baer, F., Lagrazon, K., Yuan, W., and Baer, R. (2003). The BRCA1/BARD1 heterodimer assembles polyubiquitin chains through an unconventional linkage involving lysine residue K6 of ubiquitin. J Biol Chem *278*, 34743-34746. 10.1074/jbc.C300249200.

Xiao, H., Mao, Y., Desai, S.D., Zhou, N., Ting, C.Y., Hwang, J., and Liu, L.F. (2003). The topoisomerase IIbeta circular clamp arrests transcription and signals a 26S proteasome pathway. Proc Natl Acad Sci U S A *100*, 3239-3244. 10.1073/pnas.0736401100.

Xu, G., Paige, J.S., and Jaffrey, S.R. (2010a). Global analysis of lysine ubiquitination by ubiquitin remnant immunoaffinity profiling. Nat Biotechnol *28*, 868-873. 10.1038/nbt.1654.

Xu, Y., Sun, Y., Jiang, X., Ayrapetov, M.K., Moskwa, P., Yang, S., Weinstock, D.M., and Price, B.D. (2010b). The p400 ATPase regulates nucleosome stability and chromatin ubiquitination during DNA repair. J Cell Biol *191*, 31-43. 10.1083/jcb.201001160.

Yan, W.X., Mirzazadeh, R., Garnerone, S., Scott, D., Schneider, M.W., Kallas, T., Custodio, J., Wernersson, E., Li, Y., Gao, L., et al. (2017). BLISS is a versatile and quantitative method for genome-wide profiling of DNA double-strand breaks. Nat Commun *8*, 15058. 10.1038/ncomms15058.

Yuan, Y., Miao, Y., Qian, L., Zhang, Y., Liu, C., Liu, J., Zuo, Y., Feng, Q., Guo, T., Zhang, L., et al. (2020). Targeting UBE4A Revives Viperin Protein in Epithelium to Enhance Host Antiviral Defense. Mol Cell *77*, 734-747 e737. 10.1016/j.molcel.2019.11.003.

Zhang, L., and Elias, J.E. (2017). Relative Protein Quantification Using Tandem Mass Tag Mass Spectrometry. Methods Mol Biol *1550*, 185-198. 10.1007/978-1-4939-6747-6_14.

Zhang, Y., Liu, T., Meyer, C.A., Eeckhoute, J., Johnson, D.S., Bernstein, B.E., Nusbaum, C., Myers, R.M., Brown, M., Li, W., and Liu, X.S. (2008). Model-based analysis of ChIP-Seq (MACS). Genome Biol *9*, R137. 10.1186/gb-2008-9-9-r137.

Zhang, Z., Wang, D., Wang, P., Zhao, Y., and You, F. (2020). OTUD1 Negatively Regulates Type I IFN Induction by Disrupting Noncanonical Ubiquitination of IRF3. J Immunol *204*, 1904-1918. 10.4049/jimmunol.1900305.

Zhao, M., Song, K., Hao, W., Wang, L., Patil, G., Li, Q., Xu, L., Hua, F., Fu, B., Schwamborn, J.C., et al. (2020). Non-proteolytic ubiquitination of OTULIN regulates NF-kappaB signaling pathway. J Mol Cell Biol *12*, 163-175. 10.1093/jmcb/mjz081.

9 Appendix

9.1 Abbreviations

Abbreviation	
AURKA	Aurora kinase A
BCA	Bicinchoninic acid assay
BET	Base excision repair
BLISS	Breaks labelling *In Situ* and Sequencing
bHLH-LZ	Basic region of a Helix-Loop-Helix Leucin Zipper
BrdU	Bromodeoxyuridine
ChIP	Chromatin immunoprecipitation
DBD	DNA binding domain
DDR	DNA damage response
DMSO	Dimethyl sulfoxide
DNA	Desoxyribonucleic acid
dNTP	Deoxy-nucleotide triphosphate
Dox	Doxycycline
dsDNA	Double stranded DNA
DSB	Double strand break
dSTORM	Direct stochastic optical reconstruction microscopy
DUB	Deubiquitylating enzyme
E-box	Enhancer box
EdU	5-Ethynyl-2'-deoxyuridine
EtOH	Ethanol
FACS	Fluorescence-activated cell sorting
FCS	Fetal calf serum
FDR	False discovery rate
FRAP	Fluorescence recovery after photobleaching
GFP	Green fluorescent protein
H2Bubi	H2B monoubiquitylation
H_2O_2	Hydroxy peroxide
HA	Human influenza hemagglutinin
HR	Homologous recombination
HRP	Horseradish peroxidase
HU	Hydroxyurea
IAA	Indole-3-acetic-acid
IDR	Intrinsically disordered region

Abbreviation	
IR	Ionizing radiation
K	Lysine
m	Milli
M	Molar
µ	Micro
MB	MYC box
MMR	Mismatch repair
MS	Mass spectrometry
NaCl	Natrium Chloride
NER	Nucleotide excision repair
NHEJ	Non-homologous end joining
nm	Nano meter
PAF1c	RNA polymerase II associated factor 1 complex
PAGE	Polyacrylamide gel electrophoresis
PBS	Phosphate buffered saline
PCC	Pearson correlation coefficient
PCR	Polymerase Chain Reaction
PEI	Polyethyleneimine
PI	Propidium iodide
PLA	Proximity Ligation Assay
POI	Protein of interest
PP2A	Protein phosphatase 2A
pS2	Serine2-phosphorylated RNA polymerase II
pS5	Serine5-phosphorylated RNA polymerase II
PTM	Posttranslational modification
qPCR	Quantitative PCR
rcf	Rotational centrifugal force
RNA	Ribonucleic acid
RNAPII	RNA polymerase II
ROS	Reactive oxygen species
rRNA	Ribosomal ribonucleic acid
S4/S8	Phosphorylation of RPA32 at serine 4 and 8
S33	Phosphorylation of RPA32 at serine 33
S.D.	Standard deviation
SDS	Sodium dodecyl sulfate
Ser	Serine
S.E.M.	Standard error of the mean
SFFV	Spleen focus forming virus
SSB	Single strand break

Abbreviation	
ssDNA	Single stranded DNA
TAD	Transcriptional associated domain
TAE	Tris-Acetate-EDTA
TCR	Transcription-coupled repair
TRIS	Tris-(hydroxymethyl)-aminomethane
TRRAP	Transformation/transcription domain-associated protein
TSS	Transcription start site
UMI	Unique modifier index
UV	Ultraviolet radiation
WT	Wildtype

9.2 Acknowledgments

I would like to begin with extending my sincere gratitude to Prof. Dr. Martin Eilers for his invaluable support and advice, as well as the compelling projects, that encouraged me continuously during my work in his lab.

I am also very grateful to Prof. Dr. Petra Beli and Prof. Dr. Nikita Popov for their time and the helpful discussions in context of their function as members of my thesis advisory committee as well as the very productive collaborations that accompanied me throughout my PhD.

Special thanks to the GRK2243 for the funding and association during my PhD with many fascinating meetings, workshops, retreats, and conferences. In this context a big thanks to Prof. Dr. Alexander Buchberger.

I would like to express my deepest appreciation to Leonie Uhl and Dr. Apoorva Baluapuri for sharing so many endless hours, weekends, and holidays with me in the lab in order to face the monumental workload of the MYC multimerization story and Dr. Theresa Endres for the joint effort on the PAF1-HUWE1 story.

Many thanks to Prof. Dr. Elmar Wolf, Prof. Dr. Peter Gallant, Prof. Dr. Gabriele Büchel, Dr. Steffi Herold, Dr. Carsten Ade, as well as Dr. Giacomo Cossa and Dr. Raphael Silveira-Vidal for productive discussions and input at every stage of the research projects.

I am very grateful to Dr. Ursula Eilers and Dr. Christina Schülein-Völk for their help and support in every aspect regarding imaging experiments and high-throughput screening as well as analysis.

Further, I would like to thank Ulrike Samfaß and Tobias Roth for the technical support and the whole department for a productive, sometimes competitive but always fun environment.

Special gratitude to the long-lasting companions, Michi, Basti, Olli and Raphael that started their PhD/Postdoc with me and are still around – as well as the once that left already, my coffee-buddy Jacqueline, and Theresa, and the PhD students that started more recently and shaped the last year in the lab; the time here wouldn’t have been the same without you. At this point again a special thanks to Leonie for being an excellent first student that I supervised during her internship and despite that experience coming back for a PhD, all the time we shared in the lab and the office and all the work we did on past and probably future projects.

I am incredibly grateful to my former flatmate Alex for making the time during the Covid19-lockdown and restrictions bearable, all the gym, pizza and beer sessions and listening to me when stress got the best of me – I hope we will also find time for all of that in the future.

I cannot begin to express my thanks to my new flatmate Mareike, I hope I am showing you that every day.

Last but not least, all of this would not have been possible without the endless support, understanding and encouragement of my parents, siblings, and all of my family throughout the last 31 years.

The same extends to all my friends that may not have contributed to this thesis directly but made and are still making my life in Bonn, Munich, Linköping, Stockholm, Würzburg and everywhere else in the world a spectacular time.

9.3 Publications

Herold S*, Kalb J*, Büchel G*, Ade CP, Baluapuri A, Xu J, Koster J, **Solvie D**, Carstensen A, Klotz C, Rodewald S, Schülein-Völk C, Dobbelstein M, Wolf E, Molenaar J, Versteeg R, Walz S, Eilers M. Recruitment of BRCA1 limits MYCN-driven accumulation of stalled RNA polymerase. Nature. 2019 Mar;567(7749):545-549. doi: 10.1038/s41586-019-1030-9. Epub 2019 Mar 20. PMID: 30894746; PMCID: PMC7611299.

Endres T*, **Solvie D***, Heidelberger JB, Andrioletti V, Baluapuri A, Ade CP, Muhar M, Eilers U, Vos SM, Cramer P, Zuber J, Beli P, Popov N, Wolf E, Gallant P, Eilers M. Ubiquitylation of MYC couples transcription elongation with double-strand break repair at active promoters. Mol Cell. 2021 Feb 18;81(4):830-844.e13. doi: 10.1016/j.molcel.2020.12.035. Epub 2021 Jan 15. PMID: 33453168; PMCID: PMC7611325.

Papadopoulos D, **Solvie D**, Baluapuri A, Endres T, Ha SA, Herold S, Kalb J, Giansanti C, Schülein-Völk C, Ade CP, Schneider C, Gaballa A, Vos S, Fischer U, Dobbelstein M, Wolf E, Eilers M. MYCN recruits the nuclear exosome complex to RNA polymerase II to prevent transcription-replication conflicts. Mol Cell. 2022 Jan 6;82(1):159-176.e12. doi: 10.1016/j.molcel.2021.11.002. Epub 2021 Nov 29. PMID: 34847357.

Solvie D*, Baluapuri A*, Uhl L*, Fleischhauer D, Endres T, Papadopoulos D, Aziba A, Gaballa A, Mikicic I, Isaakova E, Giansanti C, Jansen J, Jungblut M, Klein T, Schülein-Völk C, Maric H, Doose S, Sauer M, Beli P, Rosenwald A, Dobbelstein M, Wolf E, Eilers M. MYC multimers shield stalled replication forks from RNA polymerase. Nature. *In press*.

* Authors contributed equally

9.4 Affidavit

Affidavit

I hereby confirm that my thesis entitled: “Molecular Mechanisms of MYC as Stress Resilience Factor” is the result of my own work. I did not receive any help or support from commercial consultants. All sources and/or materials are listed and specified in the thesis.

Furthermore, I confirm that this thesis has not yet been submitted as part of another examination process neither in identical nor in similar form.

Place, Date Daniel Solvie

Eidesstattliche Erklärung

Hiermit erkläre ich an Eidesstatt, die Dissertation "Molekulare Mechanismen von MYC als Stressresistenzfaktor" eigenständig, d. h. selbst-ständig und ohne Hilfe eines kommerziellen Promotionsberaters, angefertigt und keine anderen als die von mir angegebenen Quellen und Hilfsmittel verwendet zu haben.

Ich erkläre außerdem, dass die Dissertation weder in gleicher noch in ähnlicher Form bereits in einem anderen Prüfungsverfahren vorgelegt wurde.

Ort, Datum Daniel Solvie

9.5 Curriculum Vitae